THE EFFECTS OF ADDITIONAL NONMAGNETIC LAYERS ON STRUCTURE AND MAGNETIC PROPERTIES OF $L1_0$ FePt THIN FILMS

ZHAO ZELIANG

(B. Eng., HUNAN UNIVERSITY)

(MSc., INSTITUTE OF MATELS RESEARCH, CHINESE ACADEMY OF SCIENCES)

A THESIS SUBMITTED

FOR THE DEGREE OF DOCTOR OF PHILOSOPHY

DEPARTMENT OF MATERIAS SCIENCE,

NATIONAL UNIVERSITY OF SINGAPORE

2007

Acknowledgements

I would like to express my heartfelt thanks to my supervisors, Prof. Jun Ding, Prof. Jianping Wang, and Dr. Jingsheng Chen, for their guidance, inspiration, and encouragement throughout the course of my research. I am grateful for both their expertise and their commitment to their students.

My thanks also go to Dr Liu Bo, Mr Yi Jiabao, Mr Liu Binghai, Mr. Lim Boon Chow, Dr Zhou Tiejun, Dr Zhang Jun, Dr Sun Chengjun, Mr Han Yufei, Mr Ren Hanbiao, Mr Hu Jiangfeng, Mr Guan Tianpeng and other staff and students in Data storage institute and National University of Singapore, all of whom were extremely helpful with their assistance and friendship.

I also had invaluable help from Dr K. Inaba (Rigaku Co, Japan), Prof. Li Yi (NUS), Prof. Dong Zhili (NTU), and Prof Liu Yinong (University of Western Australia) for in-plane XRD, arc-melting, TEM, and SQUID experiments, respectively.

I would like to thank National university of Singapore and Data storage institute for the financial support and supplying me with an excellent research environment.

Last, but not least, I am especially grateful to my wife Wang Xiaochong and my family for their encouragement, care, and support.

Table of contents

Summary

An increase in the recording areal density requires the reduction of the size of the actual bits on the disk surface. However, the further reduction in the bit size may be limited by the superparamagnetism. Magnetic thin films with high magnetic anisotropy are necessary to overcome the superparamagnetic limit, when the magnetic recording areal density further increases. The $L1_0$ ordered phase iron-platinum (FePt) with a large magnetic anisotropy of 7.0×10^7 erg/cm^3 has received a great attention because of its potential application as perpendicular recording media with an ultra-high recording density.

However, the magnetic performance (coercivity and remanence) is often limited by the presence of the soft magnetic phase, *fcc*-FePt, which is frequently found in the as-deposited FePt films. The formation of the hard-magnetic $L1_0$ FePt *fct*-phase usually requires a relatively high deposition or annealing temperature over 600 °C for pure FePt. Since high fabrication temperature over 400 °C is not compatible with industrial process, it is important to develop methods to fabricate $L1_0$ FePt film which can be formed at a relatively low deposition or annealing temperature. The aim of this study was to reduce the phase transformation temperature of FePt thin films from disordered *fcc* to ordered $L1_0$ phase. A systematic investigation on Ag top layers, intermediate layers and underlayer on the phase transformation of the FePt thin films was conducted. The relationships between the microstructure, the disordered/ ordered phase transformation, and magnetic properties of the FePt films were studied.

With an Ag underlayer deposited at the bottom of the FePt layer, both the in-plane and out-of-plane coercivities of FePt film slightly increased comparing to the FePt film without underlayer. The main contribution of the underlayer was to improve the crystallinity of the FePt films. As a result, the coercivities in both direction of the FePt thin film were slightly increased.

Ag top and intermediate layers with different thicknesses were deposited on the top and between of FePt layers. The coercivity of FePt films increased significantly to about 6 kOe. The structural study suggested that Ag diffused into the FePt layer. The diffusion of Ag from the top of the films promoted the phase transformation of FePt. At the same time the intergranular exchange coupling in the FePt films was reduced, which resulted in the increase of the coercivity.

The formation temperature of the hard-magnetic $L1_0$ phase was significantly reduced when FePt films were deposited on the MgO substrate. However, relatively low coercivity of about 6 kOe was resulted without the insertion of additive layers. With ultrathin Ag intermediate layers deposited between FePt layers, the topography of the films changed from a continuous maze-like structure to an isolated island structure. The formation of the island structure may realize the decoupling between FePt particles and cause the change of magnetization reversal mechanism from domain wall pinning to coherent rotation. As a result, the out-of-plane coercivity of the FePt films increased to over 30 kOe.

List of publications

1. **Z. L. Zhao**, J. Ding, Y. Li, G. M. Chow, J. S. Chen, and J. P. Wang, "Microstructure studies of $L1_0$ - FePt thin films with high coercivity fabricated at low deposition temperatures", ***Metallurgical and Materials Transactions A***. **38A** 811 (2007).

2. **Z. L. Zhao,** J. S. Chen, J. Ding, B. H. Liu, J. B. Yi and J. P. Wang. "Fabrication and Microstructure of High Coercivity FePt Thin Films at 400 ^{o}C", ***Applied Physics Letters***. **88** 052503 (2006).

3. **Z. L. Zhao,** J. S. Chen, J. Ding, J. B. Yi, B. H. Liu and J. P. Wang. "Microstructure of high coercivity FePt thin films fabricated at 400 ^{o}C", ***IEEE Transaction on Magnetics***. **41** 3337 (2005).

4. **Z. L. Zhao**, J. Ding, J. B. Yi, J. S. Chen, and J. P. Wang, "Nanostructured FePt Thin Films with High Coercivity", ***Journal of Materials Science and Technology***. **21** 43 (2005).

5. **Z. L. Zhao**, J. Ding, J. B. Yi, J. S. Chen, J. H. Zeng, and J. P. Wang, "The mechanism of Ag top layer on the coercivity enhancement of FePt thin films", ***Journal of Applied Physics***. **97** 10H502 (2005).

6. **Z. L. Zhao,** K. Inaba, Y. Ito, J. Ding, J. S. Chen, and J. P. Wang. "Crystallographic ordering studies of the $L1_0$ phase transformation of FePt thin film with Ag top layer", ***Journal of Applied Physics***. **95** 7154 (2004).

7. **Z. L. Zhao,** J. Ding, J. S. Chen, and J. P. Wang. "The effects of pinning layers on the magnetic properties of FePt perpendicular media", ***Journal Magnetism and Magnetic Materials***. **272** 2186 (2004).

8. **Z. L. Zhao,** J. S. Chen, J. Ding, and J. P. Wang. "The effects of additive Ag layers on the $L1_0$ FePt phase transformation", ***Journal Magnetism and Magnetic Materials***. **282** 105 (2004).

9. **Z. L. Zhao,** J. Ding, J. S. Chen and J. P. Wang. "Coercivity Enhancement of FePt Thin Films with Nonmagnetic Ru Pinning Layer", ***Journal of Applied Physics***. **93** 7753 (2003).

10. **Z. L. Zhao,** J. Ding, K. Inaba, J. S. Chen, and J. P. Wang. "Promotion of $L1_0$ ordered phase transformation by the Ag top layer on FePt thin films", ***Applied Physics Letters***. **83** 2196 (2003).

11. **Z. L. Zhao,** J. P. Wang, J. S. Chen, and J. Ding. "Control of Magnetization Reversal Process with Pinning Layer in FePt Thin Films", ***Applied Physics Letters***. **81** 3612 (2002).

List of tables

List of figures

List of symbols

1. A - exchange energy density
2. AFC - antiferromagnetically coupled media
3. BV - bit volume
4. d - the interplanar spacing of the diffracting plane
5. D - average grain size
6. H - applied external field
7. H_c-coercivity
8. H_k - anisotropy field
9. J - the exchange integral
10. K_1 - the first order anisotropy
11. K_B - the Boltzmann constant
12. K_u - anisotropy constant
13. $L1_0$ - ordered phase with AuCu intermetallic structure
14. M_s - saturation magnetization
15. T - temperature in degrees Celsius
16. T_c - Curie temperature
17. V - magnetic switching volume
18. σ - grain size distribution
19. μ-the spin quantum number
20. λ- the wavelength
21. δ - domain wall thickness

22. λ- the wavelength

23. γ - domain wall energy

24. τ- relaxation time

25. θ - the angle of the incidence and of the diffraction of the radiation relative to the reflecting plane

List of abbreviations

1. AFM - atomic force microscopy
2. AGFM - alternating gradient force magnetometer
3. AXS - anomalous x-ray scattering
4. BF - bright field
5. DC - direct current
6. DCD - direct current demagnetization
7. DF - dark field
8. DSI - Data Storage Institute
9. FFT - fast Fourier transform
10. FWHM - full width at half maximum
11. HAMR - heat assisted magnetic recording
12. HRTEM - high resolution transmission electron microscopy
13. hcp - hexagonal close-packed
14. LMR - longitudinal magnetic recording
15. LRO - long-range order
16. MFM - magnetic force microscopy
17. fcc - face center cubic
18. fct - face center tetragonal
19. IRM – isothermal remanence
20. MBE – molecular beam epitaxy
21. PMR - perpendicular magnetic recording

22. RF - radio frequency

23. SAED - selected area electronic diffraction

26. SNR - signal-to-noise ratio

24. SRO - short range order

25. SQUID – superconducting quantum interference device

26. TEM - transmission electron microscopy

27. UHV - ultrahigh vacuum

28. VSM - vibrating sample magnetometer

29. XPS - X-ray photoelectron spectroscopy

30. XRD - X-ray diffraction

Chapter 1 Introduction

A data storage device is to be used for recording (storing) information (data). The storage device may hold information and process information. Today, one of most important data storage devices is hard disc drive. In a hard disk drive, the information is stored in magnetic bits (magnetic domains) of the ferromagnetic granular film.[1] There are two different techniques of magnetic recording - namely longitudinal magnetic recording (LMR) and perpendicular magnetic recording (PMR). In a longitudinal magnetic recording medium, the magnetic domains (bits) are written parallel to film plane and the magnetic film is usually required to possess a longitudinal magnetic anisotropy. On the other hand, a perpendicular magnetic anisotropy is necessary for a perpendicular magnetic medium, as their magnetic bits are written in the perpendicular direction. The current trend in the hard disk industry is to replace longitudinal magnetic recording by perpendicular magnetic recording, as the perpendicular magnetic recording has a much higher potential in recording density.

1.1 History of magnetic recording

The magnetic hard disk drive featuring a total storage capability of 5 Mbit at a recording density of 2 Kbit/in^2 was invented at IBM in 1956.[1] Since then, the areal density has frequently been quoted as a key measurement of the remarkable progress being made in magnetic recording technology. Figure 1-1 shows the growth trend of the areal density from the invention of hard disk drive in 1956. Throughout the 1970s

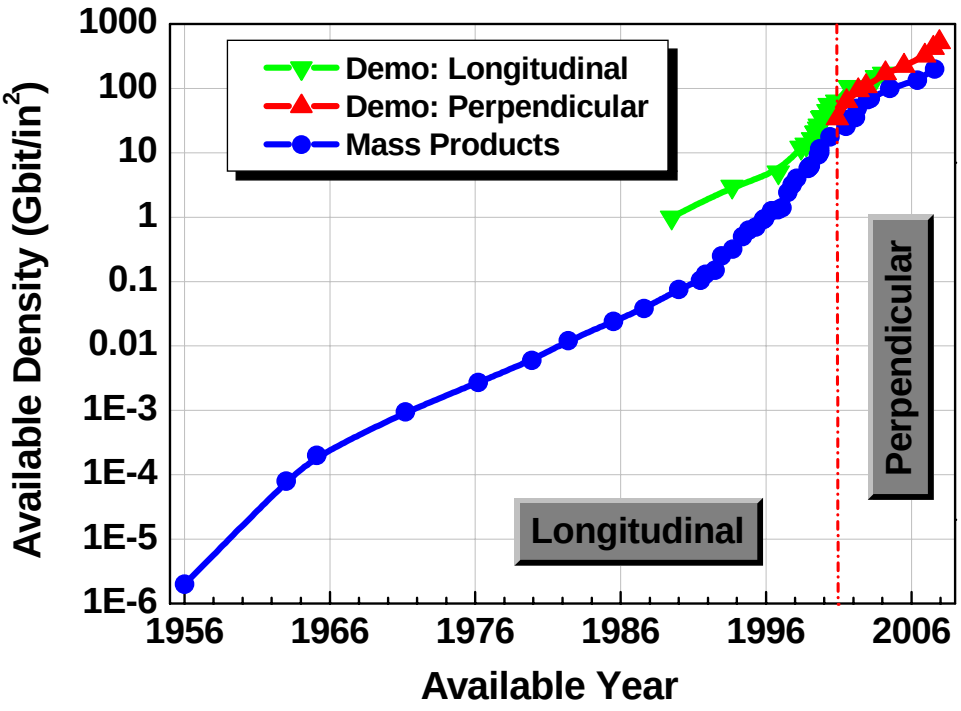

Figure 1-1. Areal density growth curve of magnetic recording media from 1956. Solid circle – mass products trend; down-triangle – demonstration of LMR; upper-triangle – demonstration of PMR; Growth in areal density has accelerated in the past decade. Earlier, density doubled every three years or so; with the introduction of magnetoresistive read heads (MR) in 1991 the doubling time was reduced to two years; since the giant magnetoresistive head (GMR) reached the market in 1997, density has been doubling each year. Before 2001, all of the mass products and most of the lab demonstration is LMR. From 2001, PMR is demonstated to achieve high areal density (Adapted of B. Hayes, 2002, *Ref. 1*).

to 1980s, the bit density increased at a growth rate of about 25 percent per year, which corresponds to a doubling time of roughly three years.[2] With the using of the magnetoresistive (MR) head, the annual growth rate jumped to about 60 percent, which is corresponding to a doubling time of 18 months Furthermore, the growth rate increased to 100% with the utilization of giant magnetoresistive (GMR) head, corresponding to a doubling time of one year after 1997.[3-5]

However, the rate of growth has slowed significantly to around 50-60 % every year after 2002. The key limiting factors in achieving high growth rate of areal density

are the superparamagnetic effect in the LMR media.[6-7] When the recording areal density increases, the size of the recording bit decreases and the thermal stability of the magnetic bits decreases. To keep the recording media readable, a minimal signal to noise ratio, *SNR*, should be remained. Since the *SNR* is approximately proportional to the number of grains per bit, the grains must be reduced to achieve considerable *SNR* with increasing of the areal density.[8]

1.2 Limitation of LMR media

From the invention of magnetic recording in 1956, longitudinal recording is widely used to store data. In LMR media, the easy axis is randomly oriented in the plane of the film. To achieve a higher areal density, small grains are required and the minimum bit length is determined by the transition width, which in turn depends on the grain size of the film. Usually the grains are weakly exchange coupled to each other. For strongly exchange coupled grains, the magnetization in neighboring grains aligns parallel, and effectively larger clusters are formed.[9] Thus, a stronger exchange coupling leads to the increase of the effective magnetic cluster size. As a consequence, transition width would be increased. In addition, thermal stability is diminished by the strong demagnetizing field that opposes the magnetization. At low recording density, when the bit length is much larger than the film thickness, the demagnetizing field is small. However, at high areal density, where the bit length becomes smaller than the film thickness, the magnetic charges inherent to LMR are pushed together, and high demagnetizing fields occur. For this limitation, hard disk technology with LMR has an estimated limit of around 100 Gbit/in^2. A decrease of the demagnetization field in

LMR was achieved by antiferromagnetically coupled media (AFC) with extended recording density to 170 Gbits/in^2.[10] In contrast to traditional media, AFC media consist of two ferromagnetic layers that are antiferromagnetically coupled. The opposite direction of the two layers is achieved by an ultra-thin ruthenium (Ru) layer, better known as "pixie dust."[10] The opposite orientation of the magnetization decreases the demagnetizing field. However, with further increase the areal density, the superparamagnetism bottleneck will be reached again and new concepts are required for future magnetic recording media.

1.3 Media requirements for high areal density magnetic recording

Exponential growth in areal density cannot continue forever due to the superparamagnetic limit. The underlying problem is that "permanent magnetism" is not truly permanent; thermal fluctuations can swap the north and south poles. For a macroscopic permanent magnet, such a spontaneous reversal is extremely improbable. But when the bit gets small enough that the magnetic anisotropy energy is comparable to the thermal energy of the bit, the stored information will be quickly lost, termed as superparamagnetism. This is a technical challenge how to reduce the bit size and to avoid superparamagnetism at the same time. The requirements for ultrahigh areal density magnetic recording are reviewed in this section.

1.3.1 Signal to noise ratio (SNR)

To achieve magnetic recording with high areal density, it is necessary to use a magnetic recording configuration to write the data and a signal processing system capable to read the data. Therefore, the ratio of single-pulse peak over integrated transition noise power,[11] defined as signal to noise ratio *SNR*, is an important parameter in magnetic recording. The higher the *SNR*, the easier data detection becomes. Magnetic recording media are required to provide a high *SNR* and remain thermally stable over a long period of time. The *SNR* is proportional to the read track-width and the square of the bit length.[11] By grain-counting argument, [12] it is approximately determined by the number of magnetic grains (or switching units) per bit:

$$SNR \propto \frac{BV}{V_g} \qquad (1.1)$$

BV: the bit volume;
V_g: the grain volume.

Equation (1.1) indicates that a large number of grains in a bit can result in a high value of *SNR*. Therefore, small grain size is required in recording media with high areal density.

In addition, the *SNR* depends not only on the average grain size *D*, but also on the distribution of grain size. Increasing of the range of distribution decreases the *SNR*. If grains are not uniform, the big magnetic clusters may cause big zigzag regions between two recording bits and result in a large transition noise. As a result, uniform grains could enhance *SNR*.

1.3.2 Thermal stability

Decreasing grain size could result in thermal instability of the recording media. In order to prevent thermal instability, a minimum factor $K_uV/K_BT > 60$, is required for a data storage time of 10 years,[13, 14] where K_u and V are the anisotropy energy density and grain volume, respectively. The magnetic relaxation time τ is an exponential function of the grain volume:[15]

$$\tau = 10^{-9} \exp\left(\frac{K_u V}{k_B T}\right) \qquad (1.2)$$

τ: relaxation time;
K_u: anisotropy constant;
V: magnetic switching volume;
K_B: the Boltzmann constant;
T: is the temperature in degrees Kelvin.

The volume V of a magnetic grain typically decreases with increasing areal density; hence, materials with higher K_u are needed to maintain the sufficient stability. The grain size cannot be infinitely decreased because thermal instability due to the critical grain size of superparamagnetism. As a result, the limitation of magnetic recording is determined by the decay of *SNR* due to thermally induced magnetization fluctuation. To meet the requirement of ultrahigh areal density recording media, some new concepts of magnetic recording are proposed to maintain high SNR ration and keep high thermal stability.

1.4 Perpendicular recording media (PMR)

Although antiferromagnetically coupled AFC magnetic recording has significantly pushed forward the area density of LMR to around 170 Gb/in^2, LMR could not go further because of the inevitable superparamagnetism phenomena. In

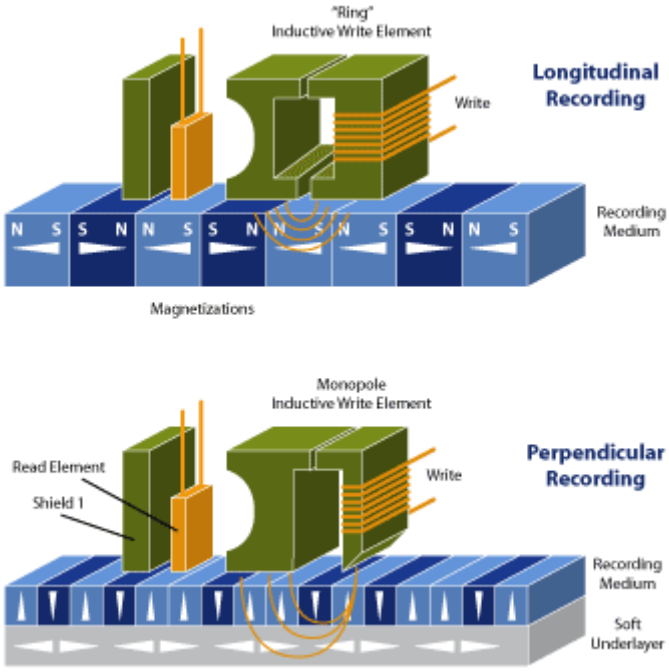

Figure 1-2. Schematic representation of (a) longitudinal recording media and (b) perpendicular recording media. "Ring" inductive head is used in the longitudinal recording media and monopole inductive head is used in perpendicular recording media. (Courtesy of D. Weller and A. Moser, IEEE Trans. Magn. 35, 4423 (2000), Ref. 6)

addition, the random distribution of magnetic easy axes of the grains in a LMR medium can cause a broadening of the transition between the bits. PMR with high thermal stability has been as a promising technique to achieve an areal density beyond 1 Tbit/in^2.[16] Figure 1-2 shows the schematic illustration of LMR and PMR media. In conventional longitudinal media, the easy axis of the grains is randomly oriented in the film plane, leading to a broadening of the transition between the bits.

The idea of PMR is to write the magnetic bits with magnetization directions perpendicular to the film plane.[17] To achieve a perpendicular magnetized configuration, textured films with easy axis perpendicular to the film plane are usually required. Another advantage of aligned grains in perpendicular recording is a narrow switching field distribution. PMR has received considerable attention when Iwasaki

and Nakamura[18] first demonstrated the PMR at 50 Kfcpi by writing with an auxiliary-driven single-pole probe head on a CoCr single layer thin film having perpendicular magnetic anisotropy and reading with a ring head.

1.4.1 Advantages of PMR

In an environment where the areal density is limited by grain-size in the recording medium as dictated by thermal stability, perpendicular recording promises several key advantages:[19]

Firstly, PMR employs a polar magnetic head that is different to ring head for LMR. The pole-head/soft underlayer configuration can give about twice the field that a ring head produces.[20] A higher head field allows the use of media with high coercivity and high anisotropy energy density, K_u. This in turn allows media with "grains" (switching units) that have smaller volume and can support higher areal density. At the same time, relatively thicker media films and larger grain volume can be used to perpendicular recording.

Secondly, sharp transitions can be obtained on relatively thick media. For media with coercivity significantly greater than the saturation magnetization and with high intrinsic squareness, the demagnetizing fields do not necessarily broaden the transitions during writing and storage. Also, the head field and field gradient are better maintained and controlled through a soft underlayer. Thicker media allow more grains per unit area for a given grain volume, and hence result in higher areal density.

Thirdly, the edge effects during writing may be significantly reduced. The field configuration of the edge of the head is similar to that in the down-track

direction. A sharp track edge with minimal erase band facilitates the low bit aspect ratios anticipated for the highest areal density.

Fourthly, short wavelengths are relatively easy to write and to maintain in perpendicular media. This is advantageous because of the difficulty in maintaining strong writing fields at high frequencies and because of the severe short wavelength losses that have to be overcome during readback. During writing, for example, the demagnetizing fields increase the transition separation in an isolated bit and thus compensate for poor field rise time.

Last but not the least, perpendicular media can naturally have a strong uniaxial orientation. This should lead to a tight switching-field distribution and sharper written transitions. There should also be higher signals and less noise in well-oriented media.

1.4.2 Media for PMR

As shown in Figure 1-1, LMR has dominated in the commercial products and lab demonstration before the year of 2001. When LMR was approaching of the superparamagnetism limitation, commercial PMR product debuts in 2001 with areal density of 100 Gb/in^2. The media requirements for high areal density perpendicular magnetic recording are high anisotropy magnetic with magnetic easy axis aligned in perpendicular direction of the media.

CoCrPt alloys have been used as LMR media from 1995. Similarly, The material used for the recording layer of the current PMR media was also CoCrPt alloys. A detailed review on the perpendicular recording media has been made by S. N. Piramanayagam.[21] The CoCr alloy was the PMR media proposed by Iwasaki in the

late 1970s.[18] Since then, modifications of Co alloys such as CoCrPt, CoCrTa, CoCrNb, CoCrPtNb, and CoCrPtB were used as the recording layer material.[22-24] Till today, CoCrPt alloys that doped with oxide such as SiO_2[25] and TiO_2[26] are serving as the recording layer of PMR media. That is the anisotropy energy of the PMR recording media is not significantly increased with respect to that of LMR media. Therefore, in order to achieve higher areal density, magnetic alloys with higher anisotropy energy are required for future magnetic recording media. As shown in Table 1-I, FePt and rare-earth containing compounds ($Nd_2Fe_{14}B$ and Sm-Co) possess much higher magnetic anisotropy compared to that of CoCr based alloys (as used in today's media). The very poor chemical stability of rare-earth containing compounds ($Nd_2Fe_{14}B$ and Sm-Co) limits the application as tin films for magnetic recording. Therefore, FePt is identified as a very promising candidate for the next generation of magnetic recording media with an ultra-high recording density.

1.5 General properties of FePt alloys

As described in the previous section, perpendicular recording media have higher thermal stability than LMR media. The magnetic recording media for high areal density require a high anisotropy energy density. Table 1-I summarizes the intrinsic magnetic properties of a number of potential alternative alloys.[2] As seen in Table 1-I, face centered tetragonal (*fct*) $L1_0$ FePt with very high magnetocrystalline anisotropy and a high magnetization is a promising candidate for the future perpendicular recording media.

Table 1-I. The intrinsic magnetic properties of a number of potential alternative media alloys. (Courtesy of R. Wood, 2002, *Ref. 2*)

	Materials	K_u (10^7erg/cm^3)	M_s (emu/cm^3)	H_k (kOe)	T_c (K)	δ_w (Å)
Todays' media	**CoPtCr**	**0.2**	**300**	**14**	**-**	**222**
Multilayer	**FePd**	**1.8**	**1100**	**33**	**760**	**75**
***L*1$_0$**	**FePt**	**7**	**1140**	**120**	**750**	**39**
Rare earth	**$Fe_{14}Nd_2B$**	**4.6**	**1270**	**73**	**585**	**45**
Amorphous	**$SmCo_5$**	**11-20**	**910**	**240-400**	**1000**	**22-30**

where,

K_u: represents the magnitude of the magnetic anisotropy energy density;
M_s: the saturation magnetization of the material;
H_k: the anisotropy field, $H_k = K_u/2\pi M_s$;
T_c: the Curie temperature;
δ_w: domain wall thickness.

The physical properties of the FePt alloy were first systematically studied in 1907.[27] A transformation between ordered and disordered phases was observed in the equiatomic composition range, which was confirmed by measurements of X-ray spectra,[27,28] magnetic,[29,30] electrical,[31] and mechanical[32] properties. Kussman and Rittberg found three stable crystal structures in the iron-platinum system: $FePt_3$, FePt, Fe_3Pt.[33]

1.5.1 Crystallographic Structure of the FePt phases

The phase diagram of the iron-platinum system was documented by Hansen and Bozorth.[33] The phase diagram of FePt alloy is characterized by the *A1* phase, which is a solid solution phase in the whole composition range at high temperature, as

shown in Figure 1-3. The crystal structure of the high temperature solid solution phase is a disordered face-centered-cubic (*fcc*) structure, in which Fe and Pt atoms statistically occupy the crystallographic sites. The *fcc* phase is not useful for magnetic recording media because it does not possess a high magnetic anisotropy and it is a soft magnetic phase. If the *fcc* phase is present, the structural phase transformation occurs when the solid solution $Fe_{1-x}Pt_x$ alloys are annealed at high temperatures and then cooled to room temperatures. $Fe_{1-x}Pt_x$ alloys that can be used as permanent magnet materials are found around the equiatomic composition where the disordered *fcc* phase transforms into an ordered face-centered-tetragonal *(fct)* phase (Fig. 1-4).

In 1941, Lipson et al. determined that the ordered *fct* phase of the FePt alloy has a CuAu type structure with lattice parameters a = 3.838 Å and c = 3.715 Å.[30] The

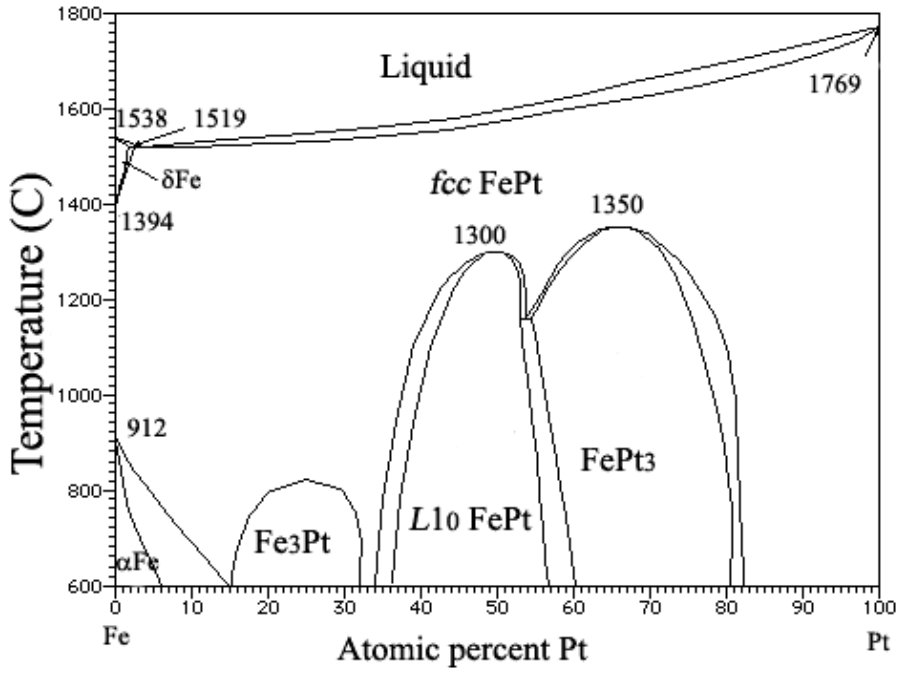

Figure 1-3. Schematic for bulk FePt phase diagram. FePt with atom ratio of about 1:1 and $L1_0$ structure is a promising candidature for perpendicular magnetic recording. (Courtesy of K. Watanabe and H. Masumoto, 1983, *Ref. 47*)

structure is shown in Figure 1-4, along with the *fcc* structure of the disordered alloy. The ordered structure has a primitive tetragonal Bravais lattice (P).[30] In metallurgical nomenclature, it is known as the $L1_0$ phase. The crystal space group is denoted as P4/mmm. The $L1_0$ phase is an ordered *fct* superstructure with Pt at the (0 0 0) and (½ ½ 0) sites and Fe at the (½ 0 ½) and (0 ½ ½) sites.

With the rearrangement of the atoms, the number of equivalent positions within the unit cell decreases; that is, the symmetry of the structure decreases by a factor of three, from 48 for the point group m3m of *fcc* structure, to 16 for the 4/mmm of $L1_0$ structure. Fe and Pt atoms are stacked layer by layer in the crystal unit (Fig. 1-4), which decreases the symmetry of the FePt crystal and increases the number of diffraction spots per unit volume of the reciprocal space. These additional reflections are termed as "superlattice" reflections. Reflections from the disordered crystal (higher symmetry)

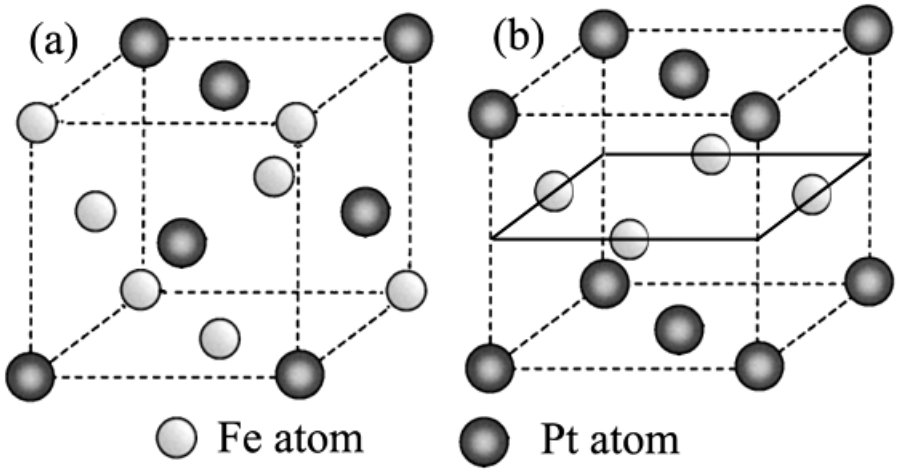

Figure 1-4. Schematic representation of structure transformation between *fcc* (a) and $L1_0$ FePt (b); white ball – Fe atom; black ball – Pt atom; Fe and Pt atoms were randam distrubited in the lattice, while Fe and Pt atoms were layer by layer stacked $L1_0$ FePt lattice.

are called fundamental reflections. The superlattice reflections usually have lower intensity than the fundamental reflections.[34]

1.5.2 Magnetic properties of the ordered phase FePt

The magnetic properties of FePt alloys have been studied since the 1930's. Fallot determined that the equiatomic alloy is ferromagnetic with a Curie temperature of 770 K.[35] The FePt $L1_0$ alloy has a uniaxial magnetocrystalline anisotropy, and K_1 has been measured to be 7.0×10^7 erg/cm^3 for bulk alloy.[36] A similar value, $K_1 = 6.0\times10^7$ erg/cm^3, has been measured for thin films.[37] On the contrary, the disordered alloy has a much lower anisotropy of $K_1 = 6.0\times10^4$ erg/cm^3.[37] The ordered phase has a saturation magnetization of 1150 emu/cm^3 at 298 K.[36] Because of its high anisotropy and large saturation magnetization, the ordered $L1_0$ FePt is considered as an attractive candidate for magnetic recording media.

The quenching of the orbital moments is best realized in 3*d* metals (such as Fe) where there is a strong coupling between the orbital moment and the crystal field. In high spin-orbit atoms such as Pt, the 5*d* electrons are less localized. The quenching of the orbital moments is less completed and the spin-orbit coupling is considerably more important in Pt.[38] Alloys having high spin-orbit components are expected to have a much stronger coupling with the underlying lattice. This is clearly illustrated in the case of FePt. For this intermetallic, the Fe and Pt atoms form alternating planes in the face-centered tetragonal (*fct*) $L1_0$ phase (Fig 1-4), creating a highly anisotropic crystal. Because the spin is more tightly bound to the lattice, the magnetic properties are also highly anisotropic.[39]

Simopolous[40] noted that in FePt alloys, platinum is a "nearly magnetic" metal because its electron configuration almost shows a spontaneous magnetic moment. The theoretical calculation of magnetocrystalline anisotropy from spin-polarized band calculation yielded a K_u value of 1.6×10^8 erg/cm^3.[39] The high uniaxial anisotropy is attributed to the large spin-orbit coupling of the Pt atom and strong hybridization of Pt *d* bands with highly polarized Fe *d* bands.[41] Magnetocrystalline anisotropy energy increases with respect to the increase of the *c/a* ratio of the axis in a certain range.[41]

According to the features of the high density magnetic recording media, high magnetocrystalline anisotropy is required. However, the disordered FePt phase is usually the major phase in the as-prepared alloy.[42] The disordered phase has to be transformed into the ordered phase with a high magnetic anisotropy before FePt can be utilized as recording medium. In the next section, the research works of the phase transformation from disordered to ordered FePt phase will be reviewed.

1.6 Disordered/ordered phase transformation

At the beginning of 1950s to 1970s, most of the studies on FePt alloy were concentrated on the bulk materials.[29,30,32] With the development of technology of vacuum and sputtering deposition after 1970s, more and more studies on FePt alloy have been focused on the thin films. In this section, the phase transformation is discussed in terms of bulk material, nanoparticles and thin films. Finally, attempts to reduce the temperature of phase transformations are reviewed.

1.6.1 Bulk FePt Alloy

The magnetic properties of FePt alloy were not widely investigated until the 1970s. In 1965, Shimizu and Watai reported FePt equiatomic alloy with a coercivity greater than 7 kOe.[43] They found that the high coercivity could be obtained by heat treatment of a totally disordered FePt alloy to form the ordered phase. The disordered phase may be frozen by quenching.[29,30] However, the ordering kinetics is so fast that it is difficult to obtain a completely disordered phase.[41] Consequently, quenching was followed by a plastic deformation in order to get a high degree of disorder. Annealing was carried out to achieve the ordered phase. Similar processes were used by others to obtain optimum magnetic hardness.[37,43,44] Although very high magnetocrystalline anisotropy and large coercivity were obtained by heat-treating the bulk FePt alloys, a temperature above 1000 ^{o}C is necessary. The transformation temperature would dramatically decrease in FePt thin films because of the high mobility of the atoms in thin films.

1.6.2 FePt nanoparticles

Self-assembled FePt nanoparticles were first reported by Sun et al.[45] and have a great potential for magnetic recording media with density beyond 1 Tb/in^2. The recent progress in chemical syntheses and self-assembly of monodisperse FePt nanoparticles as well as their potential applications in data storage, permanent magnetic nanocomposites, and biomedicine was also reviewed by Sun.[46]

Since the as-prepared FePt particles have a *fcc* structure and they are magnetically soft, they must be annealed at a high temperature to transform their

structure into the chemically ordered anisotropic $L1_0$ phase in order to obtain the high anisotropy. But the high annealing temperature needed for the transformation usually destroys the self-assembly and the particles will no longer stay isolated.

Several approaches have been attempted to avoid the sintering. In spherical FePt particles, alloying 4 at.% Cu into the system has reduced the ordering temperature from 500 to 400 °C.[47] The same strategy can be applied to chemically made monodisperse FePt nanoparticles. Several classes of monodisperse ternary nanoparticles of FePtCu,[48] FePtAg,[49] FePtAu,[50] and FePtSb[51] have been successfully synthesized by a thermal decomposition and reduction method. The *fcc* to *fct* structure transformation temperature can be decreased to as low as 300 °C.[51]

1.6.3 FePt Thin Films

In the past decade, studies on FePt alloys have been focused on thin films. FePt thin films have been made with very high maximum energy product up to 35.8 MGOe.[36] The magnetic properties of thin films were reported to be different to those of bulk alloys.[52] As in bulk alloys, annealing causes an initial increase and then a decrease in H_c, due to the increase in grain size. In thicker films, e.g., 300 - 400 nm, the magnetic and structural properties are similar to bulk alloys.[53] The transformation temperature from disordered/ordered phase decreases remarkably with deviation from the equiatomic composition.[54] The low transformation temperature of FePt thin films would make FePt as an attractive candidate for future magnetic recording media with ultrahigh density.

For the application of FePt films as recording media, FePt thin films must

possess high coercivity and a nano-grained structure. In general, the as-deposited FePt thin films have the disordered structure and are magnetically soft. In order to form the ordered $L1_0$ phase, the as-deposited films need to be *ex-situ* annealed at a temperature of 600 ^{o}C or higher.[55-56]

Some approaches have been proposed to reduce the transformation temperature of the FePt films, such as doping, using underlayer to introduce suitable strain, and injecting energy by ion bombardment to promote phase transformation.

1.6.3.1 Doping of additive elements

Additive elements have been doped into FePt films to tailor the thin film microstructure and magnetic properties. Doping of elements can be classified into two categories: one may form solid solutions with FePt that has a lower phase transformation temperature. The other kind will not form solutions with FePt and the doping of these elements will increase the mobility of Fe and Pt atoms, resulting in the reduction of the phase transformation temperature. Oxide materials and some metal elements are included in this category.

Cu[47,57-58] has been added to FePt thin films to accelerate the $L1_0$ ordering process so that the desired magnetic properties can be obtained after deposition at lower temperatures and/or after a heat treatment at relatively low temperature for a shorter period. The difference in free energy between the ordered and disordered phases is the driving force in the phase transformation.

Although there is no data reported for the phase transformation temperature of FePtCu alloy, the possible mechanism is explained using the regular solution model.

The Cu in FePtCu ordered alloy is substituted into the Fe site in the FePt alloy, that is, the Cu is in the Fe plane of the $L1_0$ FePt ordered alloy. Then, the difference in free energy between the order and disorder phases is enhanced and the driving force in disorder–order transformation increases. Thus, it leads to a reduction in the ordering temperature of the FePt film.

Materials such as Zr,[59] Ag,[60-68] Au[60, 65], W,[69] B,[70] Ti[71], and Ni[72] may not form solid solution with FePt. However, these elements have shown promise in promotion of phase transformation. The presence of the second phase changes the microstructures. The volume expansion caused by the doped elements may supply large elastic energy to the Fe and Pt atoms, resulting in the promotion of the phase ordering in the FePt film. In addition, the doped materials either introduce domain wall pinning sites to impede the domain wall motion or provide nucleation sites for the ordered $L1_0$ phase crystals or isolate the FePt grains and magnetization reversal changes to coherent rotation.

However, not all elements will improve the magnetic properties of FePt films. For example Cr may degrade the magnetic properties of FePt.[73] The decrease of coercivity is due to the formation of FePtCr alloy which has lower magnetocrystalline anisotropy. Another possible drawback of element doping is that the magnetocrystalline easy axis may be changed by the doped foreign elements. Recently, Zhou et. al[64] reported that the easy axis changed from perpendicular to longitudinal direction when the doped Ag in the FePt films was above 20 vol. %. The change of the direction of easy axis might be caused by the random distribution of Ag in the

FePt thin films.

Nitride and Oxide such as AlN,[74] Si_3N_4,[75] AlO_x,[76] MgO[77-78], and SiO_2[79,80] have also been dopped into FePt films as a insulation matrix to form a granular structure. The magnetic properties of granular thin film are different to those of continuous thin films because the magnetic particles of granular film are isolated. Furthermore, the growth of magnetic particles is constricted by a nonmagnetic matrix during heat treatment. The change in nonmagnetic matrix volume fraction changes the magnetic particles' intergranular distance, average grain size, and particle shape. These parameters all directly affect the magnetic properties of granular thin film.

AlN is found to show a negative effect on promotion of the phase transformation for the formation of ordered FePt films.[74] The in-plane coercivity of the annealed FePt-AlN film was larger than out-of-plane coercivity. The doping of Si_3N_4 has been used to control coercivity of the FePt film and particle size of FePt particles.[75] Among the oxide dopants, SiO_2 is found to be most effective to reduce the domain size and decrease the exchange coupling between FePt grains while the FePt–MgO and FePt–Al_2O_3 films were reported to have strong exchange coupling and medium domain size.[81]

1.6.3.2 Strain induced phase transformation

Generally, FePt thin film that directly deposited onto an amorphous substrate tends to have (111) textured *fcc* FePt film because the (111) plane of the disordered fcc phase is the close-packed plane and has the lowest surface energy.[55,56] After annealed at 550 °C or above, the texture of *fcc* (111) FePt film becomes $L1_0$ ordered

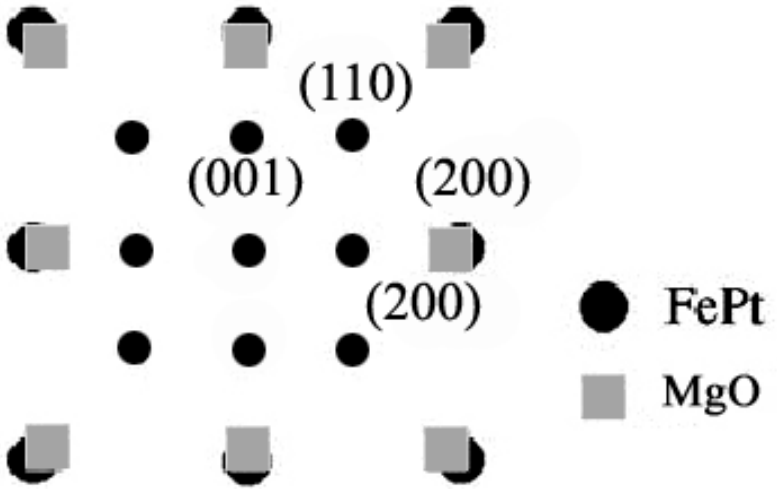

Figure 1-5. Representative schematic for the epitaxial growth of FePt on MgO underlayer; black ball – FePt; gray square – MgO.

with (111) texture. A $L1_0$ FePt film with a (111) texture has the easy axis (001) which forms an angle of 35 ^{o} to the film plane. For the application as the PMR media, the phase transformation temperature must be reduced and the easy axis must be either perpendicular to the film plane. Underlayers such as MgO,[82-84] Ag,[60] and CrRu[86,87] have been employed to reduce the phase transformation temperature and to induce the perpendicular orientation of the FePt easy axis. Figure 1-5 shows the illustration of the epitaxial growth of FePt on MgO underlayer. With the suitable strain and stress introduced by lattice mismatch, the phase transformation temperature of the disordered/ordered phase decreases.[83-84] Usually, thicker underlayer is favorable to achieve lower phase transformation temperature. However, thicker film is not favorable in magnetic recording media.

Exchange-spring magnets are nanocomposites composed of magnetically hard and soft phases that are interacted by magnetic exchange coupling.[88] Hard magnetic FePt phase and soft magnetic Fe_3Pt[89,90] or Fe[91] with nanometer crystalline size are

coupled to enhance the phase transformation and to achieve high energy product. However, the coercivity of the composite FePt film is not very high.[90]

1.6.3.3 Injecting energy by ion irradiation

Ion irradiation has been employed to reduce the phase transformation of the ordered FePt phase.[92-94] The increase in atomic mobility in alloys induced by the ion irradiation at an appropriate temperature can realize the disordered/ordered phase transformation occurring at a reduced temperature. Ion irradiation introduces an appropriate amount of atomic species and desired energy into the films and creates defects or lattice distortion to promote the phase transformation in FePt films. However, the thin films after ion bombardment usually have a large surface roughness and non-uniformity.

In summary, magnetic recording media are reviewed in terms of the LMR and PMR media. The requirements for the high density PMR are also discussed. The ordered $L1_0$ FePt with high anisotropy energy is a promising candidate for the future PMR media. The advantages and disadvantages of possible methods to promote the phase transformation of ordered FePt are summarized in the introduction chapter.

Chapter 2 Research focuses and objectives

2.1 Research focuses

In the previous chapter, the general properties of FePt alloys and the disordered/ordered phase transformation are reviewed. The ordered FePt phase meets the requirements of the high density recording media. However, the high transformation temperature over 400 ^{o}C makes it unsuitable for industrial application. Several methods, such as element doping have been used to fabricate $L1_0$ FePt films at relatively low temperatures. However, there are some inevitable drawbacks of these methods: the magnetization of the FePt alloy is inevitably reduced and the easy axis may be changed in the film with doping.

Layer engineering,[85] is an effective approach to control the microstructure and magnetic properties of the film by modifying or controlling by a well-designed layered structure . With ultrathin layers deposited into the thin film, the modification of the microstructure and magnetic properties of the film may be realized and the above drawbacks may be avoided. The original orientation of the structure will not be changed but certain stress and strain due to appropriate lattice mismatch could be introduced into the structure to promote the phase transformation and therefore to improve the magnetic properties of FePt thin films.

Underlayers have been studied to reduce the ordering temperature of $L1_0$ FePt alloys.[86] So far, relatively little work has been done on the effects of layers added to the FePt magnetic layer. The focus point of this thesis project is to carry out a systematic study on the influence of additional nonmagnetic layers on the FePt films.

The goal of the thesis project is to develop techniques for the fabrication of high-performance FePt films (high coercivity and perpendicular anisotropy) as promising candidates for perpendicular magnetic recording.

2.2 Research objectives

As discussed in the Chapter 1, the high fabrication temperature is not compatible with practical industrial application. Therefore, the objectives of this thesis research project are the fabrication of $L1_0$ ordered FePt thin films at relative low temperature, induction of a perpendicular texture and magnetic anisotropy and high magnetic performance. The effect of additional nonmagnetic layers on the phase transformation of FePt thin films with different substrates is the major objective of the thesis. Furthermore, the correlation between the microstructure, the disordered to ordered phase transformation, and magnetic properties of the FePt films with different additional layers will be studied.

2.2.1 Effects of thickness and temperature

As reviewed in the previous chapter, the film deposition temperature is a vital factor for the phase transformation of the ordered $L1_0$ phase. Many research groups have studied and obtained different results.[95,96] However, no systematic investigations have been reported yet. Therefore, it is necessary to study the temperature dependence of the FePt magnetic properties for the FePt thin films derived from sputtering technique. Film thickness is an important factor that affects the magnetic properties of FePt thin films. Since the saturation magnetization of the $L1_0$ alloys is about 3-4 times

larger than that of the current magnetic recording media of CoPtCrB alloys, $L1_0$ FePt films as recording media may be physically as thin as 5- 10 nm. The thickness of the thin film may significantly affect the diffusion of atoms and thus the ordering temperature of the FePt ordered phase. Hence, it is important to understand how the film thickness affects the magnetic and structural properties of FePt thin films.

2.2.2 Effects of top layer

In the current study, the Ag top layer is expected to diffuse into the FePt layer to increase the mobility of Fe and Pt atoms to reduce the disordered/ordered phase transformation temperature without changing the distribution of the easy axis. Consequently, the coercivity of the thin film may increase with the Ag layer deposited on the top of the film. The morphology, chemical composition and microstructure of the films are characterized by the methods of HRTEM, XPS, and XRD. The exchange coupling in the films is analyzed by the demagnetization measurements (delta M curves).

2.2.3 Effects of intermediate layer

The intermediate layer is an ultrathin layer deposited between two FePt magnetic layers. Small inhomogeneties are expected to form in the magnetic layers. These inhomogeneties may form pinning sites to enhance coercivity of the films. Also the magnetization reversal mechanism is expected to switch from domain wall pinning to nucleation mechanism. Different substrates of corning glass and MgO single crystal are used to investigate the microstructure and magnetic properties of the FePt thin films. The relationship between the phase transformation and the

magnetization reversal mechanism is studied in this section.

A comparison of the effects of the different additive layers in terms of the magnetic properties is conducted in the study. The microstructure of the films with different additive layers is believed to be very critical to the promotion of the disordered/ordered phase transformation.

The work presented in this thesis is a study of the correlations between structural and magnetic properties of FePt thin films. A better understanding of the basic science in magnetic thin films, such as the relation between the microstructure and phase transformation of the FePt films, would provide a future guide for magnetic recording media design. The microstructure and magnetic properties of the FePt thin films with different additive layers are presented in this thesis. In terms of phase transformation and coercivity values, the efficiency of the three different additional layers is compared. With an underlayer added, the crystallinity of the FePt films is expected to increase. Among the three additive layers, the intermediate layer introduces pinning sites to enhance the coercivity and influence the magnetization reversal mechanism of the FePt films. This thesis provides suggestions for reducing the phase transformation temperature of the FePt thin films and provides a reference film structure for industrial application.

2.3 Organization of the thesis

In the introduction part, the media requirements for high areal density magnetic recording and general properties of FePt thin films are reviewed in Chapter 1, and the research focuses and objectives are discussed in Chapter 2.

In the next chapter, the experimental techniques are presented. An introduction to fabrication technique of sputtering and characterization techniques such as XRD, XPS, TEM, vibrating sample magnetometer (VSM), and Magnetic Force Microscopy (MFM) are given.

In Chapter 4, the dependence of magnetic properties of the FePt films on the film thicknesses and deposition temperature is discussed. In order to meet the future requirements as magnetic recording media, the film thickness is kept to be 15 nm and the deposition temperature is fixed to be 400 °C in later chapters (Chapters 5-8).

In Chapter 5, the influence of the additional non magnetic top layers on the microstructure and magnetic properties of FePt films deposited on the amorphous glass substrates will be studied. The properties of different additional layers are discussed in Chapter 6.

In Chapter 7, the additional layers are deposited as intermediate layers between perpendicular FePt films. The enhancement of the coercivity and microstructure of the FePt films with intermediate layers are discussed.

To achieve high crystallization and high coercivity, FePt films are deposited on MgO single crystal substrate in Chapter 8. Nonmagnetic additive layers are inserted between magnetic FePt layers. The promotion of the phase transformation for the ordered FePt *fct*-phase is discussed with the association to the microstructure of the films.

Chapter 3 Experimental methodology

The experimental methods include the fabrication and characterization of the FePt thin films in this thesis. In order to study the magnetic and structural properties of FePt thin films, the first step in the experiment is to fabricate the films by magnetron sputtering. Characterization of the FePt thin films will provide the information for the film structure, FePt phase transformation, crystallographic ordering and texture, and their correlation with magnetic properties. In this chapter, an overview is given on the major experimental techniques used in the thesis, mainly focusing on sputtering and relevant characterization methods used to characterize the structural and magnetic properties of FePt thin films. The magnetization reversal mechanisms are of particular interest in tailoring the magnetic properties of perpendicular recording media. Finally, the magnetization reversal mechanisms are discussed.

3.1 Sputtering method

The sputtering technique is widely used today in the industry for media fabrication. It allows a wide selection of materials to be sputtered.[97] It also produces films of high purity, great adhesion, good uniformity and homogeneity at low cost. Sputtering is the ejection of surface atoms of a solid by the bombardment of energetic particles such as argon. The primary construction of a sputtering system consists of substrate holders and targets. Figure 3-1 shows a schematic drawing of sputtering machine. The targets are connected to a negative voltage supply, which can be either

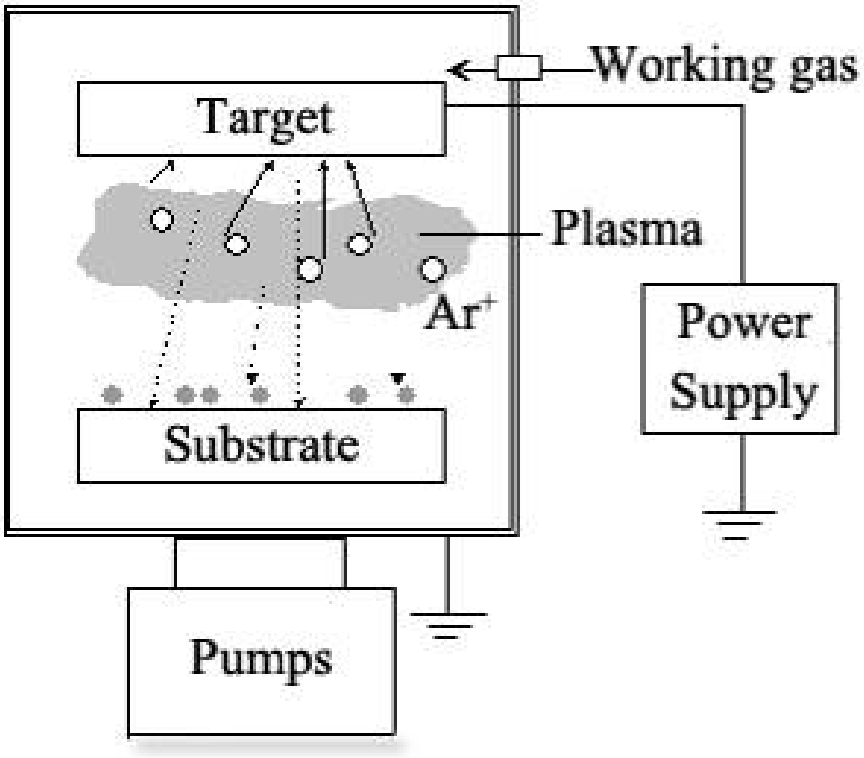

Figure 3-1. Schematic drawing of DC sputtering system.

DC or RF. The substrate holder can be grounded, floating, biased or heated. The chamber is kept in high vacuum by a series of mechanical and Cryo pump. The sputtering gas is normally argon gas or some other inert gas, which has large atomic masses to achieve higher sputtering yield. The function of the gas is to provide a medium in which a glow discharge can be initiated and maintained to continuously supply the bombarding particles.

Sputtering is initiated by applying a negative potential to the target. When the voltage exceeds a threshold value, stable glow discharge appears. In the presence of negative potential, free electrons are accelerated and gas atoms are ionized. The target with a negative potential will attract the argon ions and the argon ions are accelerated towards the target material. As a result, the target materials are displaced and

transferred to the substrate. The potential difference between the substrate and the target must be large enough to allow for effective sputtering. However, if we apply a negative potential to the substrate at the same time, the magnitude of voltage application is known as the bias voltage. That is, the greater the bias voltage, the potential difference between the substrate and the target will be less. The application of bias voltage induces re-sputtering, where some argon ions are attracted to the substrate instead, and therefore transferring some of the deposited materials back to the target.

The sputtering process is controlled by the pressure of sputtering gas, the supplied power, the substrate temperature and the applied substrate bias. These parameters are very important in determining the properties and microstructure of the deposited films. The deposition rate is approximately proportional to sputtering power while the average kinetic energy of the deposited atoms decreases with increasing Ar pressure, due to collisions between the sputtered atoms and the Ar molecules but increases with substrate bias.

Today, the sputtering systems most commonly used are DC and RF sputtering. DC sputtering is a easy configuration. Negative DC voltage that applied to a target will induce the electron acceleration, gas ionization and target bombardment as described in the last section. The substrate is mounted on the anode, facing the target to collect the sputtered materials. The shortcoming of DC sputtering is that, non-electrical conductive materials cannot be sputtered. That is, oxides and semiconductors could not be sputtered because of charging.

Another mode of DC sputtering is the magnetron sputtering. In one of the most common configurations, a magnetic field is generated by a strong magnet behind the target. The electrons from the plasma are confined close to the target. This increases the ionization of the Ar atoms near the target surface and subsequently increases the sputtering rate.

RF sputtering can solve the above problem of charging. The fast response of electrons to radio frequency fields allows electrons to compensate the buildup positive charge on the target. RF sputtering is used for non-electrical conducting material sputtering. However, its application is not limited as it can also be utilized to coat electrically conductive materials.

In the thesis, all the FePt thin films were prepared by DC sputtering process using a home-designed Ultra high vacuum (UHV) sputtering system located in Data storage institute (DSI).

3.2 Microstructure and phase analysis

3.2.1 X-ray diffraction

The phase composition and phase transformation of the samples were examined by means of X-ray diffraction. The instrument for x-ray diffraction involves a x-ray source, which provides the incident beam, and an x-ray detector, which measures the intensity of the diffracted beam emanating from the sample at a certain angle. Diffraction pattern showing peaks and intensity of various crystallographic textures can then be obtained and analyzed.

The simplest and most useful description of crystal diffraction was the Bragg' law, shown in Equation (3-1).[96] Strong diffraction occurs when all the wavelets add up in phase. By considering an entire crystal plane as the scattering entity instead of each individual atom, it can be seen from Figure 3-2 the strongest diffraction results when

$$n\lambda = 2d\sin\theta \qquad (3\text{-}1)$$

Where,

- *n:* the integer representing the order of diffraction,
- λ*:* the wavelength,
- *d:* the interplanar spacing of the reflecting (diffracting) plane and
- θ*:* the angle of the incidence and of the diffraction of the radiation relative to the reflecting plane.

The X-ray-diffraction (XRD) patterns were taken with a Philips PW 1050/37 diffractometer, using Cu K_α radiation. A diffraction angle range of 2θ between 20 ^{o} and 80 ^{o} was chosen using a continuous scanning speed of 0.02 ^{o}/sec. A software program was used to subtract the background and remove the data of the Cu $K_{\alpha 2}$

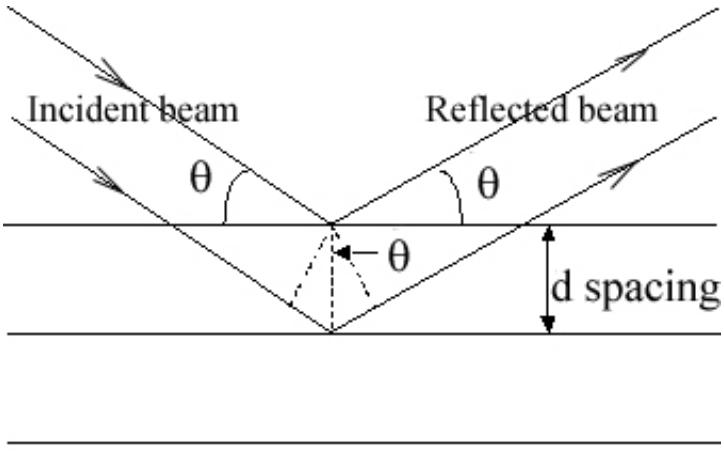

Figure 3-2. Schematic illustration of diffraction of X-ray; θ is the angle of the incidence and of the diffraction of the radiation relative to the reflecting plane; *d* is the interplanar spacing of the reflecting (diffracting) planes.

radiation. The reflections were indexed and the phases were determined by comparing the experimental positions and intensity of the reflections with the corresponding standard patterns. The mean grain size in the samples was evaluated from broadening of the diffraction peaks by Scherrer's equation (3-2):[97]

$$t = 0.9\,\lambda/(B\cos\theta) \qquad (3\text{-}2)$$

where,

t: the mean grain size;
B: full-width at half maximum;
λ: the wavelength;
θ: the angle of the incidence and of the diffraction of the radiation relative to the reflecting plane.

3.2.2 X-ray photoelectron spectroscopy

X-ray photoelectron spectroscopy (XPS, also called electron spectroscopy for analysis, ESCA) is an electron spectroscopic method that uses x-rays to knock electrons out of inner-shell orbitals.[98] The kinetic energy (E_K) of these photoelectrons is determined by Equation (3-3):

$$E_K = h\upsilon - E_b \qquad (3\text{-}3)$$

where,

$h\upsilon$: the energy of the x-ray radiation
E_b: the electron binding energy

The electron binding energies are dependent on the environment of the atom. XPS is therefore useful to identify the oxidation states and ligands of an atom. The detection of photoelectrons requires that the sample be placed in a high vacuum chamber. Since the photoelectronic energy depends on x-ray energy, the excitation source must be monochromatic. The energy of the photoelectrons is analyzed by an

electrostatic analyzer and the photoelectrons are detected by an electron multiplier tube or a multi-channel detector such as a micro-channel plate.

3.2.3 Transmission electron microscopy

In order to investigate the structure and microstructure of the materials, transmission electron microscopy (TEM) observations were performed using a JOEL 3010 electron microscope at an accelerating voltage of 300 kV.[99] A parallel beam of electrons accelerated by a voltage V_0 is transmitted through a specimen (thin foil) and is diffracted in a number of directions by the crystal. The diffracted electron beams are brought into focus in the back focal plane of the objective lens, forming a diffraction pattern that can be magnified and studied. The diffraction pattern consists of a two dimensional array of spots corresponding to a particular set of reflecting planes. From the diffraction pattern one can approximately derive the interplanar spacing d by means of the Equation 3-4, which is derived by Bragg's law.

$$d \approx L\lambda / r \qquad (3\text{-}4)$$

where,

L: distance between specimen and focal plane;
λ*:* the wavelength of the electron beam;
r: the distance of the diffracted spot and the center spot on the back focal plane.

$L\lambda$ is called the apparatus constant. The objective lens also forms an image of the specimen in the image plane. This image can be magnified subsequently by other lenses of the instrument and is finally projected onto the fluorescent screen. Since a set of planes participating in the diffraction is perpendicular to the direction from the diffracted spot to the central spot, one may also find some special crystallographic

directions in image. Using the transmitted electron beam forms a bright-field image and using a diffracted electron beam forms a dark-field image.

3.2.4 Atomic force microscope (AFM)

Sample can be placed under the scanning probe of the AFM that gives the surface image of the sample. Tapping mode™ AFM operates by scanning a tip attached to the end of an oscillating cantilever across the sample. The cantilever is oscillated at near resonance frequency with amplitude ranging typically from 20 nm to 100 nm. The tip lightly "taps" on the sample surface during scanning, contacting the surface at the bottom of its swing. The feedback loop maintains constant oscillation amplitude by maintaining a constant of the oscillation signal by the split photodiode detector. The vertical position of the scanning at each (x, y) data point in order to maintain a constant "setpoint" amplitude is stored by the computer to form the topographic image of the sample. The particle size distribution and morphology of the sample can then be analyzed.

3.3 Magnetic properties

3.3.1 Vibrating sample magnetometer

The vibrating sample magnetometer (VSM) was developed by S. Foner and Van Oosterhart.[100] The VSM is one of the most commonly used equipments for measuring magnetic characteristics, such as hysteresis curve. The schematic diagram of the VSM is shown in Figure 3-3.

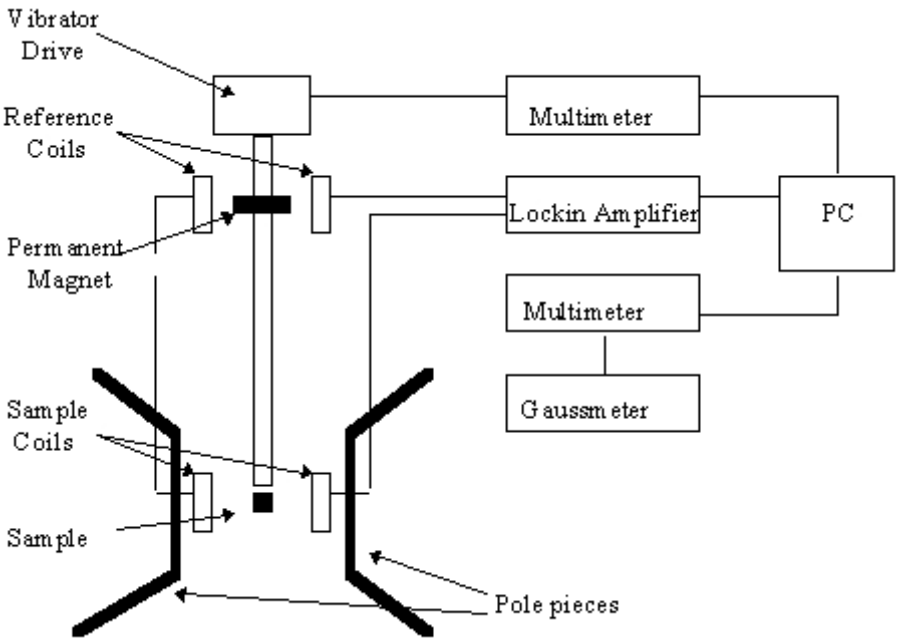

Figure 3-3. Schematic illustration of VSM (adapted from Ref 100).

The sample is mounted at the end of a rigid rod attached to a mechanical resonator, which oscillates the sample at a fixed frequency. The movement of the sample in the applied magnetic field alters the magnetic flux through the pick-up coils, which, according to Faraday's law of magnetic induction, causes an induction voltage in the coils that is proportional to the magnetization of the sample. The in-plane state corresponds to the sample surface parallel to the direction of the applied field, whereas the out-of-plane state corresponds to the sample surface normal to the applied field.

The basic principle of VSM is as follows: a pair of electromagnets applies a uniform *DC* magnetizing field to the sample. The vibrator, which is a nonmagnetic rod, vibrates the sample between the coils of the electromagnets and a region of free

space. According to the Faraday's Law of electromagnetic induction, an *AC* voltage *V (t)* is produced in the pair of pickup coils. This output voltage is then applied to the lock in amplifier and compared with that produced by a standard magnetic sample. And the output signal, which is proportional to the sample's magnetic moment, is sent to an XY plotter, along with the applied field signal from a field sensor. By controlling the electromagnetic field appropriately, any sequence of fields can be applied to the sample. In this work, the VSM is used for obtaining the magnetization curves. The maximum applied field for the VSM in DSI is 15 kOe.

3.3.2 Alternating gradient force magnetometer

The alternating gradient force magnetometer (AGM) has a high sensitivity. The AGM has a noise floor of 10^{-8} emu compared to 10^{-6} emu for VSM. In an AGM, the sample is mounted on an extension rod attached to a piezoelectric element. An alternating gradient field produces a periodic force on a sample placed in an AC field of an electromagnet.[101] The alternating field gradient exerts an alternating force on the sample proportional to the magnitude of the field gradient, the magnetic moment of the sample and the intensity of the applied field. The resulting deflection of the extension is transmitted to the piezoelectric sensing element. The output signal from the piezoelectric element is synchronously detected at the operating frequency of the gradient field. The signal developed by the piezoelectric element is greatly enhanced by operating at or near the mechanical resonant frequency of the assembly. A built-in software function automatically determines mechanical resonance and sets the

appropriate operating frequency for the sample under study. The maximum applied field for the AGM at data storage institute (DSI) is 20 kOe.

3.3.3 SQUID magnetometer

A Quantum Design MPMS-5S superconducting quantum interference device (SQUID) was used for the investigation of the macroscopic magnetic properties of the samples. The SQUID utilizes an extremely sensitive detection method that is capable of measuring magnetization values in the range of 10^{-8} to 10^{7} emu with an accuracy of 0.1 %. The magnetic field was applied along the length direction of the ribbon samples and the plate-like samples, so that the demagnetizing factor can be disregarded. The SQUID with DC magnetic field varied between -70 and 70 kOe was used to measure the high anisotropy thin films grown on MgO substrate.

3.4 Magnetization reversal mechanisms

In thin film recording media, both the micromagnetic behavior and the magnetic interactions among the magnetic grains in the film are very important. The interactions in these films are usually so significant that the reversal mechanisms of isolated individual grains can be altered. In the following section, magnetization reversal mechanisms will be discussed. Magnetization reversal mechanisms may fall into four broad categories: coherent rotation, incoherent rotation, nucleation, and domain wall pinning.

In terms of interaction behavior between grains, magnetization reversal mechanisms can be divided into two sorts: one is Stoner-Wohlfarth mode without

interaction between grains and the other is non-ideal mode with interaction between magnetic domains.

On the other hand, from viewing of the reversal processes, there are two steps involved: (i) an initial phase where reverse domains are nucleated followed by (ii) a phase where reversal occurs by domain wall motion. Therefore, the reversal mechanism can be sorted as nucleation, domain wall pinning modes or mixture (both nucleation and domain wall pinning controlled magnetization reversal).

3.5 Magnetization reversal mechanisms

In thin film recording media, both the micromagnetic behavior and the magnetic interactions among the magnetic grains in the film are very important. The interactions in these films are usually so significant that the reversal mechanisms of isolated individual grains can be altered.[102-103] In the following section, magnetization reversal mechanisms will be discussed. Magnetization reversal mechanisms may fall into four broad categories: coherent rotation, incoherent rotation, nucleation, and domain wall pinning.

In terms of interaction behavior between grains, magnetization reversal mechanisms can be divided into two sorts: one is Stoner-Wohlfarth mode without interaction between grains and the other is non-ideal mode with interaction between magnetic domains.

On the other hand, from viewing of the reversal processes, there are two steps involved: (i) an initial phase where reverse domains are nucleated followed by (ii) a phase where reversal occurs by domain wall motion. Therefore, the reversal

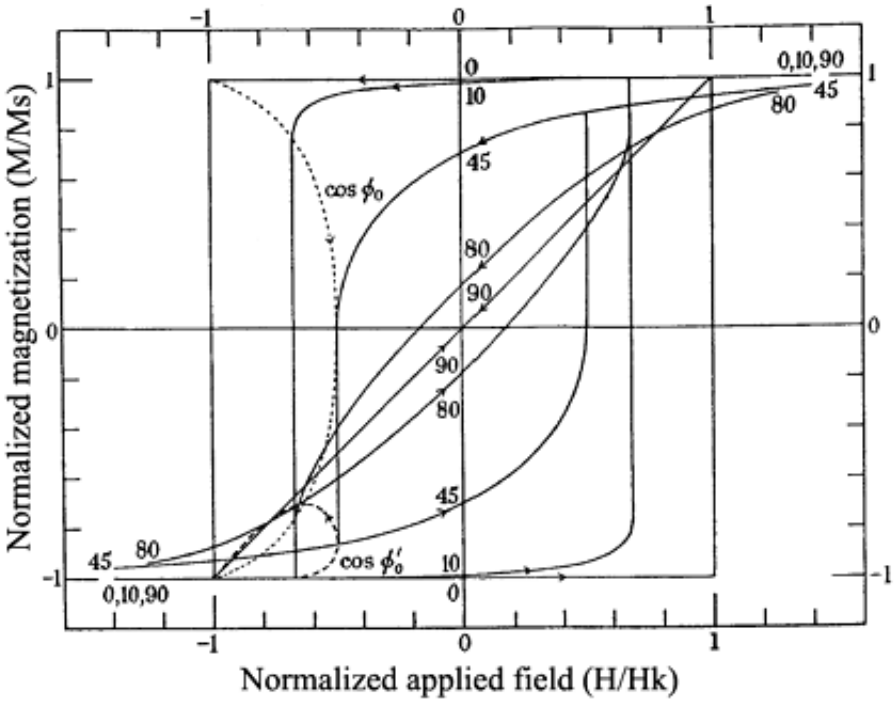

Figure 3-4. The hysteresis curves of Stoner-Wohlfarth particle with different applied field angles θ; the film is with an in-plane magnetization (Courtesy of E. C. Stoner and E. P. Wohlfarth, 1948, *Ref. 104*).

mechanism can be sorted as nucleation, domain wall pinning modes or mixture (both nucleation and domain wall pinning controlled magnetization reversal).

3.4.1 Non-interaction Model: Stoner-Wohlfarth mode

The material is assumed to be uniformly magnetized and to possess uniaxial anisotropy. If a magnetic field H is applied at angle θ to the anisotropy axis, the hysteresis curves with different applied orientations θ can be derived, as shown in Figure 3-4.[103,105] When the field is applied along the easy axis, the magnetization remains at the original saturation state until the external applied field reaches the coactivity. When the applied field is larger than the coactivity, the magnetization

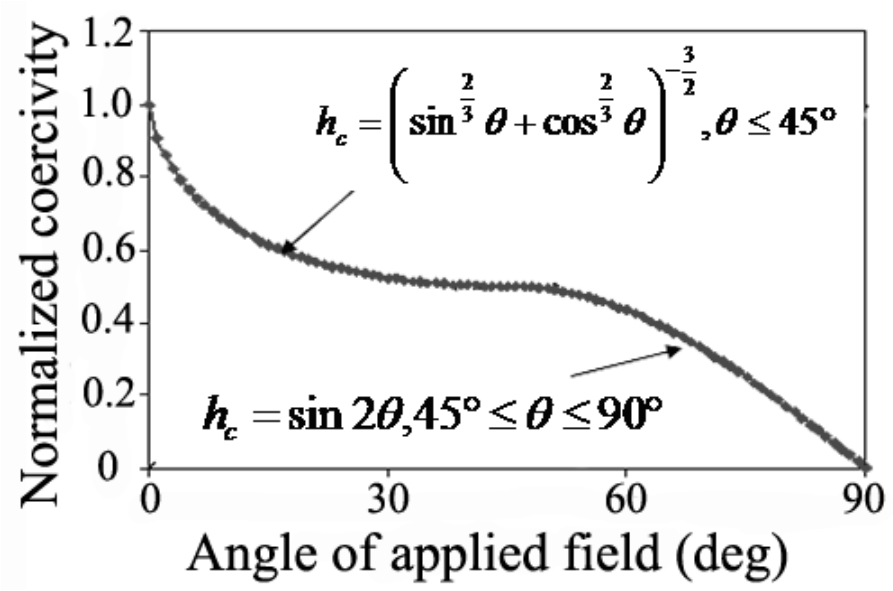

Figure 3-5. Dependence of normalized coercivity of Stoner-Wohlfarth particle with the external applied field direction angle θ; the two functions of coercivity with the range of angle of applied field (θ<45 ^{o} and 45 < θ<90 ^{o}) was stated in the figure.

suddenly reverses its original direction to the opposite direction across the zero magnetization level. The applied field that causes the zero magnetization of the magnetic system is defined as coercivity h_c. For the S-W model magnetic particle, the coercivity with the different applied angle θ is calculated as:

$$\begin{cases} h_c = \left(\sin^{\frac{2}{3}} \theta + \cos^{\frac{2}{3}} \theta \right)^{-\frac{3}{2}}, \theta \le 45° \\ h_c = \dfrac{1}{2} \sin 2\theta, 45° \le \theta \le 90° \end{cases} \qquad (3\text{-}5)$$

The dependence of coercivity on the applied field angle θ is shown in Figure 3-5. When the external field is applied along the easy axis, the coercivity has the largest value of 1. As the applied field angle increases to 90 degree, the coercivity decreases to 0 (Fig. 3-5). In the real case, for the longitudinal medium, there is a distribution along the easy axis. Therefore, the macro-scale coercivity is obtained by

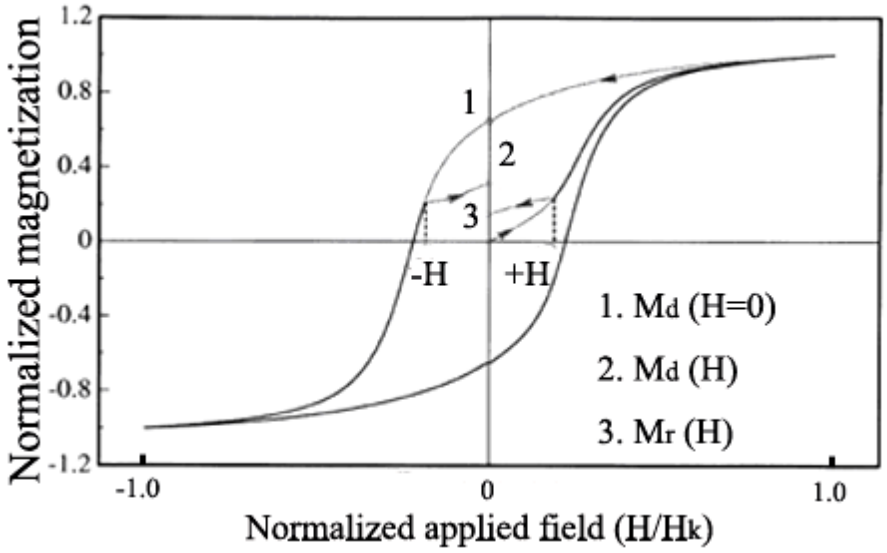

Figure 3-6. Schematic explanation to measure the field dependant magnetisation remanence M_r and demagnetization remanence M_d; 1- magnetization remenence; 2 – *DCD* remanence; 3 – *IMR* remanence. (Courtesy of M. Fearon, 1990, *Ref. 108*).

integrating the angle dependence coercivity with the angle distribution. For the perpendicular recording media, on the contrary, the zero degree refers to the film normal direction.

3.4.2 Interaction model

Interaction effects in particulate magnetic materials can be studied via the interaction model based on the Wohlfarth relation,[104] which links the isothermal remanence (*IRM*) and *DC* demagnetization (*DCD*) remanence curves (Figure 3-6).

The IRM remanence curve is measured on a previously demagnetized material. The material is then subjected to a positive applied field. The applied field is then removed and the remanent magnetization is measured, seen in Fig. 3-6. The cycle is then repeated, incrementing the positive applied field, until saturation is reached. Plotting remanent magnetization versus the previously applied positive field gives the

IRM curve. As only remanent moments are considered, the *IRM* curve shows the progress of the irreversible changes in magnetization.

The *DCD* remanence curve is measured by saturation of the sample in a sufficient high positive applied field followed by applying a certain reversal field. The reverse field is then reduced to zero and the remanent magnetization is measured, seen in Fig. 3-6. The process is then cycled with an incremented reverse field until negative saturation is reached. As with the *IRM* curve, the measurement taken in the applied field contains contributions from both reversible and irreversible magnetization processes, while the remanent measurement contains only the irreversible contribution.

The Wohlfarth relation, which links these two remanence curves, was derived for an assembly of non-interacting single domain particles with uniaxial anisotropy where magnetization reversal occurs by coherent rotation. In reduced units (normalized so that the saturation remanence equals unity), the Wohlfarth relation is:

$$M_d\,(H) = M_r,\, max - 2M_r\,(H) \qquad (3\text{-}6)$$

where,

$M_d\,(H)$ is the DCD remanence;
$M_r\,(H)$ is the IRM remanence;
$M_r,\, max$ is 1.

Equation (3-6) was derived assuming a non-interacting system of particles. Any deviation in experimental data from this relationship can be attributed to the effect of interactions. McCurrie and Gaunt[105] extended the derivation of the Wohlfarth relation to include the case where magnetization reversal is controlled by interaction modes. Kelly *et al.*[106] adopted an analytical approach to describing deviations from

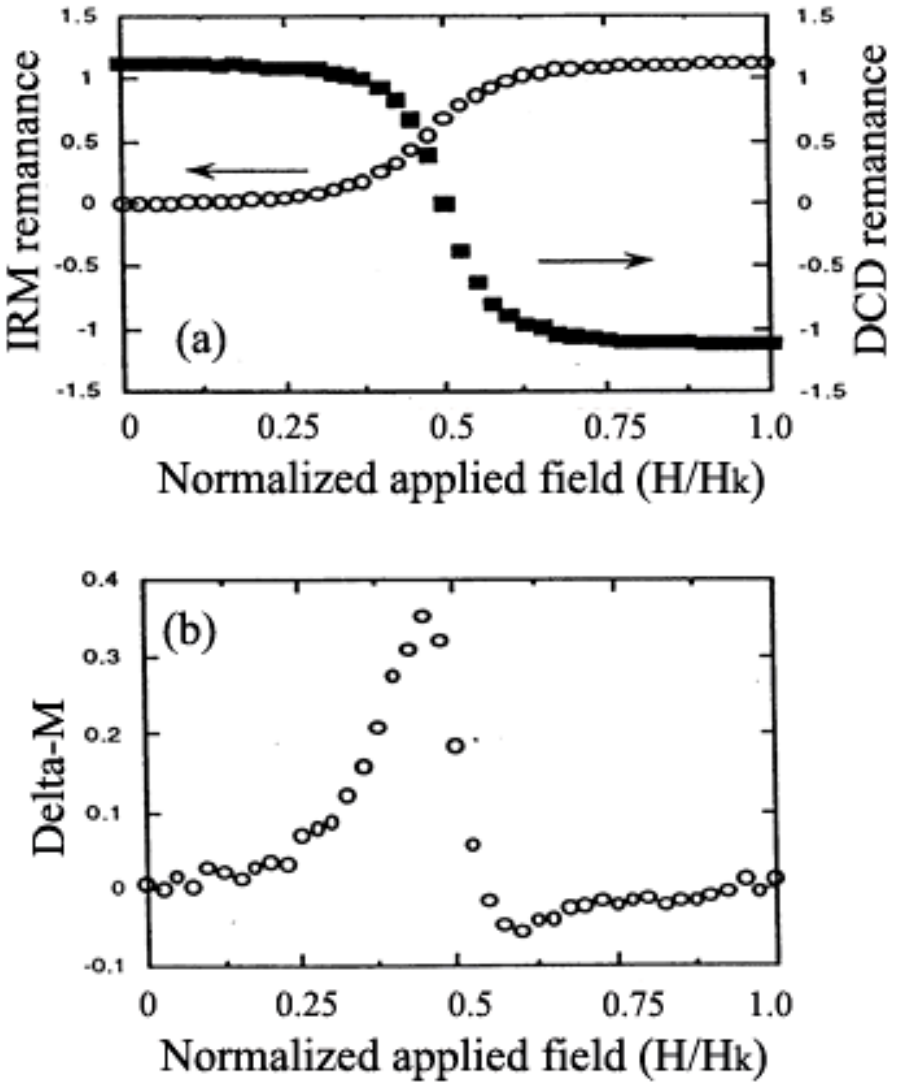

Figure 3-7. (a) Illustration of typical *DCD* and *IRM* curves; blank circle – *IRM* remanence curve; solide square – *DCD* remanence curve; (b) delta-M curve for magnetic thin film media. (Courtesy of M. Fearon, 1990, *Ref. 108*).

linearity and explicitly accounting for interactions by modifying the Wohlfarth relation:

$$\Delta M\,(H) = M_d\,(H) - [M_r,\, max - 2M_r\,(H)] \qquad (3\text{-}7)$$

where,

$M_d\,(H)$ is the *DCD* remanence;
$M_r\,(H)$ is the *IRM* remanence.

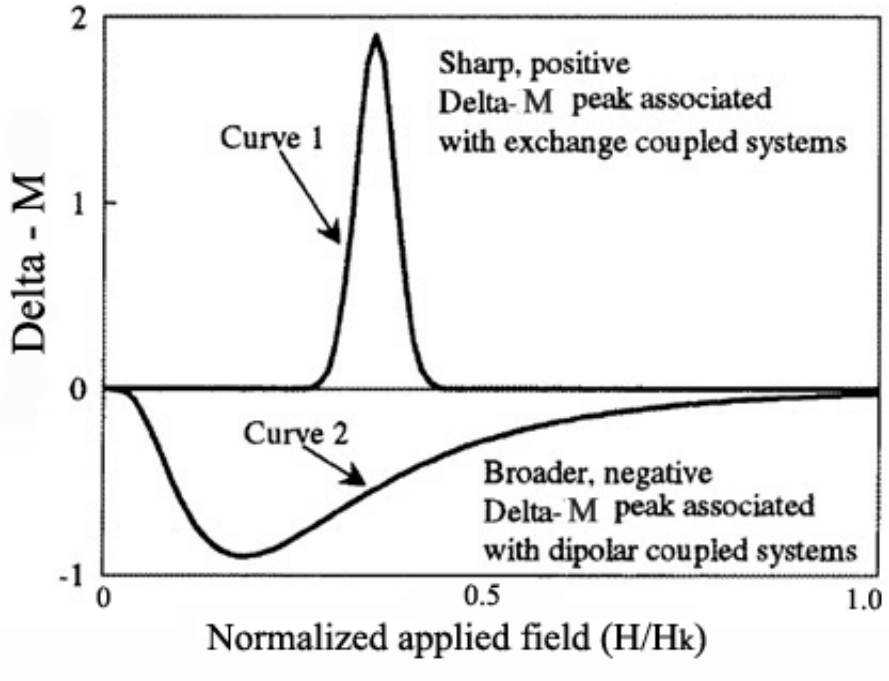

Figure 3-8. Schematic delta - *M* curves illustrating different coupling regimes; Curve 1 showed sharp positive indicates large exchange coupling; Curve 2 showed negative peak indicates small exchange coupling existing in the thin film. (Courtesy of T. Thomson, 1997, *Ref. 111*).

A plot of $\Delta M(H)$ (occasionally written as δM) against H therefore gives a curve characteristic of the interactions present, as seen in Figure 3-7. There are two major types of ΔM curves measured in magnetic thin films. Two such curves are shown in Figure 3-8. A number of conclusions can be drawn when the dominant reversal process is the same for both the *IRM* and *DCD* curves. The first concerns the sign of the $\Delta M(H)$ plot. Positive $\Delta M(H)$ values (curve 1 in Fig. 3-7) indicate interactions that encourage the magnetized state; i.e., the positive $\Delta M(H)$ *implies* magnetizing interactions. Positive $\Delta M(H)$ plots are usually associated with exchange coupled granular systems[107] such as samples having particular structural features. Negative $\Delta M(H)$ plot (curve 2 in Fig. 3-7) implies interactions that attempt to demagnetize the material. Negative $\Delta M(H)$ plots are associated with materials such as

particulate recording media[108-109] where the coupling is dipolar in nature. Thus, we generally associate exchange coupling with positive $\Delta M\ (H)$ plots, and dipolar coupling with negative $\Delta M\ (H)$ plots.

3.4.3 Nucleation and domain wall pinning

The starting point for reversal models of the nucleation and domain wall pinning is a system where magnetization reversal is achieved by nucleation or domain wall motion. Presumably, at saturation, no domain walls exist in the material; thus, before magnetization reversal can proceed, some reversed domains must be created. Therefore, in principle, systems subject to magnetization reversal by domain wall motion undergo a two-stage process: an initial nucleation phase and a subsequent domain wall motion phase. Now the reaction of this system to an applied magnetic field will depend on the relative difficulty of nucleating of reversed domains or moving of domain walls once nucleated. For most materials, this nucleation stage occurs before the application of a reverse field, as the remanent magnetization (M_r) is not equal to the saturation magnetization (M_s). Thus, in order to proceed with this model, the materials under investigation must have a squareness of unity as is generally found in magneto-optic films with perpendicular anisotropy.

Two extreme cases exist. In the first case, the nucleation energy is much less than that required for the movement of the domain walls; in the second, the critical field of domain wall motion is less than the nucleation energy. In materials undergoing magnetization reversing by domain wall motion, the domain wall pinning properties are dominant, rather than the initial formation of reversal domains (as

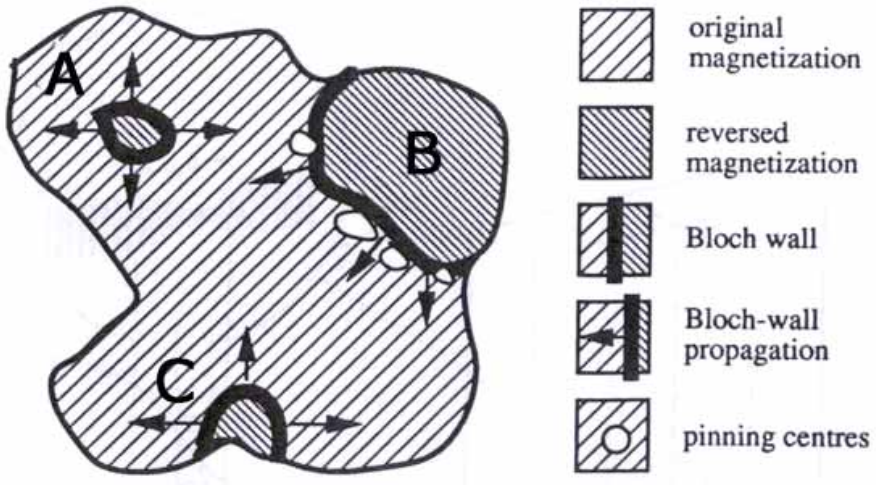

Figure 3-9. Schematic representation of domain, reversal domain, and inhomogeneities in a domain. The icons on the right side represent the original magnetization domains, reversed domains, domain wall, direction of domain wall propagation and defects in the domains, respectively. (Courtesy of J. D. Livingston, 1981, *Ref. 113*).

nuclei). The measured hysteresis for this type is thus determined by the distribution of domain wall pinning fields.

The other extreme case is a system where the nucleation energy is greater than the domain wall pinning energy. In this system, the domain walls, once nucleated, move rapidly through the material until the magnetization reversal is completed. The hysteresis curve in this case is observed as a catastrophic reversal resulting in an ideally square curve.

Figure 3-9 shows the schematic representation of the domain structure and the defects in the domain.[110] Location A is the original domain, and location B and C are the reversal domains. The arrows show the propagation direction of the reversal domains. The white particles denote the defects that act as pinning sites that impede the domain wall motion.

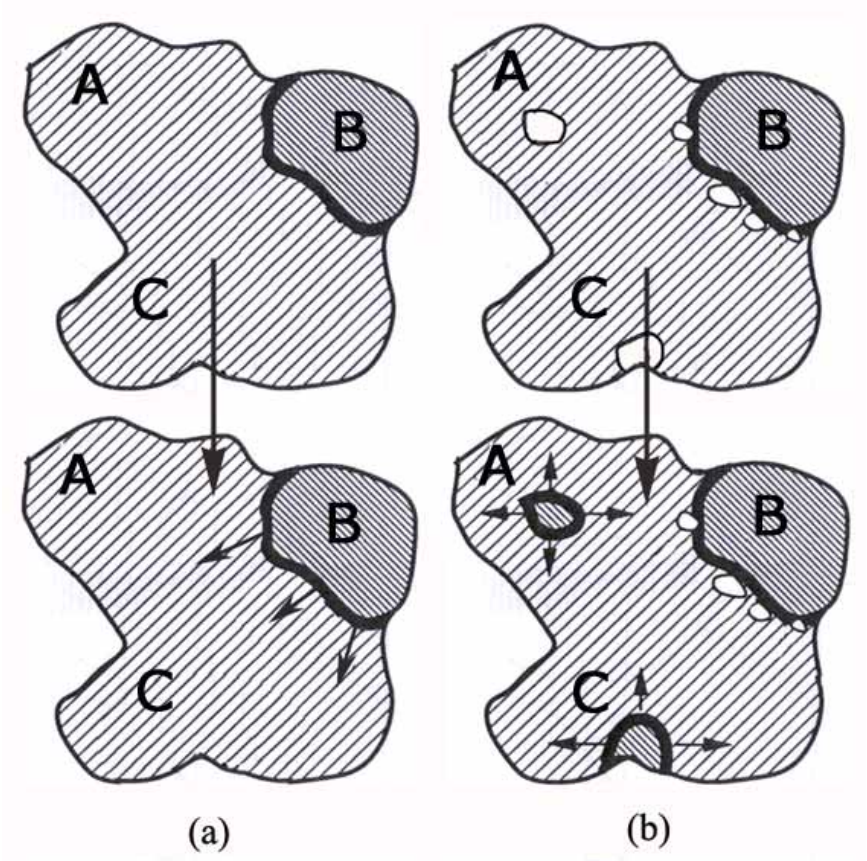

Figure 3-10. Schematic illustration of (a) domain wall motion; and (b) nucleation mechanism domain reverse process. The arrows represent the direction of the domain wall propagation; the illustrations were represented by the icons in Fig. 3-9. (Adapted from J. D. Livingston, 1981, *Ref. 110*).

Figure 3-10 shows the schematics of domain wall motion (a) and the nucleation mechanism (b). The domain wall motion mechanism is a continuous moving propagation of domain wall with few pinning sites that impede the motion of the domain wall (Fig. 3-10a). The nucleation mechanism is a discontinuous, domain nucleation process in which the domain wall motion is limited by pinning sites (Fig. 3-9b).

However, in real materials, the situation may be less clear-cut than the straightforward picture presented above. Since both the domain wall pinning energies

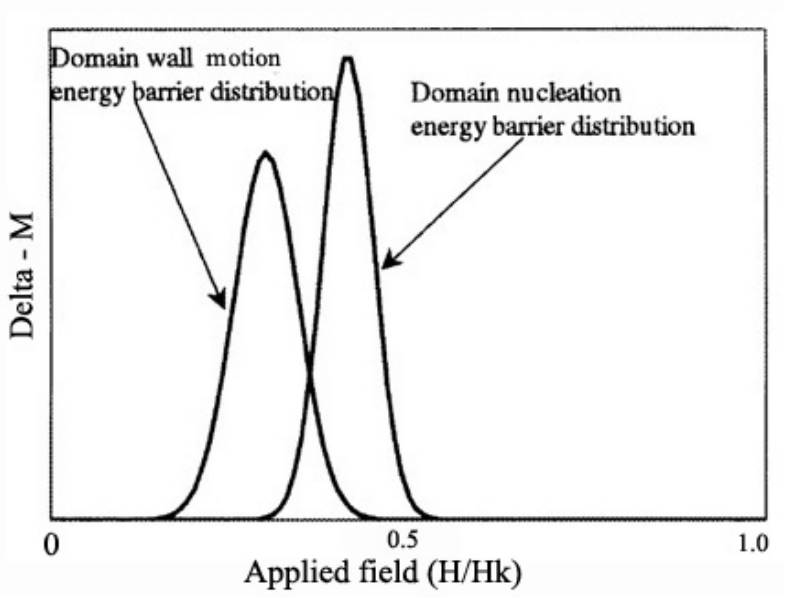

Figure 3-11. Domain wall pinning energy distribution in relation to the reverse domain nucleating energy distribution. The domain wall motion energy barrier distribution and domain nucleation energy barrier distribution peaks are illustrated in the picture. (Courtesy of T. Thomson, 1997, *Ref. 111*).

and the reverse domain nucleating energies are not single valued, the distribution of one in relation to the other must be considered.

Figure 3-11 shows two such distributions overlapping. These overlapping energy barrier distributions lead to a behavior lying between the two extremes described earlier. Thus, the hysteresis properties are modified in that the domain walls, once nucleated, cannot sweep through the entire volume of material without the assistance of additional external energy. This produces a hysteresis loop with an initially square transition followed by a tailing off as reverse saturation is approached. Thus, with the two-coercivity model, magnetization reversal is governed by the relative positions of the domain wall pinning energy barrier distribution and the domain nucleation energy barrier distribution.

Chapter 4 Dependence of magnetic properties of FePt films on film thickness and deposition temperature

As described in the literature review section (Chapter 1), the film deposition temperature is a vital factor for the formation of the $L1_0$ phase FePt. Many research groups have studied the effects of thickness and deposition temperature, and different results have been reported.[75-79] Therefore, it is necessary to study the temperature dependence of the FePt magnetic properties for the sputtered FePt thin films in this work. The film thickness is another factor that affects the magnetic properties of the FePt films. For magnetic recording, thinner media are favorable for the signal to noise ratio (SNR). Hence, it is important to understand how film thickness and deposition temperature affect the magnetic and structural properties of FePt alloy films.

4.1 Experiment methodology

FePt thin films were deposited by the *DC* magnetron sputtering in a high-vacuum system with a base pressure of 5×10^{-8} Torr using an FePt alloy target with the FePt composition ratio of approximately 1:1. High purity argon of 10 mTorr was fed during sputtering. Corning glass substrates were attached to a rotating substrate holder and were heated up to 400 °C prior to the deposition. The maximum temperature in this work is set at 400 °C because a higher deposition temperature may cause the deformation of glass substrate. Two series of FePt films with a nominal total thickness from 5 to 120 nm were prepared. The typical growth rate for FePt was 0.06 nm/s. Crystallographic texture of the films was studied by the in-plane XRD with Cu

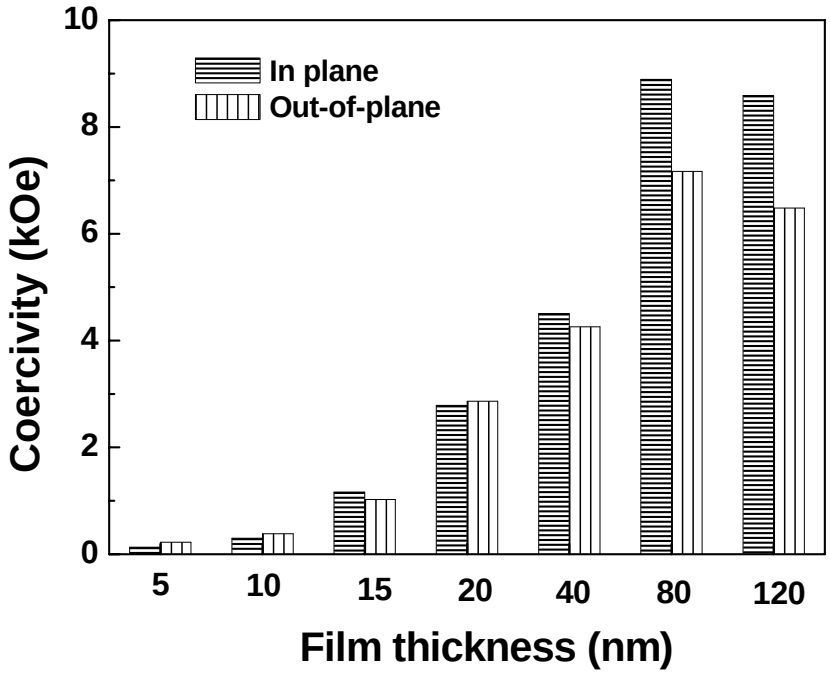

Figure 4-1. In-plane and out-of-plane coercivity for FePt thin films with different thicknesses deposited at 400 °C; dense bars – in-plane coercivity; sparse bars – out-of-plane coercivity; coercivity increases with increase of film thickness.

K_α radiation. Magnetic properties of the films were measured with a vibrating sample magnetometer (VSM) with a maximum applied field of 15 kOe.

4.2 Results and discussion

Figure 4-1 shows the thickness dependence of the in-plane and out-of-plane coercivities with the deposition temperature of 400 °C. For the FePt films with a thickness of 5 and 10 nm, both the in-plane and out-of-plane coercivities were 200 to 300 Oe. The low coercivity indicates that the dominating phase is the disordered *fcc* FePt phase in the these FePt films. With a thickness of 15 nm, coercivity for the films increased quickly to above 1 kOe. Figure 4-2 shows the typical hysteresis loops of FePt films with thickness of 15 nm. Figure a and b show the in-plane and out-of-plane

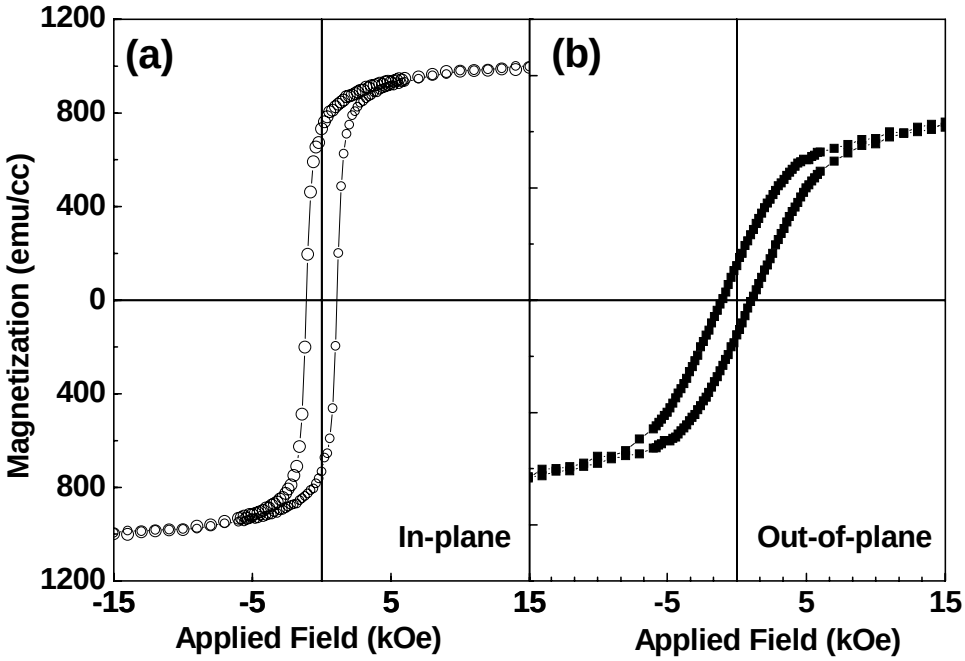

Figure 4-2. In-plane and out-of-plane hysteresis loops for FePt thin films with thickness of 15 nm.

magnetization with the external field applied in the film plane and normal to the film plane, respectively. The curve was saturated at a maximum magnetic field of 15 kOe in the in-plane direction and could not be saturated in the out-of-plane direction. It indicates that the easy axis of FePt film deposited amorphous glass substrate is in-plane direction.

With the thickness increases to 80 nm, the FePt thin film showed the maximum coercivity of 8 kOe in the in-plane direction. Coercivity decreased slightly with further increase of film thickness. The thickness dependence of coercivity behavior was qualitatively similar to that reported for FePt films.[112]

Figure 4-3 shows XRD patterns of the FePt films with the thickness varying from 15 to 80 nm. The (111), and (200) peaks FePt fundamental peaks that belongs to both *fcc* and *fct* phase. The (001), (110), and (112) peaks are characteristic superlattice

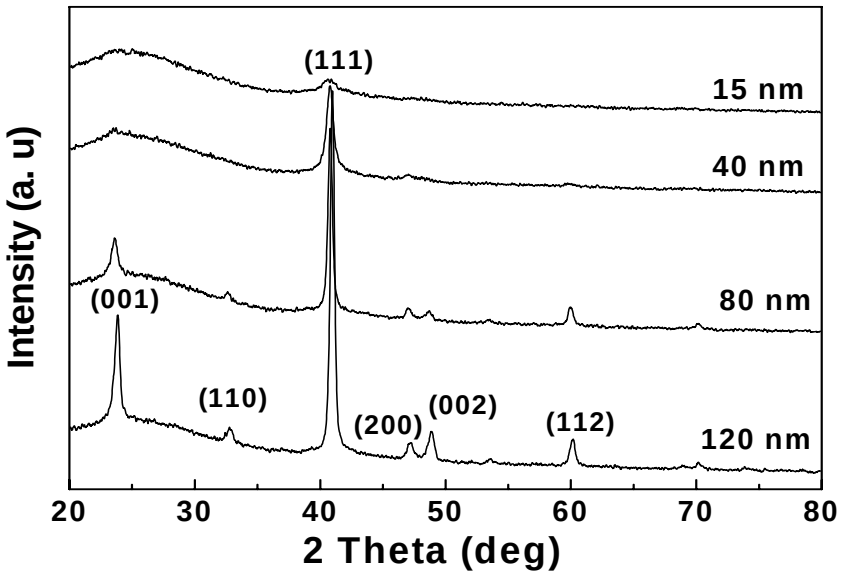

Figure 4-3. XRD patterns for FePt thin films with different thicknesses; with increase of film thickness from 15 to 120 nm, the intensity of the diffraction peaks increase gradually.

peaks of *fct* ordered FePt phase. The XRD profile of FePt film with thickness of 15 nm showed the FePt (111) peak and an amorphous hump at 20-25 degrees from the glass substrate as well. This indicates that the disordered phase is dominating in the film. This explains the small coercivity in films with a thickness less than 15 nm. With increase of the thickness to 40 nm, the characteristic superlattice peaks, such as (001) and (110) peaks appeared in the XRD patterns. With further increase of the thickness to 80 and 120 nm, most of the superlattice peaks appeared and the intensity of the peaks became stronger, as shown in the XRD scan of the FePt thin film with a thickness of 120 nm in Figure 4-4.

Figure 4-5 shows the temperature dependence of the coercivity for FePt thin films with a thickness of 15 nm, when the deposition temperature varied between 300 and 400 °C. With an increase of the deposition temperature, the coercivity of the films increases. The film deposited at 400 °C only has a coercivity of about 1 kOe. It

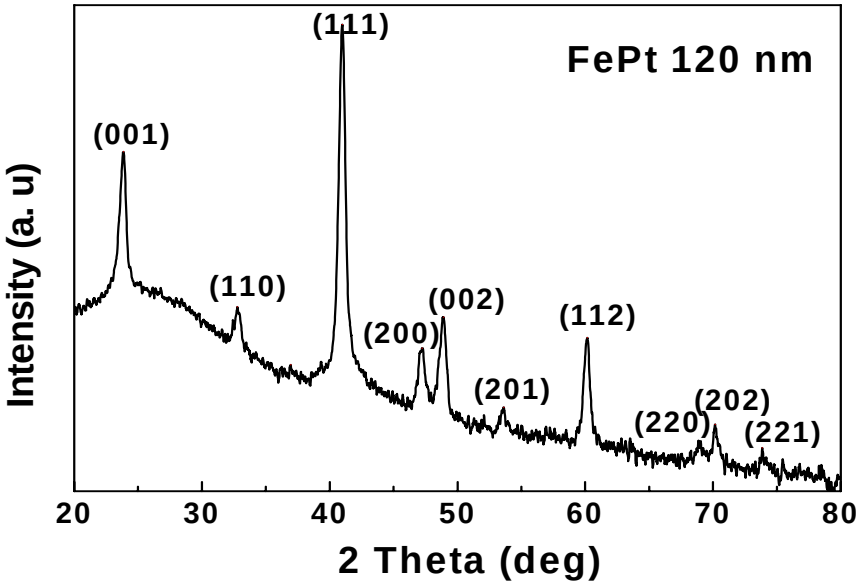

Figure 4-4. XRD patterns for FePt thin films with thickness of 120 nm. Almost all the characteristic peaks of ordered FePt phase are present in the curve.

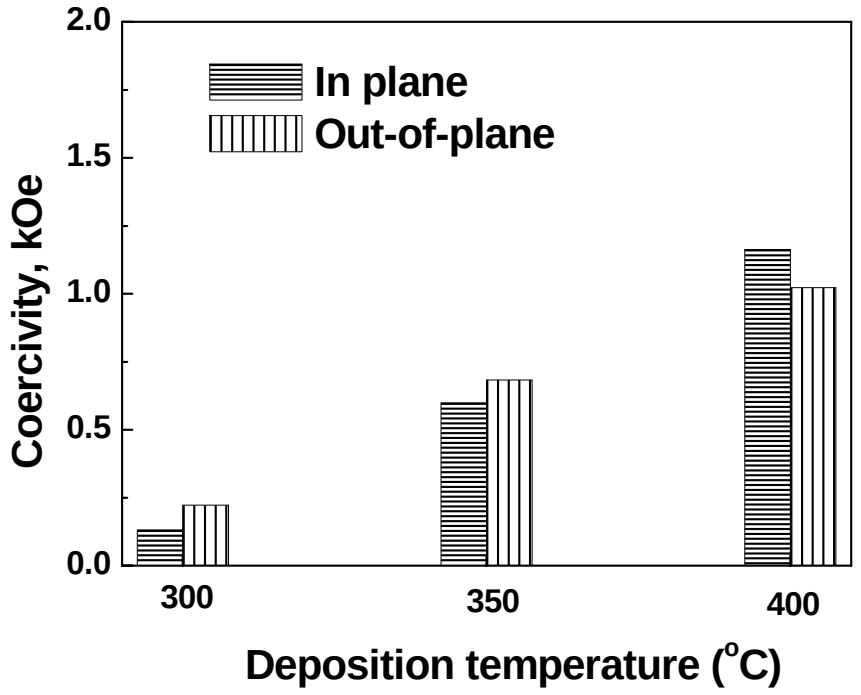

Figure 4-5. Temperature dependence of in-plane and out-of-plane coercivity for 15 nm FePt thin films with deposition temperature variation from 300 to 400 °C; dense bars – in-plane coercivity; sparse bars – out-of-plane coercivity.

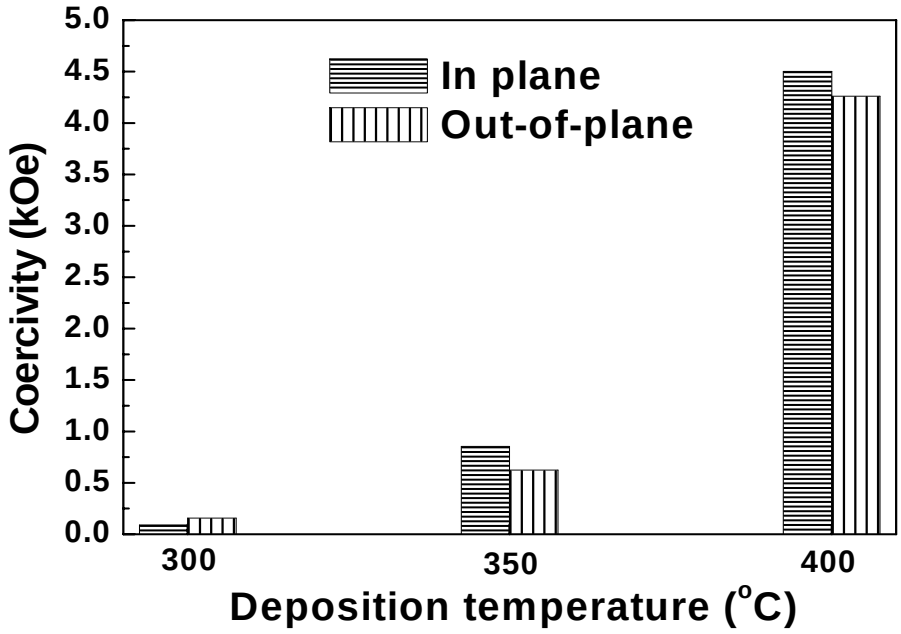

Figure 4-6. Temperature dependence of in-plane and out-of-plane coercivity for 40 nm FePt thin films with deposition temperature variation from 300 to 400 °C; dense bars – in-plane coercivity; sparse bars – out-of-plane coercivity;

indicates that 400 °C is not high enough to form the ordered phase to present a higher coercivity when the film has a thickness of 15 nm. Figure 4-6 shows the temperature dependence of the coercivity for the FePt thin films with a thickness of 40 nm, when the deposition temperature was varied between 300 and 400 °C. For the FePt film deposited at 300 or 350 °C, the coercivity was less than 1 kOe. The low coercivity implies that the disordered *fcc* FePt phase is the dominant phase in the FePt film with a thickness of 40 nm deposited on the glass substrate at temperatures lower than 400°C. When the deposition temperature increased to 400 °C, coercivity increases dramatically to about 4 kOe, indicating the high coercivity *fct* phase as the dominant phase. With respect to the appearance of the characteristic superlattice peaks of the ordered phase, it suggests that the film with a thickness of 40 nm may be easier to form the ordered phase compared to that of the films with a thickness less than 15 nm.

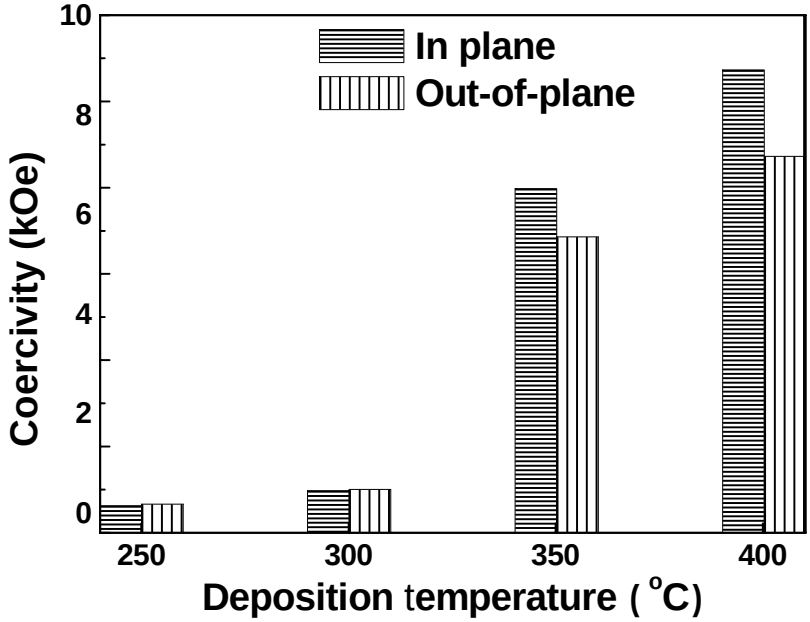

Figure 4-7. Thickness dependence of in-plane and out-of-plane coercivity for 80 nm FePt thin films with deposition temperature variation from 250 to 400 °C**; dense bars – in-plane coercivity; sparse bars – out-of-plane coercivity; coercivity increases dramatically with deposition temperature of 350 °C.**

Figure 4-7 shows the temperature dependence of the coercivity for the FePt thin films with a thickness of 80 nm when the deposition temperature varied between 250 and 400 °C. Coercivity increase dramatically when the deposition temperature increases from 300 to 350 °C. This indicates that the phase transformation temperature decreases for about 50 °C when film thickness increased from 40 to 80 nm.

Deposited at 300 °C, the out-of-plane coercivity for all the three films with the film thickness of 15, 40 and 80 nm is as low as several hundred Oe. The coercivity of FePt thin film with a thickness of 15 nm slightly increases to about 1 kOe with the increase of the deposition temperature to 400 °C, while the coercivity for 40 nm film increases up to about 4 kOe at 400 °C and the coercivity for 80 nm film increases

dramatically to about 6 kOe at 350 ^{o}C. It indicates that with the increase of film thickness, the ordered phase formation temperature decreases. However, as reviewed in the Chapter 1, thick film is not favorable for the application of the FePt film as magnetic recording media. Therefore, FePt films with the thickness of 15 or 40 nm will be used in the following chapters. The promotion of the ordered phase formation will be studied with the additional ultrathin nonmagnetic layers.

4.3 Summary

The crystallographic ordering and magnetic properties of FePt thin films with different thicknesses and deposition temperatures prepared by magnetron sputtering were studied. For films deposited at the same temperature, the coercivity of FePt films increased with film thickness. For films of the same thickness, the coercivity increased with deposition temperature.

In the next chapters, the study is concentrating on FePt films with the thickness of 15 nm and deposition temperature of 400 ^{o}C. The major objective is to lower phase transformation temperature of about 400 ^{o}C and to achieve high coercivity of FePt films.

Chapter 5 Effects of top layer on FePt thin films with glass substrates

As discussed in Chapter 1, the face-centered tetragonal (*fct*) $L1_0$ FePt with alternating planes of Fe and Pt atoms stacked along the (001) direction possesses high magnetocrystalline anisotropy and high magnetization.[82-84] As the reduction of bit size is limited by the superparamagnetism, a large magnetic anisotropy allows a further reduction of the recording bit size. To study the FePt alloy as magnetic recording media, it is important to achieve high ordered $L1_0$ phase in FePt films at a relatively low temperature. Therefore, the major task of my PhD project was focused on how to reduce the phase transformation temperature from the disordered *fcc* to the ordered *fct* $L1_0$ using additive layers (mainly Ag layers). The first work I did was the investigation of the structure and magnetic properties when a thin Ag layer was deposited on the top of the FePt thin film. In this work, a coercivity up to 6 kOe has been achieved after deposition at 400 ^{o}C with Ag top layers.

5.1 Experiment methodology

FePt thin films were deposited at the same condition as that described in Chapter 4. Two series of FePt films with nominal total thickness of 15 and 40 nm, respectively, were prepared. An Ag layer with a nominal thickness of 0, 0.25, 1, or 4 nm was deposited at the same temperature of 400 °C directly after the deposition of the FePt layer. The structure of the films are shown in Figure 5-1 and the coercivity values of FePt films are listed in Table 5-I.

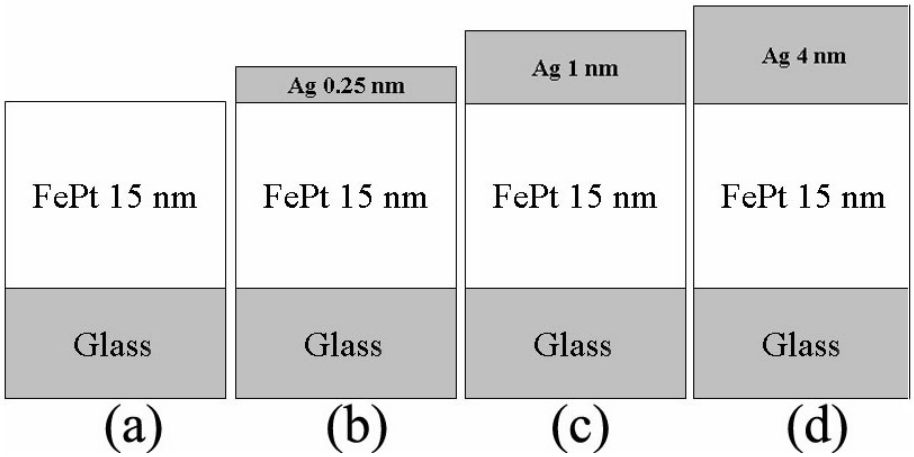

Figure 5-1. Schematic representation of FePt films with Structures Ag top layer of 0, 0.25, 1, and 4 nm.

Table 5-I. Layer structure and magnetic properties of FePt films with different thickness of Ag top layers; $Hc_{//}$ – in-plane coercivity; $Hc_{\perp}$ – out-of-plane coercivity.

Sample	Film structures	$Hc_{//}$ (Oe)	$Hc_{\perp}$ (Oe)
A	Glass/FePt 15 nm	1098	1045
B	Glass/FePt 15 nm/Ag 0.25 nm	2751	3288
C	Glass/FePt 15 nm/Ag 1 nm	4685	5980
D	Glass/FePt 15 nm/Ag 4 nm	5107	6398

Arc melting method is used to fabrication FePt, FePt-5 at%Cu, and FePt-5 at% Ag bulk alloy at 1400 °C. In order to obtain uniform alloy, the ingots were repeatedly molten for 5 times and homogenized at 1000 °C under vacuum for 48 hours.

Crystallographic structure of the films was studied using a grazing-incidence X-ray diffraction (GIXD) diffractometer (Rigaku, ATX-G) with Cu K_{α} radiation at an

grazing incident angle of 0.5 °.[114] X-ray reflectivity (XRR) is performed to obtain the surface roughness, thickness, and density of the FePt films. Magnetic properties of the films were measured with a vibrating sample magnetometer (VSM) under a maximum applied field of 15 kOe. The HRTEM studies were carried out using a JEOL 3010 microscope with an operating voltage of 300 kV and a lattice resolution of 1.4 Å. The X-ray photoelectron spectra (XPS) of these thin films were recorded on a Scientific Instruments spectrometer by a K_α source operating at 100 W. All the X-ray photoelectron spectra were obtained with pass energy of 90 eV for wide scans and 44 eV for individual elements. The quantitative evaluation of each peak was obtained by dividing the integrated peak area by atomic sensitivity factors that were calculated from the ionization cross-sections, the mean free electron escape depth, and the measured transmission functions of the spectrometer.

5.2 Results and discussion

5.2.1 M-H curves

Figure 5-2 shows the magnetization curves of the FePt thin films with different thicknesses of Ag top layers. The in-plane and out-of-plane coercivities are listed in Table 5-I. For the FePt film without the Ag top layer (Sample A), the hysteresis curves show coercivities of about 1.0 kOe in both directions. The low coercivities indicate that the disordered *fcc* FePt phase was the dominant phase, when FePt was deposited directly on the glass substrate at the substrate temperature of 400 °C. The film is easier

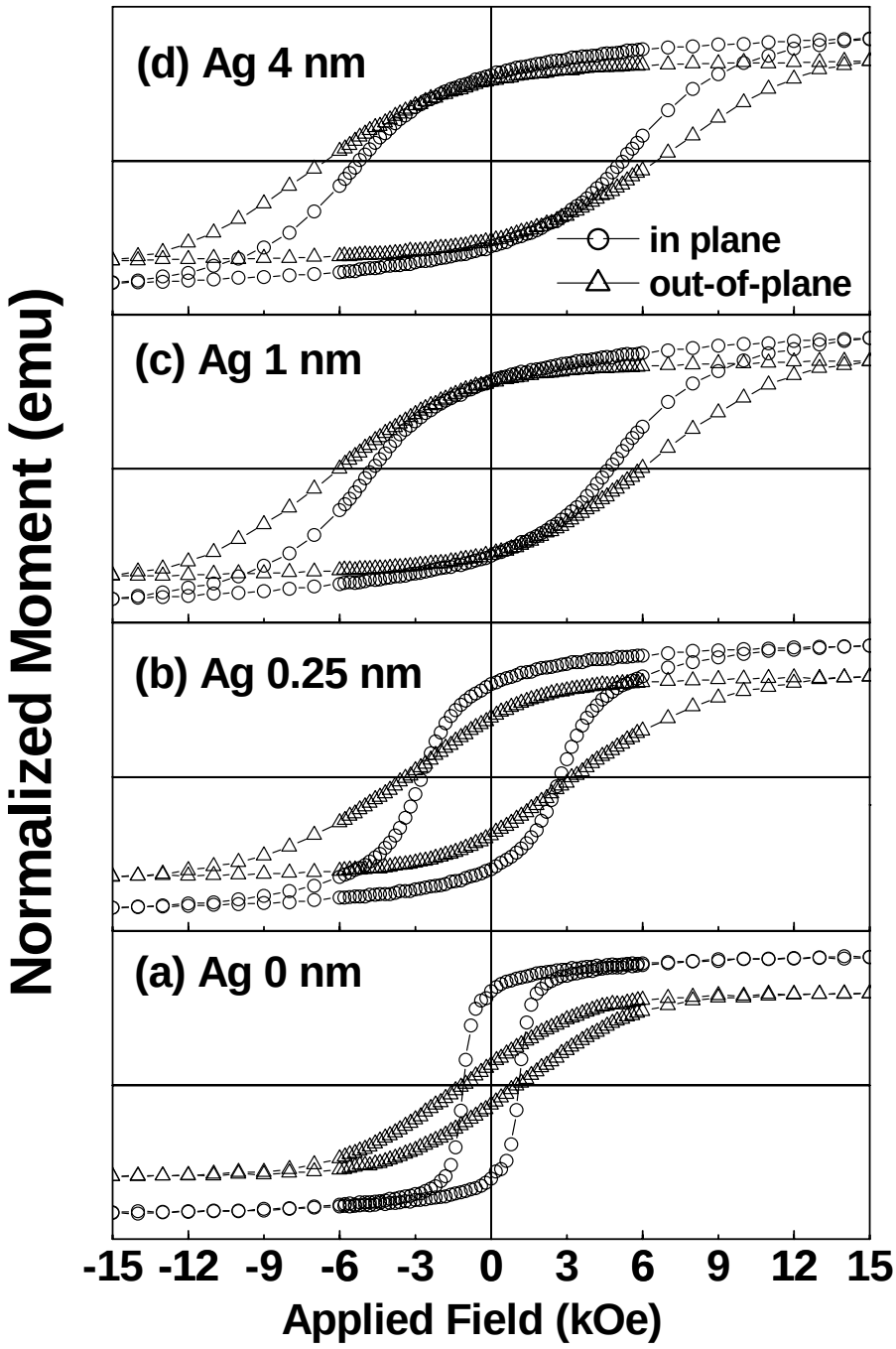

Figure 5-2. Magnetic hysteresis curves for the FePt thin films (a) without Ag top layer; with a thickness of (b) 0.25 nm, (c) 1 nm, and (d) 4 nm Ag top layers under a maximum applied field of 15 kOe; circle – in-plane hysteresis curve; triangle – out-of-plane hysteresis curve.

to be saturated in the parallel direction of the film than in the film normal direction. It suggests that the easy axis is in the film plane and hard axis is normal to the film.

Both the in-plane and out-of-plane coercivities dramatically increased when an ultrathin Ag top layer was deposited on the top of the FePt film. The in-plane and out-of-plane coercivity increased to about 3 kOe for the Sample B film with Ag top layer of 0.25 nm. It indicates that the Ag top layer is effective to enhance the coercivity of the film. When the thickness of the Ag top layer further increased to 1 nm, the out-of-plane coercivity (Sample C) dramatically increased to about 6 kOe, which is slightly larger than that of the in-plane coercivity. The increase of the coercivities suggests that the ordering of the FePt film is promoted by the presence of the Ag top layers. However, with a further increase the thickness of the Ag top layer to 4 nm (Sample D), the coercivity for the Sample D is about 6.4 kOe, which is slightly larger than that of Sample C. The results indicate that the thicker Ag top layer would not result in a further significant change in coercivity.

5.2.2 XRD analysis

Figure 5-3a shows the in-plane XRD scans of FePt thin films with different thicknesses of the Ag top layer. As the same result as in Chapter 4, the FePt film without the Ag top layer mainly shows the fundamental peaks of (111), (200) and (022) of the *fcc* FePt phase and only a weak superlattice peak (110) of the $L1_0$ FePt phase in the spectrum, indicating that the deposition temperature of 400°C was not high enough to achieve a highly ordered FePt alloy with $L1_0$ as the major phase. After the deposition of 0.25 nm of Ag on the top of the FePt thin film (Sample B), the

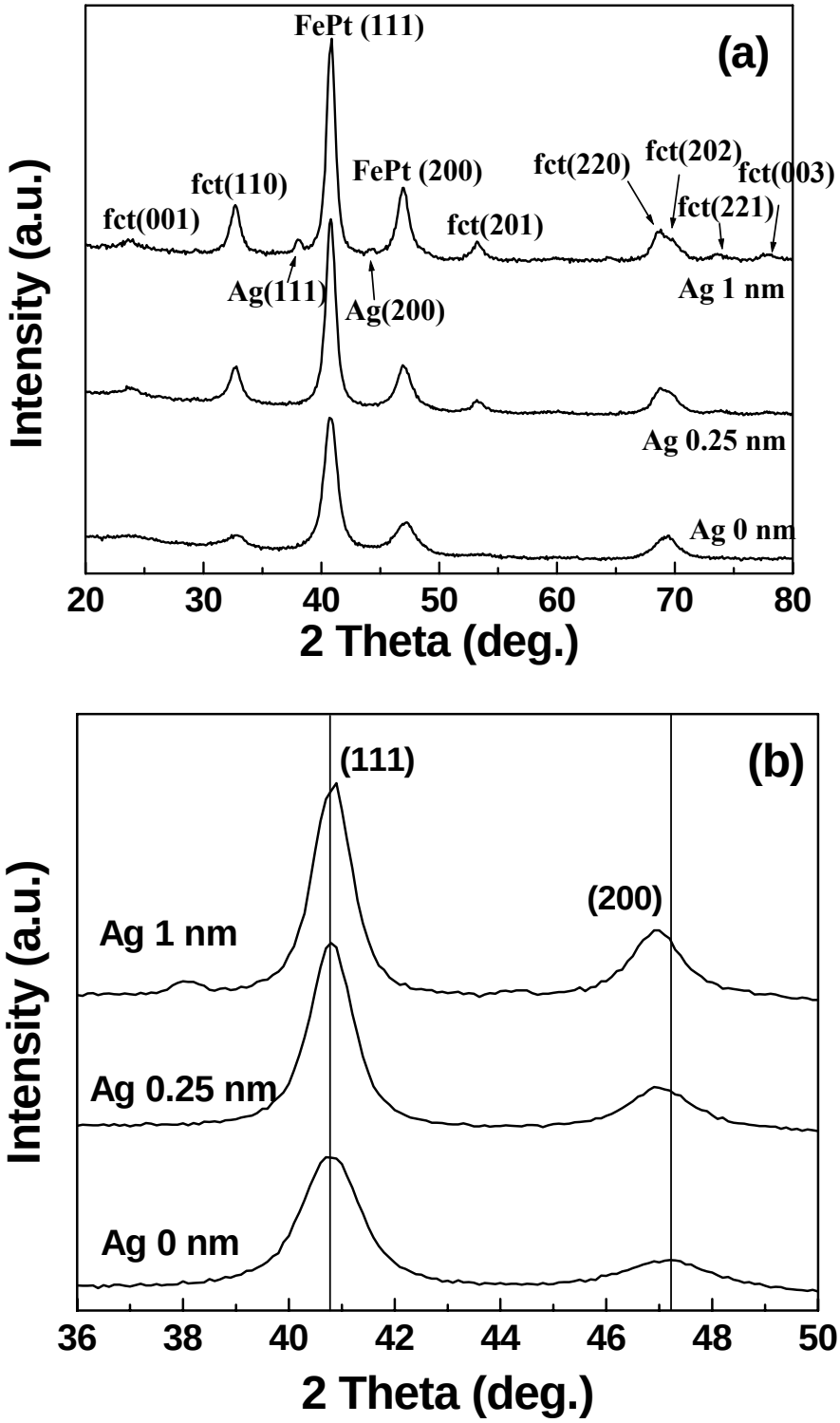

Figure 5-3. (a) In-plane crystallographic XRD patterns of FePt thin films with Ag top layers of different thicknesses. (b) Enlarged view of the XRD scans with 2θ range from 36-50 degree in (a).

superlattice peaks became stronger and the *fct* (201) peak appeared. With 1 nm top Ag layer deposited (Sample C), the intensity of the superlattice peaks increased further and the weak *fct* (221) and *fct* (003) peaks appeared in the spectrum. Figure 5-3b shows an enlarged view of the XRD scans with 2θ range in the range of 36 to 50 degree. The position of the FePt (111) peak shifted to the higher angle and the position of the FePt (200) shifted to the lower angle when the Ag top layer was deposited on the FePt film. These results indicate that the Ag top layer promotes the ordering of the $L1_0$ FePt phase. It is possible that Ag atoms induce vacancies to increase the mobility of the Fe and Pt atoms and thus enhance the kinetics for the phase transformation.[115-116] It is noted that the absolute intensity of the fundamental FePt (111) and (200) peaks increases after the deposition of the Ag top layer (seen in Fig. 5-3a). This may indicate that the crystallization of the FePt film with Ag top layer increases with respect to that of film without Ag top layer. Using Bragg's law, the lattice constants *a* and *c* in Sample C were calculated to be 3.871 and 3.737 Å from the peaks of $L1_0$ (110) and (001), respectively. The *c/a* ratio was 96.5% that is comparable to the value of bulk ordered FePt. [116]

5.2.3 X-ray reflectivity (XRR)

When X-rays are applied to a material's surface, total reflection will occur at or below a certain incident angle, θ_c. Figure 5-4a shows the schematic illustration of method of X-ray reflectivity (XRR). The higher the incident X-ray angle relative to the critical angle, the deeper the X-rays transmit into the material. With a material whose surface is ideally flat, the reflectivity suddenly decreases at angles above the

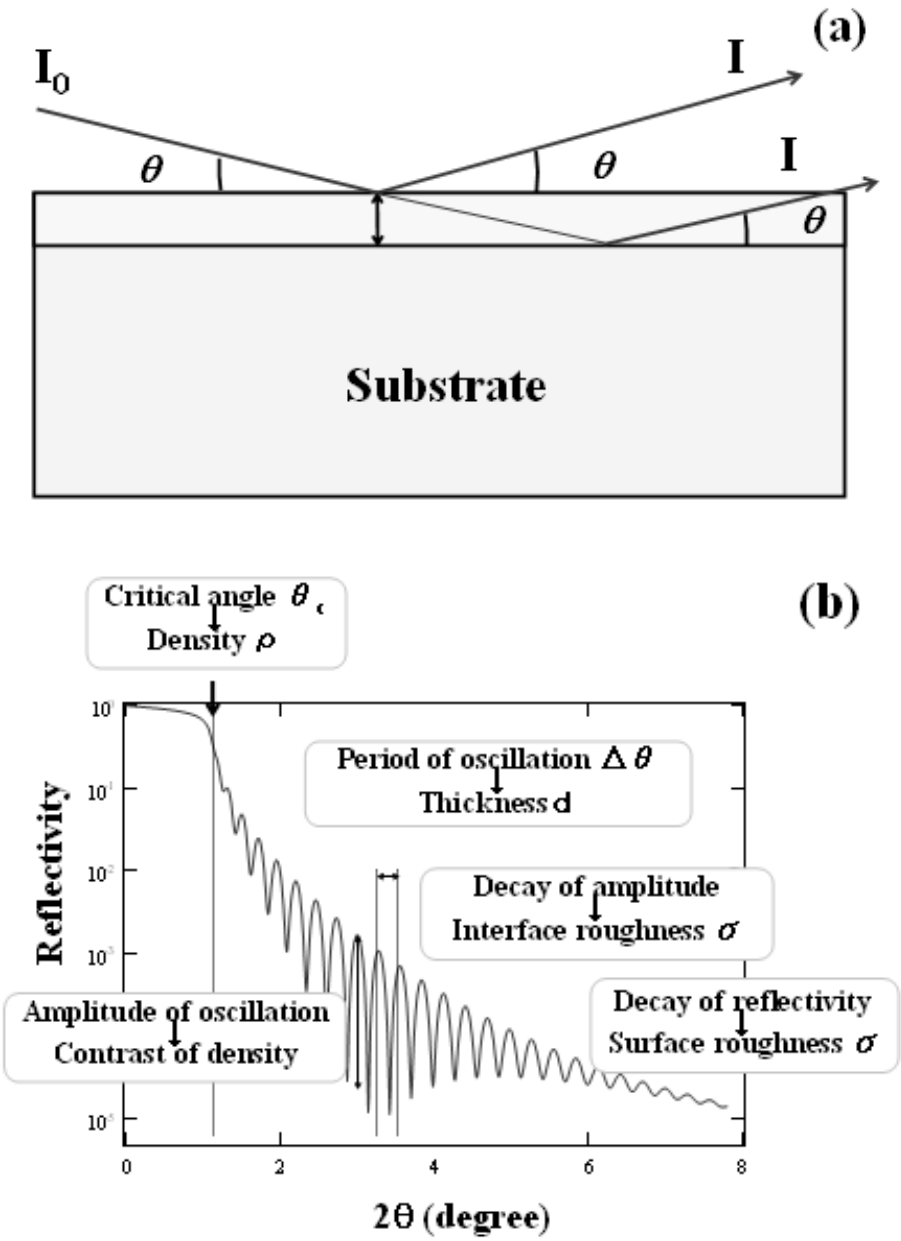

Figure 5-4. (a) Schematic illustration of X-ray reflectivity; (b) the profile of the XRR; the parameters that can be derived from the spectra are noted in the figure. θ is the angle of the incidence and of the diffraction of the radiation relative to the reflecting plane; I_0 is the intensity of the incident beam; I is the intensity of the reflectivity beam.

critical angle in proportion to θ^{-4}. If the material surface is rough, it causes a drastic decrease in reflectivity. If such a material, serving as a substrate, is evenly overlaid with another material having a different electronic density, then reflected X-rays from

the interface between the substrate and the thin film as well as from the free surface of the thin film will either constructively or destructively interfere with each other - resulting in an interference induced oscillation pattern. Figure 5-4b shows the typical spectrum of X-ray reflectivity (XRR). To a first approximation, the intensity scattered by a sample is proportional to the square of modulus of the Fourier transform of the electron density. Thus the electron density profile can be deduced from the measured intensity pattern, and subsequently the vertical properties (layer thicknesses) as well as the lateral properties (roughness and correlation properties of interfaces or lateral layer structure) characterizing multilayer can be determined. Specifically, film thickness can be determined from the periodicity of the oscillation and information on the surface and interface from the angular dependency of the oscillation pattern's amplitude.

X-ray reflectivity was measured to examine the surface roughness of FePt thin films with Ag top layers of different thicknesses. Figure 5-5 shows the X-ray reflectivity scans of the FePt films. The profile for Sample A shows a oscillation period till $2\theta > 6^{o}$, while the profile for Sample B shows a decrease of the amplitude of the oscillation in the range of $2\theta = 0\text{-}5^{o}$ and the profile for Sample C presents diminish of the oscillation from 3^{o}. Calculated from the degradation of the amplitude of the oscillation fringes, the surface roughness of Sample B is about 0.45 nm and it increases to 0.9 nm when the Ag top layer of 1 nm was deposited (Sample C), indicating a rougher surface that the top Ag layer might not form a continuous layer

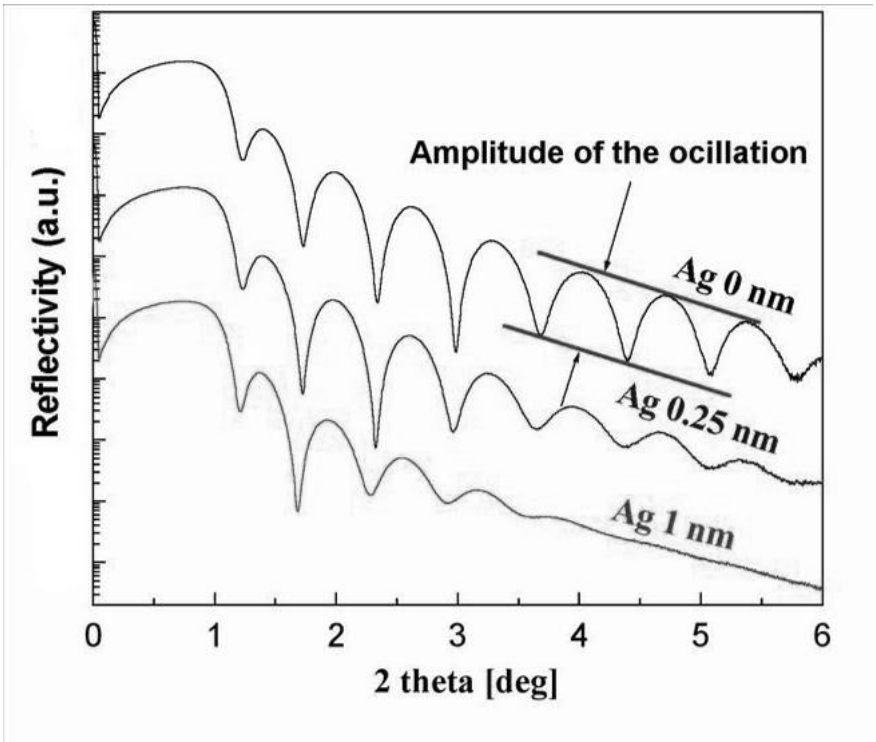

Figure 5-5. The X-Ray reflectivity patterns for FePt thin films without Ag top layer and with 0.25 nm and 1 nm Ag top layers; the larger amplitude of the oscillation of the curves indicates the smoother of the film surface.

on the surface. Some of the Ag atoms may remain on the top of the FePt surface, while some of the Ag diffused into the FePt layer.

5.2.4 TEM microstructures

Figure 5-6 shows the TEM images and selected area electron diffraction (SAED) patterns of Sample A without an Ag top layer and Sample C with an Ag top layer of 1 nm. Compared to the grain size of FePt film without Ag top layer (Sample A), the grain size slightly increased with the deposition of Ag top layer of 1 nm (Sample C). The film without the Ag top layer was mainly composed of randomly oriented FePt grains and amorphous FePt. The SAED pattern shows the fundamental diffraction rings only, which suggests that the disordered *fcc* phase is present in the

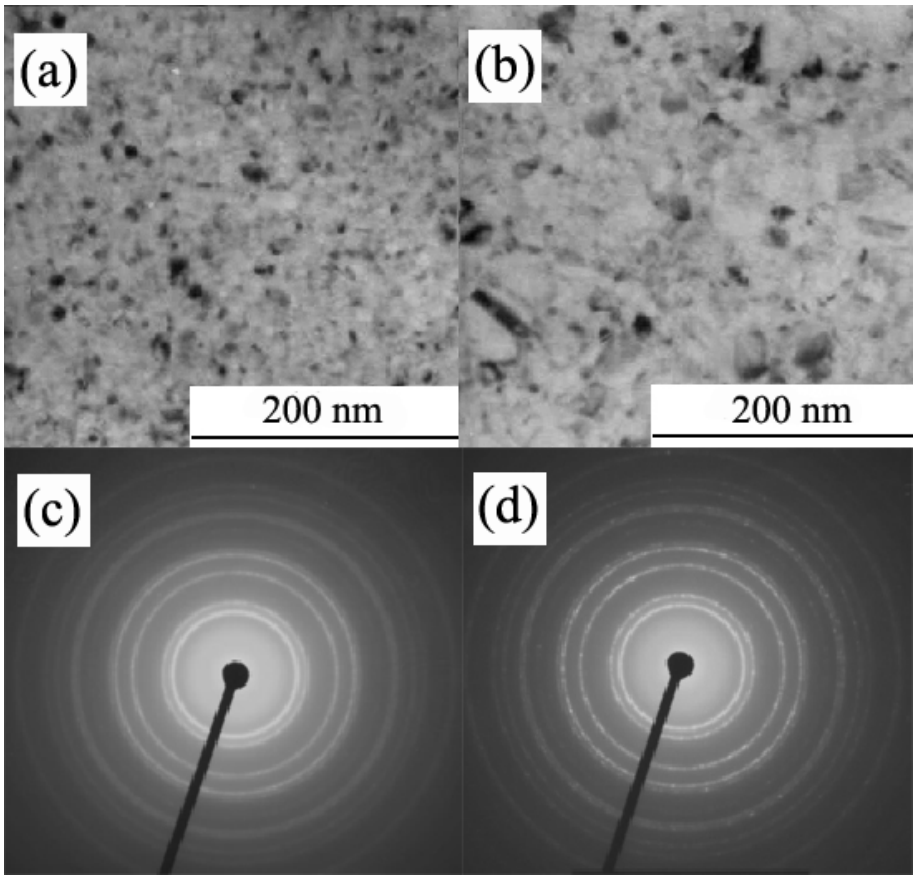

Figure 5-6. TEM images and SAED patterns of the FePt films without Ag top layer (a) and (c) and with 1 nm Ag top layer (b) and (d); scale bar in Fig. a and b is 200 nm.

film. With the deposition of the Ag top layer, larger FePt grains are found in the TEM image. The diffraction rings in the SAED pattern becomes intense and superlattice spots appear in the pattern, indicating that the ordered *fct* phase is dominant when the Ag top layer is deposited. The results are well agreed with the XRD profiles in Fig. 5-3a.

5.2.5 HRTEM microstructures

Figure 5-7 shows the HRTEM images of the Sample A without an Ag top layer and Sample C with an Ag top layer of 1 nm. Large area of amorphous FePt was

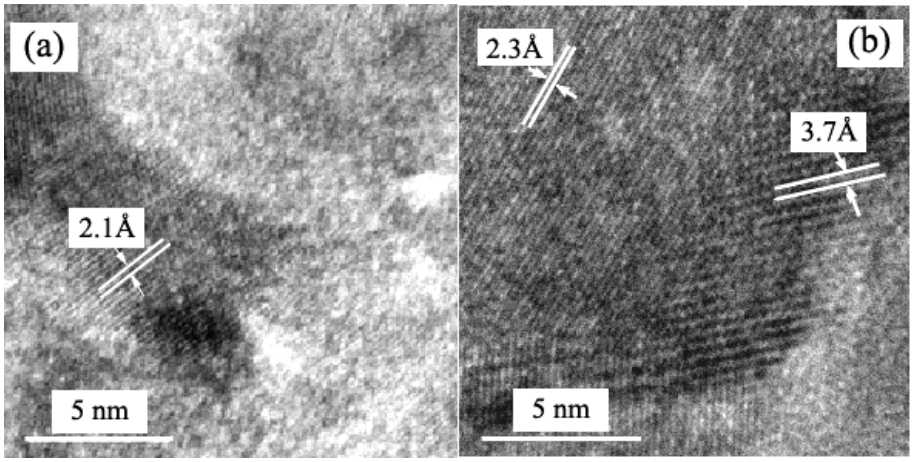

Figure 5-7. HRTEM images of the FePt film without the Ag top layer (a) and with 1 nm Ag top layer (b). The lattice planes with a *d*-spacing of 2.1 Å are the fundamental (111) planes of FePt; 2.3 Å is Ag (111); the lattice planes with a *d*-spacing of 3.7 Å are the superlattice $L1_0$ FePt (001) planes.

observed surrounding the FePt grains (with d-spacing of 2.1 Å) in the FePt film without the Ag top layer, as seen in Fig. 5-7 (a). This result indicates the low crystallinity of the FePt film without an Ag top layer. As shown in Fig. 5-7(b), particles are present with the lattice spacing of 2.3 Å which corresponds to the (111) plane of *fcc* Ag. The result clearly indicates that Ag atoms diffuse into the FePt layer, do not form solid solution with FePt and form Ag particles inside of the FePt layer. A more close observation revealed that many small Ag particles are present in the grain boundary regions between FePt grains. With a lattice mismatch of 5.5%, the Ag (111) may serve as a nucleation plane for the growth of the (001) plane of the $L1_0$ ordered FePt phase. In the HRTEM image, the superlattice (001) planes present in the $L1_0$ ordered FePt particle. The existence of the Ag that diffused from top of the film promoted the $L1_0$ ordered FePt phase transformation and reduced exchange coupling by separating the FePt particles.

5.2.6 Interaction behaviors in FePt thin films

The technique of remanence curve is introduced in the methodology section of Chapter 3. This technique was used to characterize the magnetization reversal mechanism of thin film materials. The δM curves for all the FePt thin films (15 nm and 40) with different Ag top layers were measured. Figure 5-8 shows the variation of δM for different samples with an FePt thickness of 15 nm (Samples A-C) when the external field was applied in the film plane. For Sample B (with an Ag top layer of 0.25 nm), δM was positive at small magnetic fields. However, the intensity of the positive δM was much lower compared to Sample A. This result indicates that intergranular exchange coupling was strongly reduced by the deposition of an Ag top layer of 0.25 nm. For Sample C with an Ag top layer of 1 nm, positive δM at lower

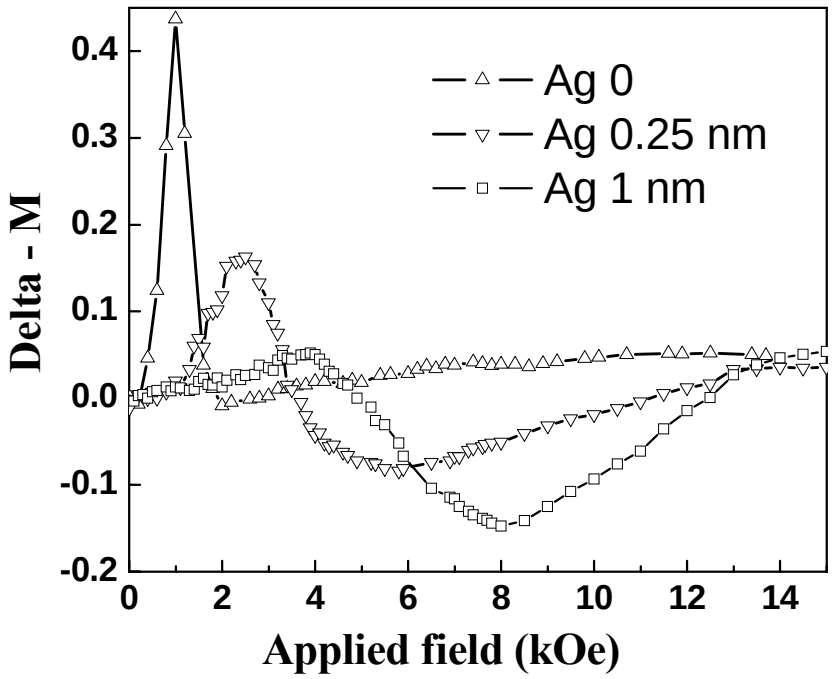

Figure 5-8. Variation of δM as a function of the Ag top layer thickness with the external field applied in the film plane direction; upper triangle – FePt film without Ag top layer; down triangle – FePt film with 0.25 nm Ag top layer; square – FePt film with 1 nm Ag top layer.

magnetic fields was very small, while there was a large negative δM at higher magnetic fields. Thus, the dramatic increase in coercivity with an ultrathin Ag top layer was caused not only by promotion of disorder/order phase transformation, but also by the modification of the microstructure, which reduce the intergranular exchange coupling. As discussed previously (HRTEM), Ag particles were found in the grain boundary areas between FePt grains. The strong reduction of exchange coupling is probably due to the presence of non-magnetic particles (here Ag) in the grain boundaries of magnetic FePt grains.

5.2.7 Effect of Ag top layer on FePt film with different thickness and different deposition temperature

As discussed above, both the in-plane and out-of-plane coercivities increased with the thickness increase of the Ag top layer deposited on the FePt thin. To carry out a more detailed research study, FePt films with thickness of 40 nm are used in this section. The effect of top layer to the magnetic properties of FePt films will be investigated with variation of deposition temperatures of the FePt layer and Ag top layers as well.

The layer structures and coercivity values for the FePt films with or without an Ag top layer are listed in Table 5-II. Sample E and Sample F are FePt films without Ag top layer that deposited at 350 and 400 ^{o}C, respectively. These samples have been used in Chapter 4 for the discussion of the influence of the deposition temperature on the magnetic properties of FePt films. The coercivities of Sample F are about 4 kOe, which is much higher than those of Sample E. It was concluded in Chapter 4 that

Table 5-II. Layer structure and magnetic properties of FePt films with different thickness of Ag top layers and different deposition conditions; $Hc_{//}$ – in-plane coercivity; $Hc_{\perp}$ – out-of-plane coercivity.

	Film structures	$Hc_{//}$ (Oe)	$Hc_{\perp}$ (Oe)
E	**Glass/FePt 40 nm, 350 ^{o}C**	**853**	**625**
F	**Glass/ FePt 40 nm, 400 ^{o}C**	**4504**	**4261**
G	**Glass/FePt 40 nm, 350 ^{o}C /Ag 4 nm, 350 ^{o}C**	**3038**	**2967**
H	**Glass/FePt 40 nm, 400 ^{o}C /Ag 4 nm, 400 ^{o}C**	**7409**	**6777**
I	**Glass/FePt 40 nm, 350 ^{o}C, /Ag 4 nm, RT**	**936**	**875**

the ordering temperature for FePt film with a thickness of 40 nm is reduced to around 400 ^{o}C. With the deposition of Ag top layer of 4 nm on Sample E and F at the same deposition temperature of Sample E and F, we obtained Sample G and Sample H, respectively. The coercivity is about 3 kOe for Sample G and is over 6 kOe for Sample H. Both the coercivity values are much higher than of Sample E and F. The result indicates that the Ag top layers are effective to enhance the coercivity of FePt film.

Figure 5-9 (a) shows the XRD scans of the FePt thin films with different structures. Except the amorphous hump from the glass substrate, only a fundamental FePt (111) peak showed up in the scan of Sample E with deposition temperature of 350 ^{o}C. As concluded in Chapter 4, the disordered *fcc* phase dominates in the film with deposition temperature of 350 ^{o}C. The low coercivity of Sample E shown in the Table 5-III is well agreed with the XRD analysis in Fig. 5-9. When the deposition temperature increased to 400 ^{o}C (Sample F), the superlattice (001) peak shows up on the top of the amorphous hump of the glass substrate and another superlattice peak

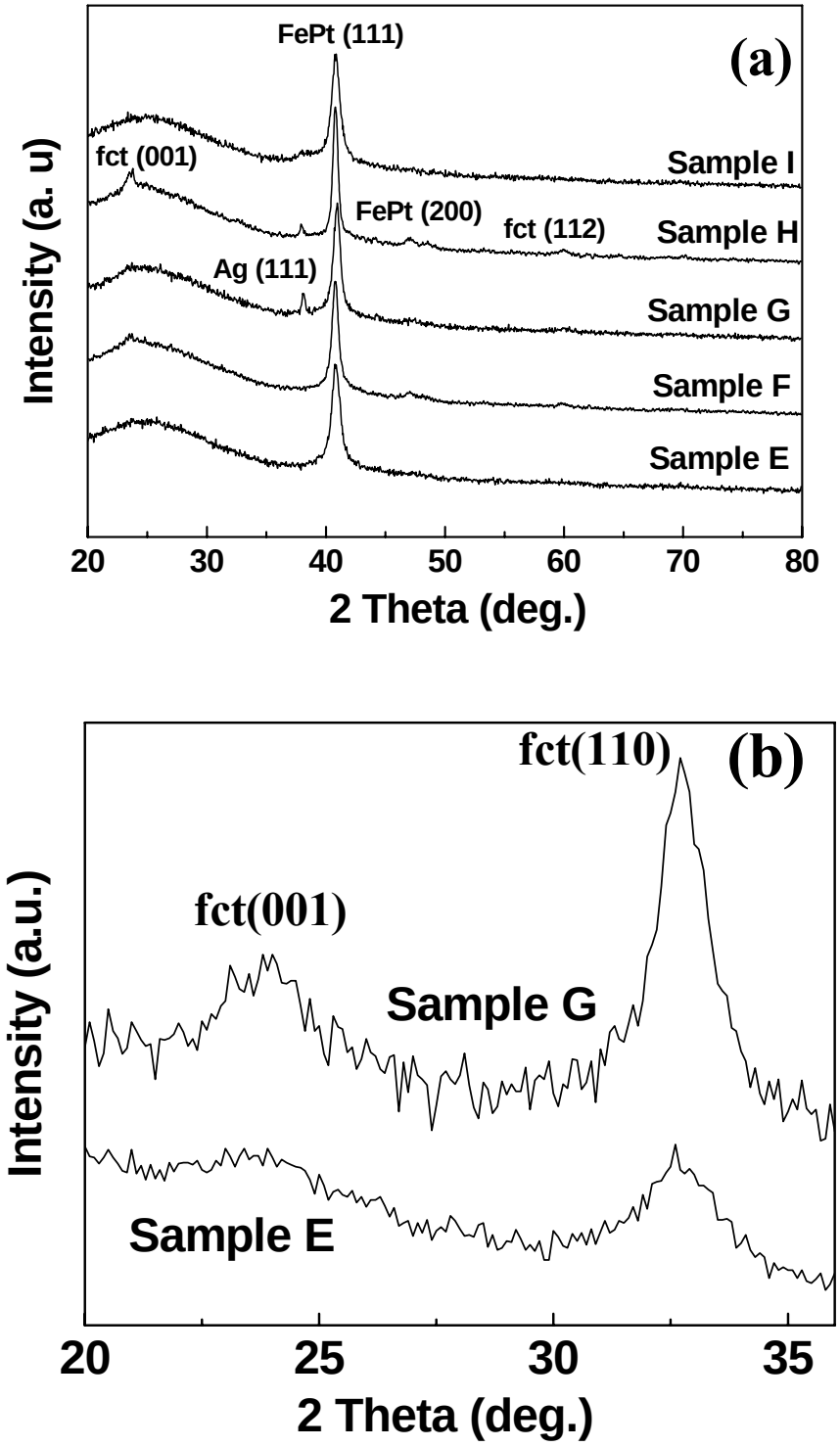

Figure 5-9. (a) XRD scans of FePt thin films with different sample structures. (b) the enlarged view of in-plane XRD scans of Sample G and Sample E at the 2θ range of 20-36 degree. The intensity of the fct (001) peak increase when Ag top layer was deposited.

such as (112) peak appears. The in-plane and out-of-plane coercivities both increase to over 4 kOe. It indicates that the ordered $L1_0$ phase is formed in Sample F and the ordering temperature should be between 350 and 400 ^oC. With the Ag top layer deposited, weak superlattice peaks are observed in the XRD pattern of Sample G. Additionally, both the in-plane and out-of-plane coercivities increase to about 3 kOe. For Sample H, when an Ag layer of 4 nm was deposited on FePt layer at the deposition temperature of 400 ^oC, the intensity of the superlattice peaks further increased and the coercivity increased to about 7 kOe. It indicates that the Ag top layer is also effective at higher temperature when FePt was already partially ordered.

Figure 5-9 (b) shows the enlarged view of the in-plane XRD scans of Sample E and G at the 2θ range of 20-36 degree. The intensity of the superlattice peaks (001) and (110) of Sample G was obviously larger than that of Sample E. It implies that the ordering temperature of $L1_0$ ordered FePt phase was reduced to 350 ^oC with the deposition of the Ag top layer.

5.2.8 Effect of the deposition temperature of Ag top layer

To investigate the influence of the deposition temperature of Ag top layer on magnetic properties, Sample I with Ag top layer deposited at room temperature was fabricated. Comparing with the large increase of the coercivity in Sample G, the coercivity of Sample I was nearly the same as that of Sample E, as shown in Table 5-III. This result is in agreement with the XRD analysis of the samples, where the FePt diffraction peaks of Sample I were almost the same as those of Sample E. It indicates that the Ag top layer that deposited at room temperature is not effective to

Table 5-III. 2θ values in degree for the three FePt samples with different alloying elements; XRD is performed at the core parts of each samples.

	FePt (111)	FePt (200)	FePt (220)	FePt (311)
FePt	**40.9**	**47.1**	**68.9**	**83.3**
FePt-5Ag	**40.9**	**47.1**	**68.9**	**83.1**
FePt-5Cu	**40.3**	**46.9**	**68.6**	**82.8**

enhance the coercivity and to promote the disorder/order phase transformation.

X-ray photoelectron spectrometer (XPS) was performed on the FePt film with an Ag top layer deposited at 350 ^{o}C (Sample G) and room temperature (Sample I). Figure 5-10 shows the Pt-4f and Ag-3d XPS spectra of the Sample G and Sample I. In the binding energy range of Pt-4f spectra, the intensity of Sample G was much stronger than that of Sample I, indicating that the Pt composition was much higher on the surface of Sample G. Since the film structure is the same for the two samples, the difference of the surface composition should be caused by the different diffusion rate of Ag into FePt layer at different deposition temperature.

In the binding energy range of Ag-3d spectra, on the contrary, the intensity of Sample I was much lower than that of Sample G, suggesting that the Ag composition of Sample I was much lower on the surface. It is reasonable to conclude that Ag may be diffused into the FePt layer when the deposition temperature of the Ag top layer is high enough. On the other hand, most of the Ag may be remained on the surface of the sample when Ag top layer was deposited at room temperature. Correlated with the

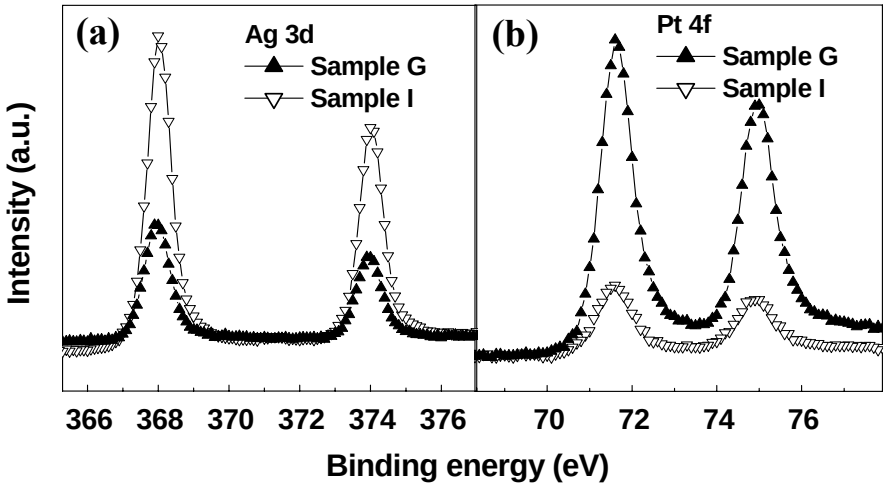

Figure 5-10. The Pt-4f (a) and Ag-3d (b) X-ray photoelectron spectra of the samples with Ag top layer deposited at high temperature (Sample G) and room temperature (Sample I); solid upper triangle –XPS spectrum for Sample I; blank down triangle – XPS spectrum for Sample G.

analyses of the XRR and SEM, the deposited Ag may diffuse into FePt layer when deposited at higher temperatures. The diffusion of the Ag may increase the mobility of the atoms, resulting in a further re-crystallization of the film. As a result, the $L1_0$ ordered FePt phase transformation was improved by the existence of the Ag in the FePt film. The volume expansion caused by the diffused Ag could supply large elastic energy to the FePt grains, facilitating transformation.

5.2.9 Alloys by arc melting -- a study of solubility of Ag in FePt alloy

Ag has been deposited as additive elements in FePt layers to promote the ordering of FePt film and Ag was reported to be immiscible with FePt.[68,116,23] However, there is no systematic work to confirm the miscibility of Ag and FePt. In this section, FePt alloying with additive of 5 at% of Ag (FePt-5Ag) was fabricated by arc melting to investigate the miscibility of Ag and FePt. Meanwhile, Cu has been

intensively studied as an additive element to improve the ordering of FePt and Cu was reported to form solid solution with FePt.[64-68] As a comparison, FePt ingots with 5 at% of Cu (FePt-5Cu) and 100% FePt were fabricated with the same method and under the same condition as well.

Figure 5-11 shows the XRD patterns for FePt, FePt-5Ag, and FePt-5Cu ingots that obtained by arc melting. In all the three patterns, the largest intensity of the diffraction peaks is FePt (111). With 5 at% of Ag alloyed in FePt, besides the diffraction peaks of FePt, diffraction peaks from Ag are presented in the XRD profile. The present of Ag peak indicates that Ag is immiscible with FePt and was separated from FePt with cooling down from the molten state. On the contrary, the 2θ position

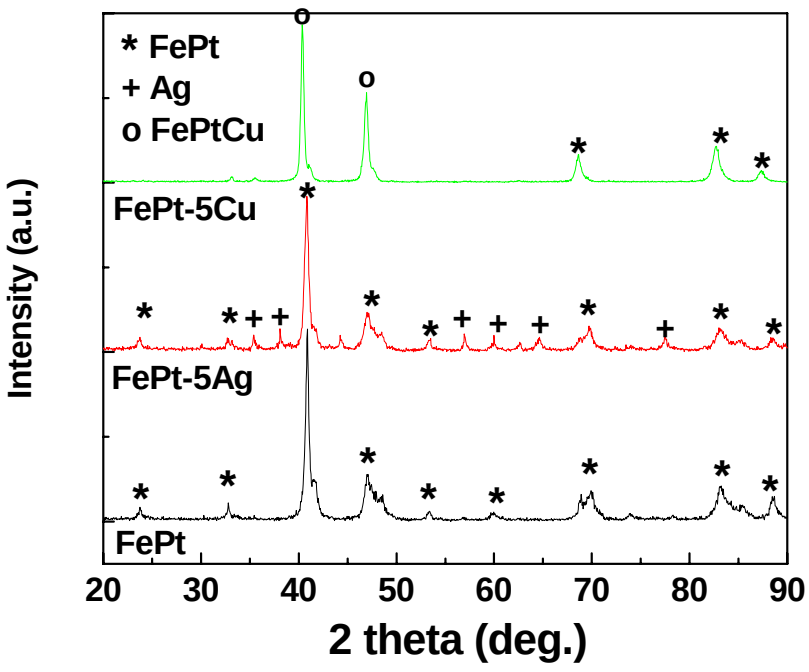

Figure 5-11. XRD scans for FePt, FePt-Ag, and FePt-Cu ingots obtained from arc melting. In the XRD scan of FePt-5Ag, diffraction peaks of Ag are presented; while for FePt-5Cu alloy, diffraction peaks of FePtCu solid solution are presented in the scan.

of the peak of FePt (111) shifts to a lower angle when Cu is alloyed into FePt alloy and no additional peaks are observed from Cu element. It suggests that the FePt-5Cu may form an FePtCu solid solution. The shifted diffraction peak of FePt (111) is regarded as the (111) peak of FePtCu solid solution. Table 5-III summarizes the 2θ values for the diffraction peaks of the XRD patterns of FePt, FePt-5Ag, and FePt-5Cu ingots. The 2θ values for the FePt-Ag ingot is almost the same as those of the FePt alloy. On the contrary, all the 2θ values of the diffraction peaks for the FePt-Cu ingot is shifted to lower angles compared to those of the FePt alloy. Therefore, the XRD analysis suggests that Cu formed solid solution with FePt, while Ag could not form solid solution phase with FePt.

5.3 Summary

The deposition of an Ag top layer on FePt film promotes the phase formation of the $L1_0$ ordered FePt and enhances the coercivity of FePt films both in the in-plane and out-of-plane directions.

Based on the XRR and XPS analysis, the Ag that deposited on the top of the film diffuses into the FePt layer. The volume expansion caused by the diffused Ag could supply large elastic energy to the FePt grains, resulting in the promotion of the phase ordering in the FePt film.

Ag is immiscible with FePt and the diffused Ag may stay in the grain boundaries to reduce the exchange coupling between FePt grains. Correlating with the promotion of ordering transformation of FePt by Ag diffusion, the reduction of the exchange coupling further enhances the coercivity of the FePt films.

Chapter 6 Comparison of underlayer, intermediate, and top layers

As discussed in Chapter 5, the nonmagnetic top layer enhances the coercivity of FePt films by promoting the disordered/ordered transformation of FePt thin films and by enhancing the crystallinity of the film. However, grain growth is observed and the surface roughness increased in the FePt films with deposition of Ag top layers. Additionally, the deposition of a top layer inevitably increases the flying height between the magnetic head and recording media, making FePt thin films unsuitable for magnetic recording because of surface smoothness. Based on this consideration, we deposited additional layers as underlayer, intermediate layer, and top layer to compare the influence of these layers to FePt thin films.

6.1 Experiment methodology

The layer structures of the FePt films with different additive layers are shown in Figure 6-1 and the coercivity values of the FePt films with different structures are listed in Table 6-I. FePt thin films with a nominal thickness of 15 nm were deposited by *DC* magnetron sputtering on glass substrates at 400 ^{o}C. The Ag layers with a nominal thickness of 0.25 nm were deposited at the same temperature before deposition of FePt layer as an underlayer, between two FePt layers as an intermediate layer, and on the top of FePt layer as a top layer. As discussed in the last chapter, these Ag layers with an expected thickness of 0.25 nm were not continuous layers, but are referred to as layers in the thesis for convenient interpretation. The layer thickness is defined as the nominal

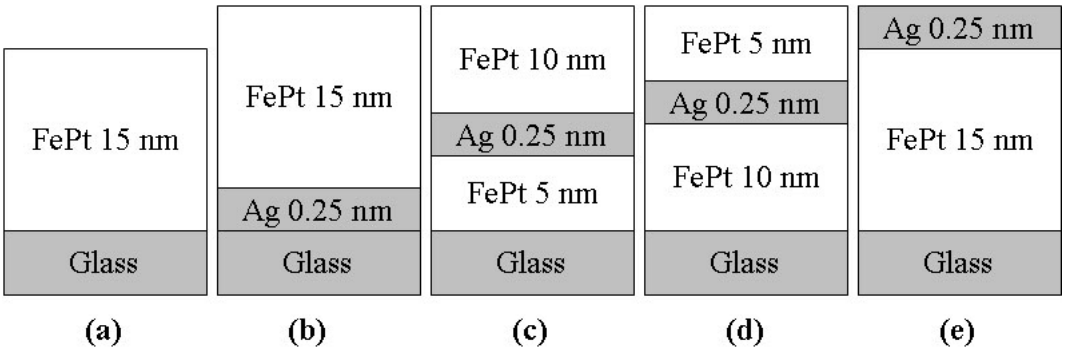

Figure 6-1. Schematic representation of FePt films with Ag underlayer, intermediate layers and top layer.

thickness as the layer was assumed to be a continuous layer. Magnetic properties of the films were measured with a vibrating sample magnetometer (VSM) under a maximum applied field of 15 kOe. Crystallographic texture of the films was studied by in-plane XRD using a Grazing-incidence X-ray diffraction (GIXD) diffractometer (Rigaku, ATX-G) at an incident angle of 0.5 ^{o}.

6.2 Results and discussion

6.2.1 Crystallographic properties

Figure 6-2 shows the in-plane XRD scans of FePt thin films with different Ag additive layers. The XRD pattern for the FePt film without an Ag additive layer (Sample A) showed fundamental peaks [(111), (200) and (220)] of the FePt alloy and a very weak superlattice peak (110) of the $L1_0$ FePt phase. This indicates that the deposition temperature of 400°C was not high enough to achieve a highly ordered FePt alloy. When an Ag layer was deposited as the underlayer (Sample B), intensity

Table 6-I. Layer structure and magnetic properties of FePt films with different thickness of Ag intermediate layers; $Hc_{//}$ – in-plane coercivity; $Hc_{\perp}$ – out-of-plane coercivity.

Sample	Film structures	$Hc_{//}$ (Oe)	$Hc_{\perp}$ (Oe)
A	Glass/FePt 15 nm	1098	1045
B	Glass/Ag 0.25 nm /FePt 15 nm	1629	1679
C	Glass/FePt 5 nm/Ag 0.25 nm/FePt 10 nm	2290	2931
D	Glass/FePt 10 nm/Ag 0.25 nm/FePt 5 nm	2489	2963
E	Glass/FePt 15 nm/Ag 0.25 nm	2751	3288

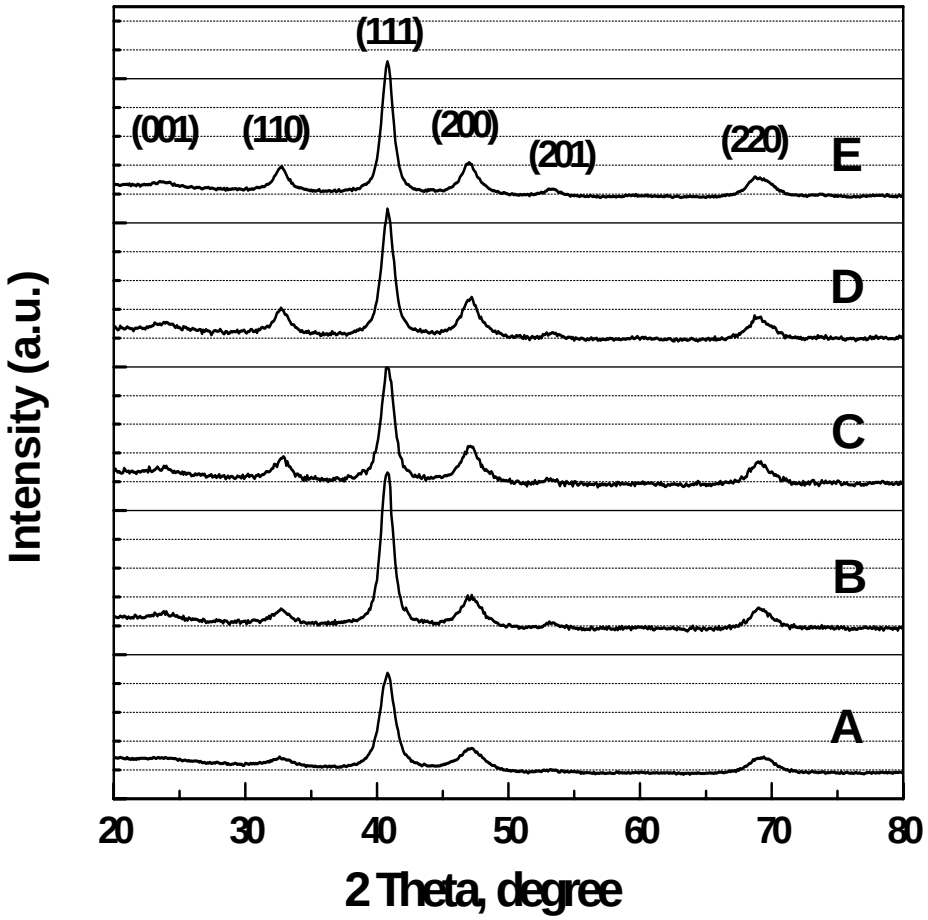

Figure 6-2. In-plane XRD patterns of FePt thin films with the different Ag additive layers; A-E represents the samples with different Ag layers in Figure 6-1.

for all the diffraction peaks became stronger, particularly the fundamental (111) peak. That is, the intensity for peaks of both the ordered and disordered phase increased with respect to Sample A without an Ag additive layer. The Ag underlayer may serve as nucleation sites for the crystallization of $L1_0$ FePt grains. After the deposition of Ag layers as the intermediate layer (Sample C) and top layer (Sample D), the intensity of the superlattice peaks such as (110) peak, increased further compared to those of Sample B. On the other hand, the intensity of the fundamental FePt (111) peaks did not increase with respect to the intensity of Sample B. This indicates that Ag intermediate layer and top layer may promote the ordering of the $L1_0$ FePt phase instead of promote the crystallization of the film.

While the XRD profiles of Samples C and D were very similar, the superlattice (201) peak of Sample E was much sharper than that of the other films. Additionally, the FePt (220) was broadened and split into two peaks, indicating the coexistence of the two disordered and ordered phases. The top layer is more effective than the intermediate layer in promoting $L1_0$ FePt phase transformation. On the other hand, the intensity of the fundamental (111) peak is much greater than that of Sample A. It suggests that the crystallinity of the film is promoted as well.

6.2.2 Magnetic properties

The variation of in-plane and out-of-plane coercivities with different Ag additive layers is shown in Table 6-I. For the FePt film without Ag additive layers (Sample A), the coercivity was 1.0 kOe in the two directions, indicating that FePt was isotropically orientated on the glass substrate and no texture was found. With the

deposition of the Ag underlayer, the coercivity in both directions increased to about 1.6 kOe. This suggests that the $L1_0$ FePt grains remained randomly distributed and the increase in coercivity might have been caused by the promotion of crystallization of the film with the Ag underlayer. The out-of-plane coercivity increased more than the in-plane coercivity of the films with deposition of the Ag intermediate and top layers (samples C, D, and E). When the Ag layer was deposited on top of the FePt film, the in-plane and out-of-plane coercivities increased to 2.7 and 3.3 kOe, respectively. This is in agreement with the XRD analysis because the ordering degree of the $L1_0$ FePt phase was the largest for FePt film with a top layer.

For samples C and D with intermediate layers, the in-plane coercivity increased to 2.3 kOe, and the out-of-plane coercivity increased to nearly 3.0 kOe. The large increase in the out-of-plane coercivity indicates that there is a high ordering of $L1_0$ FePt phase with the easy axis preferred normal to the film plane. The coercivity values for the two samples are nearly identical.

6.2.3 Magnetic interactions

Figure 6-3 shows the δM curves for the FePt films with different additive Ag layers, when the external field was applied in the film plane. As introduced in the methodology in Chapter 3, a deviation of δM may indicate intergranular exchange coupling or dipole interactions. [115,116] A positive deviation δM indicates the presence of exchange interactions, while negative δM means dipolar interactions. For the FePt film without Ag additive layers (Sample A), the δM curve shows a sharp positive peak, which indicates strong exchange coupling in the FePt film. For Samples C, D, and E

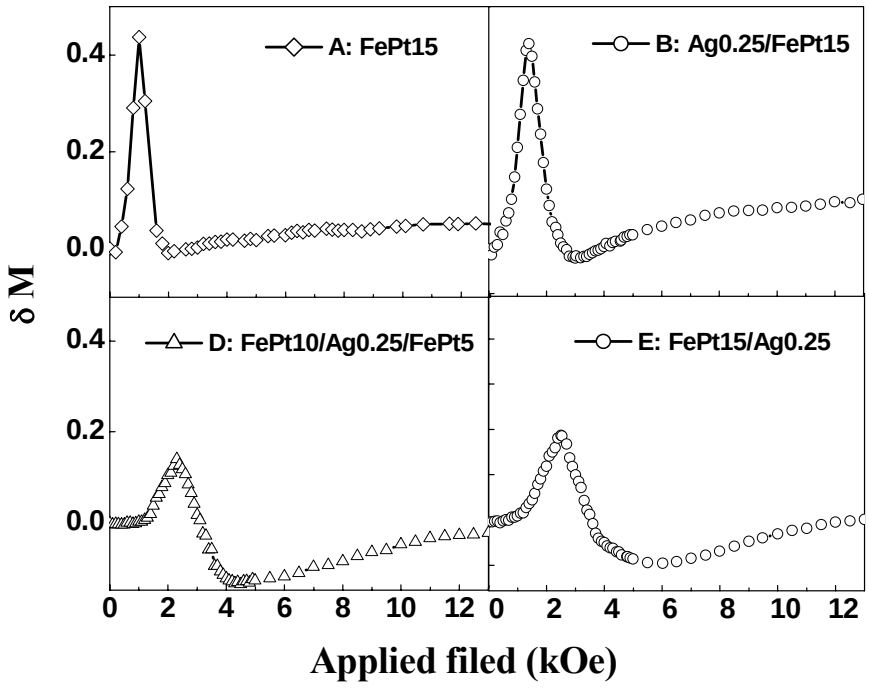

Figure 6-3. Variation of delta-*M* with different Ag additive layers with the external field applied in the film plane direction; the *δM* curve for Sample B with a sharp positive peak is smiliar with Sample A; the *δM* curve for Sample D with a small positive peak is smiliar with Sample C.

with Ag intermediate layers or top layers, the positive *δM* was significantly lower than that of Sample A. It indicates that the intergranular exchange coupling in these samples was reduced compared to that existing in Sample A. This may be attributed to the diffusion of the Ag atoms into the grain boundaries of the FePt films; the diffused Ag would separate the exchange coupled FePt grains. However, when an Ag underlayer was deposited (Sample B), the *δM* curve showed no significant change from that of Sample A. Reduced exchange coupling may also have contributed to the increase in coercivity of the FePt films with Ag intermediate or top layers. That is, the increase in coercivity with an ultrathin Ag intermediate layer or top layer was not only due to crystallinity that improved the $L1_0$ phase transformation, but also to a possible modification of the microstructure, which could lead to reduction of intergranular

exchange coupling. The SEM image of Sample E showed no Ag particles remained on the surface of the sample, but few Ag particles were observed on the surface of the FePt film with 1 nm Ag top layer above the FePt film. Thus, some Ag remained on the top of the FePt film with 1 nm Ag top layer, while nearly all the Ag diffused into the FePt layer with a 0.25 nm Ag top layer.

As seen in Table 6-I, the out-of-plane coercivity is larger than in-plane coercivity in FePt films with an intermediate or top layer, while the in-plane coercivities for Samples A and B were nearly the same of the out-of-plane values. The diffusion of Ag into FePt layers may change the texture of the FePt films by coordinating the competition between the strain energy and grain boundary energy. With a lattice mismatch of 5.5%, the preferential orientation Ag (111) may serve as a nucleation plane for the growth of the (111) plane of the $L1_0$ ordered FePt, as shown in the HRTEM image of Fig 5-7 and discussed in Chapter 5. Since the lattice parameter a (a = 3.86 Å) of the FePt is closer to that of the Ag (a = 4.08 Å) than c (c = 3.71 Å), FePt grains prefer to have their easy axis c normal to the film plane in order to reduce the strain energy.

From the above results and discussion, it is suggested that the intermediate layers inserted between magnetic layers have the same function of that of the top layers. That is, the deposited Ag may diffuse into the FePt magnetic layers to reduce the exchange coupling between FePt grains and result in the enhancement of coercivity of FePt films. Furthermore, the surface roughness caused by the top layer will be diminished with the layer inserted between magnetic layers.

6.3 Summary

Ultrathin Ag layers were studied as underlayer, intermediate layer, and top layer. Their magnetic properties of the FePt films were investigated. As an underlayer, Ag might not diffuse into the FePt film and the major function of the ultrathin Ag underlayer is to increase the crystallinity of the FePt films.

On the contrary, the diffusion of Ag from the intermediate or the top layer promoted the phase formation of the $L1_0$ ordered FePt, and it also reduced the intergranular exchange coupling in the FePt film.

Chapter 7 Effects of intermediate layers on FePt films with perpendicular orientation

As discussed in the last two chapters, a nonmagnetic layer could enhance the coercivity of FePt films by promoting the disordered/ordered transformation. However, a non-magnetic top layer may result in grain growth and in increase of surface roughness in the FePt thin films and will inevitably increase the flying height between the magnetic head and recording media. The texture and out-of-plane coercivity were not sufficiently high for perpendicular magnetic recording. In this chapter, CrRu orientation layer will be introduced to induce the FePt perpendicular orientation. The influence of different intermediate layers deposited between FePt layers will be discussed in this chapter.

7.1 Experimental methodology

Figure 7-1 shows the schematic illustration of the layer structure of the FePt films. FePt thin films with the structure of Glass/ $Cr_{91}Ru_9$ (30 nm)/ Pt (4 nm)/ FePt/ Ag/ FePt/ Pt (2 nm) were prepared by *DC* magnetron sputtering. The argon pressure was kept at 10 mTorr for the deposition of the FePt layer and 3 mTorr for the other layers. An FePt magnetic layer and $Cr_{91}Ru_9$ layer were deposited onto corning glass substrates at 400 ^{o}C. Pt was sputtered as the buffer layer between the $Cr_{91}Ru_9$ underlayer and the FePt magnetic layer to avoid the diffusion of elements from underlayer to magnetic layer.[127] The CrRu underlayer with (002) texture in the film plane induced the ordered FePt (001) texture. The 5.8 % of lattice mismatch between

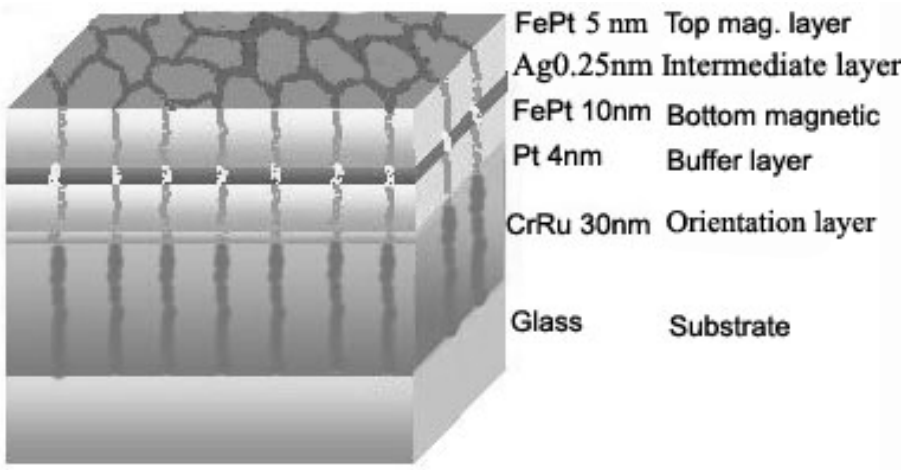

Figure 7-1. Schematic illustration of the layer structures of the FePt film; the substrate is glass and CrRu is an orientation layer to induce perperdicular orientation of FePt layer; Pt layer is a buffer layer to prevent Cr from diffusion into FePt layer; Ag layer is added to improve the magnetic properties.

Cr (002) and FePt (001) planes induced suitable tensile stress along the FePt *a* axis and expanded the *a* axis while contracting the *c* axis, easily forming an *fct* structure.

7.2 Results and discussion

7.2.1 CrRu as an orientation layer

Due to minimization of surface energy, FePt tends to show a (111) texture when it is directly deposited on a substrate.[94] To realize a perpendicular recording, it's necessary to make the easy axis perpendicular to the film plane. An orientation layer is of critical importance to grow the magnetic layer with the desired magnetization orientation and consequently the desired magnetic properties. In general the thin film microstructure involves the crystal structure, crystallographic texture, grain morphology, compositional segregation. Cr and Cr alloys, e. g. CrX (X=V, Mo, W and Ru.), which have a body centered cubic (*bcc*) crystal structure, are one of the most

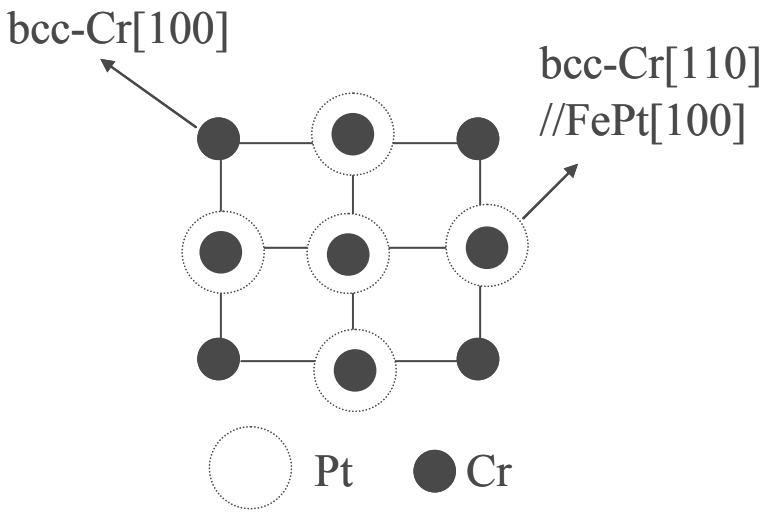

Figure 7-2. Schematic representative for the epitaxial growth of FePt on bcc-Cr substrate; black ball – Cr; open circle – Pt.

frequently used orientation layers.[94]

Figure 7-2 shows the schematic illustration of the epitaxial growth of FePt on *bcc*-Cr substrate. The FePt *fct*-(001) texture can heteroepitaxially grow with the crystallographic relationship Cr (002) [110]//FePt (001) [100]. Many papers have been published to discuss how the Cr underlayer affected the microstructure and magnetic properties of the magnetic layer. [99] The FePt *fct*-(001) texture can heteroepitaxially grow with the crystallographic relationship Cr (002) [110]//FePt (001) [100]. It was suggested that tensile stress along the FePt *a* axis is preferred to expand the *a* axis and to contract the *c* axis and thus form *fct* structure easily. In Ref. 94, Ru was doped in Cr to adjust the lattice parameter and hence to optimize the tensile stress between Cr orientation layer and FePt magnetic layer. Better quality of FePt *fct*- (001) texture was obtained and the intensity of the FePt superlattice (001) peak increases with Ru content up to Ru = 9.0 at.%. Further increasing of the content of Ru in the Cr underlayer resulted in a dramatic drop of the intensity of FePt (001) peak. The increase of the Cr

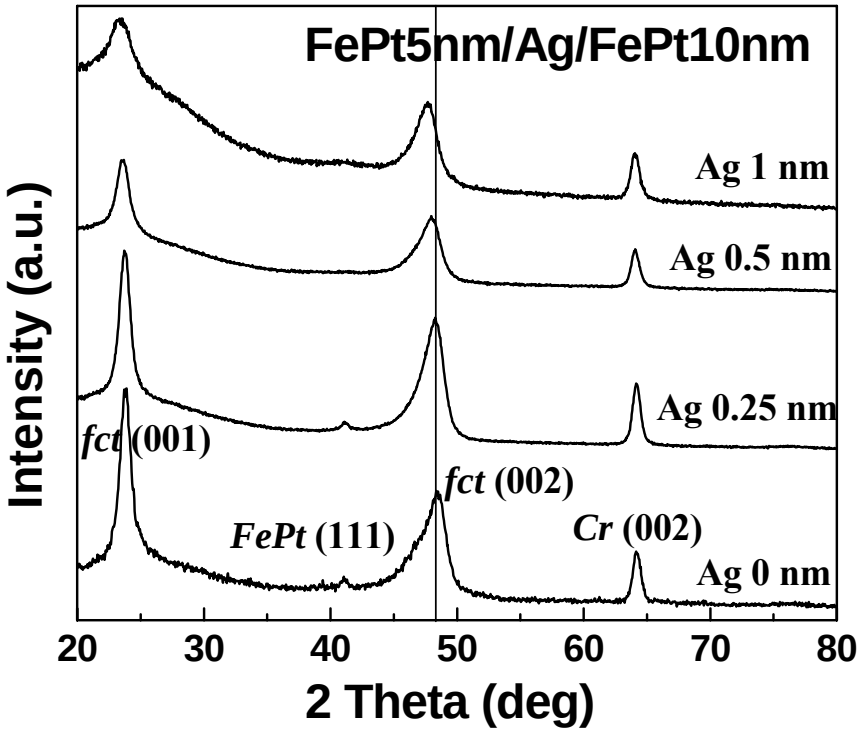

Figure 7-3 XRD θ-2θ spectra for FePt films with 0, 0.25, 0.5, and 1 nm Ag intermediate layer; superlattice (001) presents in the spectra; with increase of Ag layer to 1 nm, the (001) texture is gradually weaked and *fct* (002) peak shift to low 2θ angle.

lattice constant increased the lattice mismatch between the Cr (002) and the FePt (001) planes. This may result in the larger strain between FePt (001) [100]/Cr (002) [110], which was supposed to enhance the strain-induced *fct* phase formation. However, with further increase of the content of Ru up to 11.6 at. % in the Cr underlayer, the Cr lattice constant further increased. This may start to induce more stacking faults at the interface between the CrRu underlayer and the FePt magnetic layer, which may cause the relaxation of the expected strain. The strain relaxation between the CrRu layer and the FePt layer may result in the formation of a small amount of *fcc* FePt.

The lattice misfit linearly increases with the increase of the Ru content in the Cr underlayer, reaches a maximum at 9.0 at. % Ru, and then decreased. Accordingly, the

Table 7-I. Layer structure and magnetic properties of FePt films with different thickness of Ag intermediate layers and different deposition conditions; $Hc_{\perp}$ – out-of-plane coercivity; S – Squareness.

Sample	Film structures	$Hc_{\perp}$ (Oe)	S
A	Glass/CrRu/Pt/FePt 15 nm	2571	0.87
B	Glass/CrRu/Pt /FePt 5 nm/Ag 0.25 nm/FePt 10 nm	2831	0.92
C	Glass/CrRu/Pt /FePt 5 nm/Ag 0.5 nm/FePt 10 nm	2730	0.89
D	Glass/CrRu/Pt /FePt 5 nm/Ag 1 nm/FePt 10 nm	2115	0.85

out-of-plane coercivity increases with the Ru content and reaches the maximum at 9.0 at.% Ru, then decreases rapidly with a further increase of the Ru content in the Cr underlayer. The in-plane coercivity increases first and then decreases, down to the lowest value at 9.0 at. % Ru. These results indicate that an adequate lattice mismatch between the FePt (001) plane and the Cr (002) plane can result in the desired (001) orientation of the FePt film.

7.2.2 Ag as intermediate layers

Figure 7-3 shows the θ–2θ XRD spectra of the FePt films with different thickness of Ag intermediate layers. The XRD results show no change before and after the Ag intermediate layer of 0.25 nm was inserted, suggesting that the insertion of Ag intermediate layer would not affect the crystallographic orientation of the FePt film. However, when the Ag thickness is increased from 0.25 to 1 nm, the intensity of FePt *fct* (001) peak significantly decreased and the FePt *fct* (002) peak shifted to lower angles. This indicates that the perpendicular orientation of the *fct* FePt phase is

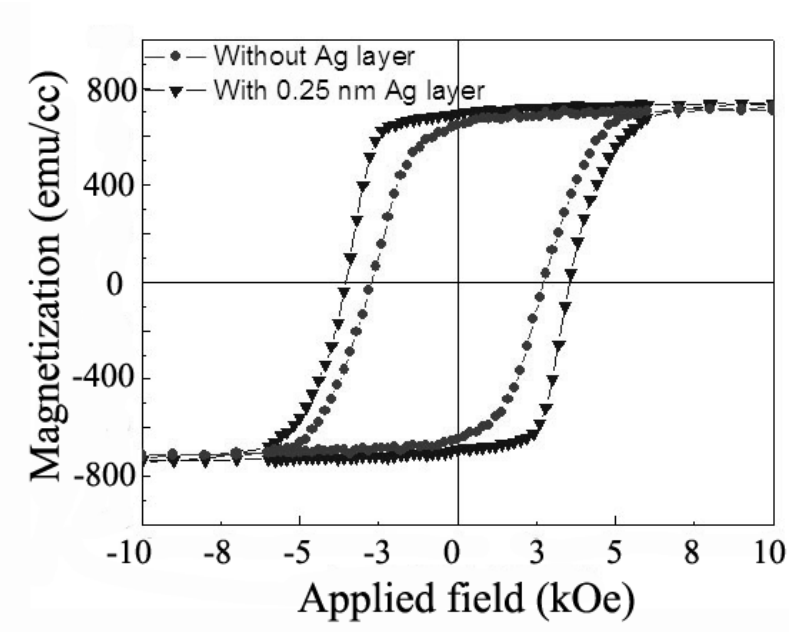

Figure 7-4. Out-of-plane hysteresis curves for FePt films with and without 0.25 nm Ag intermediate layer; solid circle – FePt film without Ag intermediate layer; solid triangle – FePt film with 0.25 nm Ag intermediate laver.

slightly changed.

The out-of-plane coercivities and remanent magnetization squareness for different FePt film structures are shown in Table 7-I. Perpendicular anisotropy was observed for the samples with an Ag layer of 0.25 nm. It was also reflected in the XRD pattern of the FePt film A. Figure 7-4 shows the typical out-of-plane hysteresis curves for the FePt films without and with 0.25 nm Ag intermediate layer. The out-of-plane curve has a coercivity of 3.5 kOe with remanent magnetization squareness of 0.94 for the sample with the Ag intermediate layer. It confirms that the perpendicular orientation of the FePt film with the Ag intermediate layer of 0.25 nm. The out-of-plane coercivity for the FePt film without Ag intermediate layer was 2.5 kOe, respectively. The largest out-of-plane coercivity and squareness appeared in the film with the 0.25 nm Ru layer (Sample B). With a 0.25 nm of Ag intermediate layer

inserted between the FePt layers, the out-of-plane coercivity increased to 3.5 kOe, a 40% increase over Sample A. The coercivity enhancement may be interpreted by the pinning induced interaction decoupling due to the insertion of Ag intermediate layer between FePt magnetic layers. The insertion of Ag intermediate layer between FePt magnetic layers might induce defects, e.g. dislocations, as pinning sites to impede the domain wall motion.

However, the out-of-plane coercivity decreased with further increase the Ag layer to 0.5 and 1 nm. This may be due to a destroying of the perpendicular texture of the FePt films due to the insertion of thicker Ag intermediate layer. The change of texture was reflected in the XRD profiles of samples with thicker intermediate Ag layers, as seen in Fig. 7-3.

7.2.3 A study on pinning effects

It was reported that the dislocations induced by the lattice misfit between FePt and Pt layers would pile-up in neighboring planes.[117] In our studies, the Ag intermediate layer may also play the same role because the perpendicular texture would not change with the ultrathin Ag intermediate layer deposited. Also the number and size of the defects could be controlled by the Ag layer. Thickness of the Ag layer could be one of the factors to introduce controllable defects that act as pinning sites to control the magnetization reversal process.

The pinning effect was more effective when defects had dimensions close to the domain wall thickness *(δ),*[118]

$$\delta = \pi (A/K)^{1/2} \qquad (7\text{-}1)$$

where,

A: the exchange coupling constant,

K: the magnetocrystalline anisotropy constant.

The relative small defects induced by the Ag intermediate layer of 0.25 nm in Sample B should have an average dimension comparable to that of the domain wall thickness of FePt film to enhance the film coercivity. On the contrary, relative large defects induced by thicker Ag intermediate layers in Sample D may have an average dimension that is larger than that of pinning sites. These large defects may serve as nucleation sites for nucleation of reversal domains. Therefore, the coercivity of these films is reduced.

The extrapolated anisotropy fields of Samples B and D from hysteresis curves were 20 and 16 kOe, respectively. The domain wall thickness can be calculated use Eqn. (7-1). If we use the same value for exchange coupling constant A, the domain wall thickness ratio of Samples B and D is

$$\delta_B/\delta_D = (K_B/K_D)^{1/2} = (16/20)^{1/2} = 0.89 \approx 1 \qquad (7\text{-}2)$$

Hence, from the above estimation, the domain wall thickness should be in the same magnitude in the two samples. If the defects for Samples B and D are of the same dimension, it is difficult to understand the drop of the coercivity for Sample D based on the domain wall motion pinning effect. The squareness and nucleation field of the out-of-plane curve of Sample D were also much smaller, perhaps due to larger dislocations or stacking faults (planar defects) formed at the interfaces of the Ag layer and the FePt magnetic layers. These defects were larger than the domain wall

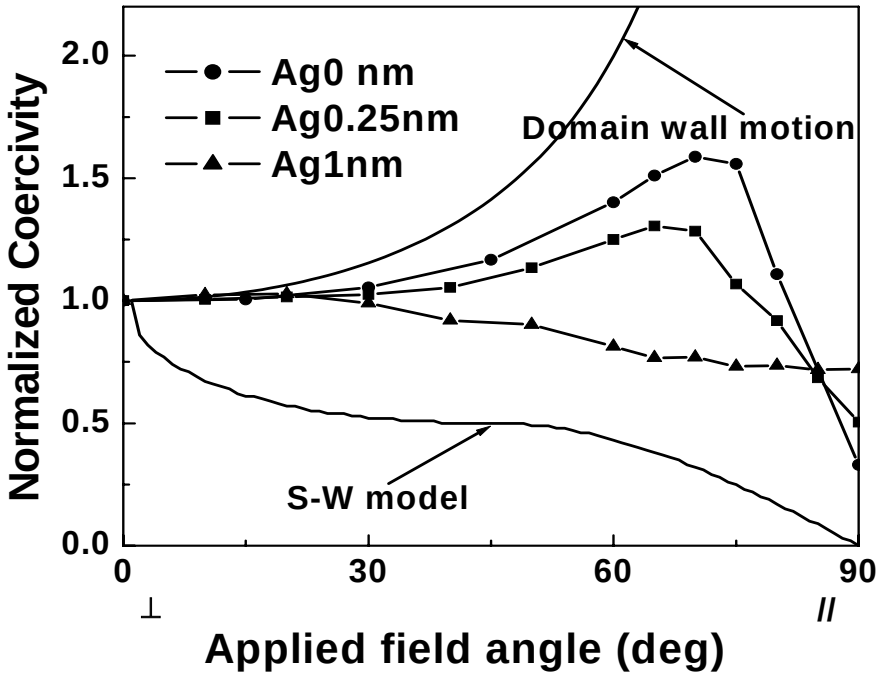

Figure 7-5. Angular dependence of coercivity for the FePt films with Ag intermediate layers of different thicknesses. The theoretical domain wall motion and nucleation model are also plotted. Zero field refers to film normal direction.

thickness *(δ);* thus, a higher localized demagnetization field would be induced at these locations. In other words, the defects introduced by a thick Ag layer (Sample D) may serve as nucleation sites rather than pinning sites. Consequently, the reversed domains would easily nucleate at these locations, and the measured coercivity would be smaller than that of the Sample A without an Ag layer and the Sample B with a thinner Ag layer.

Figure 7-5 shows the angular dependence of coercivity for FePt films with Ag intermediate layers of different thicknesses. The expected angular dependence profiles of domain wall pinning and the Stoner-Wohlfarth model are also shown in Figure 7-5. Generally, for a domain wall pinning mechanism, the coercivity is proportional to $1/\cos(\theta)$,[127] where θ is the angle between the applied field and easy axis of the

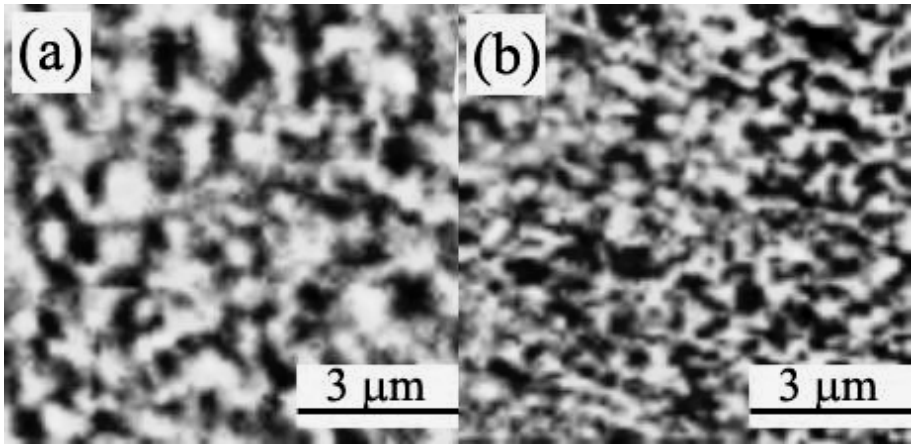

Figure 7-6. MFM images of FePt films: (a) Sample A film without Ag layer and (b) Sample B film with 0.25 nm Ag intermediate layer; the data bar is 3 μm for both figures.

uniaxial anisotropy. For the Stoner-Wolhfarth (S-W) rotation mechanism, the variation of coercivity with the angle θ is illustrated according to the S-W model.[104] The angular dependence of the coercivity profile for the FePt film without an Ag layer displayed typical domain wall pinning behavior. For the FePt film with the Ag intermediate layer of 1 nm; a pinning related rotation mode was dominant in the domain wall. This indicates that pinning effects might have been introduced into the FePt films by the Ag intermediate layers. As a characterization of the S-W rotation mechanism, the domain size in the films was reduced and exchange decoupling was realized in the FePt thin film with Ag intermediate layers.

Figure 7-6 shows the MFM images of the FePt thin films with and without Ag intermediate layer. The average magnetic domain size for Sample B is smaller than that of Sample A. The small domain size should have been resulted from the existence of pinning sites introduced in the FePt film by the insertion of the Ag intermediate layer.

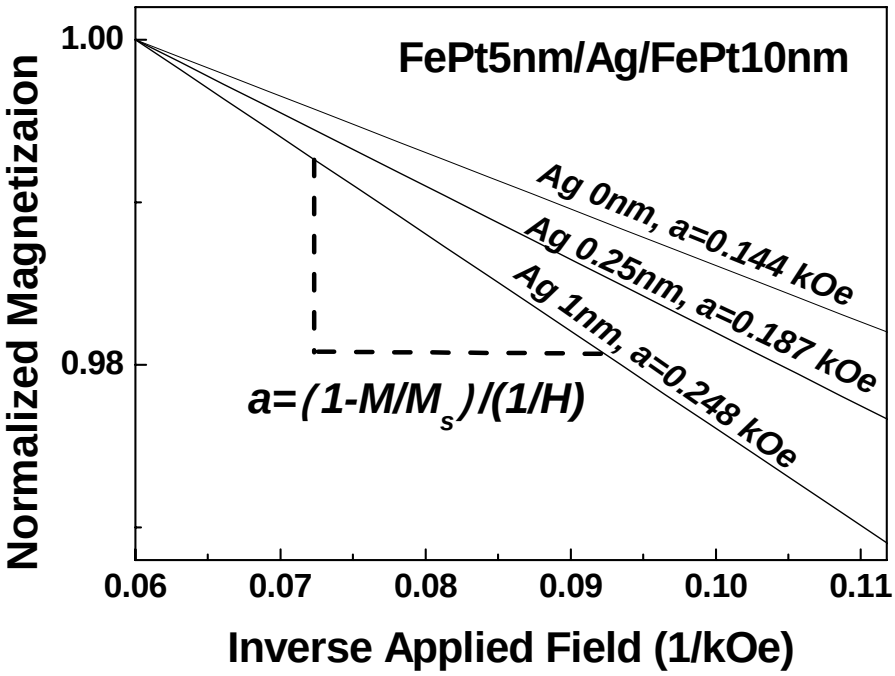

Figure 7-7. Normalized magnetization vs. inverse field for FePt films with different structures. The approach to saturation field ranged from 9 kOe to 15 kOe; the slope *a* represents the coefficient of magnetic hardness.

The defect information in magnetic films e.g., the relative levels or concentration of defects can be determined by comparing the high field behavior of the magnetization curve by the law of approach to saturation (LATS).[119-120] To investigate the defects in the thin films, the initial magnetization curves of films with Samples A, B, and D were measured by VSM. Figure 7-7 shows the normalized magnetization *vs*. inverse field for obtaining the magnetic hardness coefficient of films with Samples A, B, and D. Parameter *a* in the figure is the hard magnetic coefficient in the expression[119], as shown below:

$$M=M_s\,(1-a/H-b/H^2)+kH \qquad (7\text{-}3)$$

where,

M: the magnetization,
M_s*:* the saturation magnetization,

H: the magnetic field.
a, *b:* constants, the coefficient of magnetic hardness.

Parameters b and k were neglected when the applied field was selected in the range of approach to saturation field from 9 to 15 k Oe. According to the references,[119-120] the larger hard coefficient may relate with the larger defects. As expected, the film with Sample D had the largest hardness coefficient of the three samples, indicating potentially large defects. The smaller defects in Film with Sample B induced by the thinner Ag layer could form pinning sites to enhance the coercivity. However, the larger defects in the Sample D induced by the thicker Ag layer could serve as nucleation sites to undermine coercivity.

7.2.4 Different elements as the intermediate layer

To further investigate the effect of the intermediate layer, Ru or Pt ultrathin layer is deposited between two FePt magnetic layers to compare with the Ag intermediate layers. The layer structure was the same as that with Ag intermediate layers: Glass/$Cr_{91}Ru_9$ (30 nm) /Pt (2 nm) / FePt (5 nm) /Ru (or Pt) (0~1 nm) / FePt (10 nm). Nonmagnetic Ru or Pt intermediate layer was deposited between FePt magnetic layers to introduce desirable defects. $Cr_{91}Ru_9$ underlayer with (002) texture in the film plane induced the ordered FePt (001) texture. Pt layer was sputtered as the buffer layer between the $Cr_{91}Ru_9$ underlayer and the $Fe_{50}Pt_{50}$ magnetic layer to avoid the diffusion of elements from underlayer to magnetic layer.[127] The Ru or Pt layer with a thickness from 0 to 1 nm was deposited between the bottom FePt (5 nm) and top FePt (10 nm) magnetic layers to introduce the defects to form pinning sites.

Figure 7-8 summarizes the out-of-plane coercivity of the FePt films with different thicknesses of the Ag, Ru and Pt intermediate layers. The out-of-plane coercivity of the sample without an intermediate layer was approximately 2.5 kOe. The coercivity values increased when the Ag intermediate layer of 0.25 nm was inserted in the FePt film with respect to the film without intermediate layers. The enhancement of the coercivity is attributed to the pinning effects that induced by the appropriate defects by the Ag intermediate layer. However, when a Ru intermediate layer with the same thickness of Ag was inserted, coercivity only increased to 2.8 kOe. The *hcp* structure of the Ru element is different from the *fct* structure of FePt; the mismatch between the Ru and FePt layers was about 11 %. The defects formed in the interfaces by Ru intermediate layer were too large to form pinning sites to pin domain

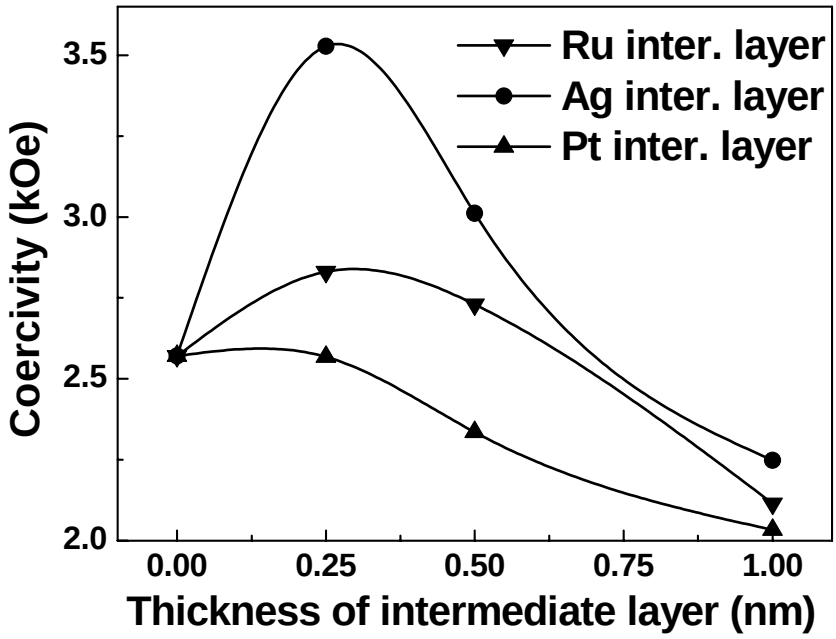

Figure 7-8. Variation of out-of-plane coercivity for the FePt films with Ru, Pt, and Ag intermediate layers of different thicknesses; down triangle – FePt film with Ru intermediate layer; circle – FePt film with Ag intermediate layer; up triangle – FePt film with Pt intermediate layer.

wall motion and would undermine the pinning effects and hereby to enhance coercivity.

Ag has an *fcc* structure that is close to *fct* of FePt structure and the lattice mismatch between Ag and FePt was about 5.8% and would form relatively small defects in the interfaces to act as effective pinning sites. Therefore, the increase of coercivity was relatively large when the Ag intermediate layer was deposited.

On the other hand, with Pt intermediate layers deposited between FePt layers, the coercivity of the film decreased with increase of the thickness of Pt layer. This may be due to diffusion of Pt into FePt layer as Pt is one of the components of FePt alloy. With Pt diffused into FePt layers, the content of the Fe and Pt will be aberrant from the stoichiometric composition and the coercivity of the film decreases.

With increasing the thickness of the Ru or Pt layers from 0.25 to 1 nm, shown in Fig. 7-8, the coercivity decreases to a value even less than the sample without intermediate layer. The thicker intermediate layer would introduce larger inhomogeneities in the interfaces. The larger inhomogeneities would serve as nucleation sites for the reversal domains that would undermine the coercivity of the FePt films. The XRD profiles of the FePt films with intermediate layers of different thicknesses showed no changes before and after 0.25 nm intermediate layers were inserted. When the thickness of the intermediate layers was increased to 1 nm, the FePt *fct* (002) peak shifted slightly to the lower angles, and the intensity of the FePt *fct* (002) peak decreased. These subtle changes indicate that the texture of the films was

interrupted by thicker intermediate layers. Consequently, the out-of-plane coercivity of the FePt films with 1 nm intermediate layers decreased.

The profiles of the angular dependence of coercivity for FePt films with Ru intermediate are different from that of FePt films with Ag intermediate layers. A pinning related rotation mode was dominant in the film with Ru intermediate layers. This indicates that pinning effects might have been introduced into the FePt films by the Ru intermediate layers, where the domain size in the films was reduced and decoupling was realized in the FePt thin film with Ag intermediate layers.

7.3 Summary

Ag, Ru and Pt were deposited as the intermediate layer between FePt magnetic layers to enhance the coercivity in FePt perpendicular media. Comparing with Ru and Pt layers, Ag is the best candidate as the intermediate layer because Ag has a similar structure of FePt and Ag can not form alloy with FePt.

With the diffusion of the atoms from the intermediate layers into the magnetic layers, the intergranular exchange coupling in the FePt film reduced. Additionally, the smaller defects introduced by the thin intermediate layer with a nominal thickness of 0.25 nm may form pinning sites to enhance the coercivity of the FePt film. On the other hand, larger defects introduced by a thicker intermediate may serve as nucleation sites to decrease the coercivity of the films.

Chapter 8 Effects of intermediate layers on FePt films with MgO substrates

As discussed in the last chapter, the intermediate layers are effective to improve the phase transformation of the ordered $L1_0$ phase FePt. However, the coercivity obtained for FePt film deposited on glass substrate is probably limited by the amorphous properties of glass substrate. Epitaxial growth of the FePt (001) films on MgO (100) single crystal substrate is widely reported.[123-126] In this chapter, $L1_0$ phase FePt thin films deposited on MgO (100) single crystal substrate with large magnetocrystalline anisotropy are investigated with a deposition temperature of 400 ^{o}C. With ultrathin Ag intermediate layers inserted between FePt layers, the perpendicular coercivity of the FePt film increased to 32.5 kOe. Exchange coupling between the FePt grains was reduced. A magnetization reversal mechanism changing from the domain wall pinning mode to a non-interaction single domain rotation mechanism is observed with Ag intermediate layers inserted between FePt layers.

8.1 Introduction

The key limiting factor in achieving areal density over 1 Tbit/in^2 is the superparamagnetic effect (thermal stability) in recording media.[20] As the recording areal density increases, the recording units become smaller. To keep the recording media readable, a minimal signal to noise ratio, *SNR*, should be kept. Since the *SNR* is approximately proportional to the number of magnetic grains per bit, the grains must be shrunk to achieve a larger *SNR*.[15] Limitations arise because the energy in magnetic grains become so small as to be comparable with the ambient thermal energy.[121] As

discussed in the Chapter 1, in order to avoid thermal instabilities, a minimal stability ratio of stored magnetic energy K_uV to thermal energy K_BT, or $K_uV/K_BT > 60$, is required for data storage time of 10 years,[21, 22] hence, higher K_u materials are needed to maintain stability.

Coercivity is another important parameter for high density recording media. The critical size of stable domain (here could be the bit size) against demagnetization is given as Equation (8-1).[122]

$$D_0 \cong \frac{4(AK_u)^{1/2}}{\mu_0 M_s H_c} \qquad (8\text{-}1)$$

Where,

A: the exchange coefficient,
K_u: the anisotropy field,
μ_0: vacuum permeability,
M_s: the saturation magnetization,
H_c: the coercivity.

The above equation shows clearly that high coercivity is required for high density recording media (with nano-sized bits). Heat assisted magnetic recording (HAMR) is proposed for high coercivity media with a high-recording density.[123-125] However, with "excessively" high K_u, the media become harder to be magnetized.[123] HAMR is one approach that has been proposed to overcome the writability problem of the Tbit/in^2 recording media.[125] HAMR involves producing a hot spot, usually with a laser, on the recording media while data is simultaneously written. Rapid cooling afterwards effectively freezes the written bit in its state. This technique allows the use of materials with extremely high coercivity values at ambient temperature at which writing would normally not be possible. Combined with the perpendicular recording, HAMR could offer areal density above 1Tbit/in^2.

For certain magnetic materials, the values for A, K_u, and M_s are constant; that is, the stable domain size is inversely proportional to the coercivity of the material. Therefore, high coercivity is critical for high recording density media. The $L1_0$ ordered FePt with a large magnetic anisotropy of the order of 7.0×10^7 erg/cc has received great attention because of its potential for recording HAMR media with ultrahigh density. The epitaxial growth of FePt films with the *c* axis normal to the film plane was investigated by conventional deposition techniques[126] such as sputtering and molecular beam epitaxy (MBE). In most cases, however, the coercivity realized in highly ordered FePt films was less than 10 kOe. Recently, Shima presented FePt thin film with coercivity as high as 70 kOe at room temperature.[127] However, the high coercivity required a high temperature as high as 780 ^{o}C. The high deposition temperature resulted in a large grain size of about 50 nm.[126-127] The large grain size impedes the FePt being applied as the recording media with ultrahigh density and the high fabrication temperature at ultrahigh vacuum is formidable for FePt application and even for lab research. In this chapter, coercivity larger than 30 kOe has been obtained at 400 ^{o}C with ultrathin Ag layers deposited between FePt layers.

8.2 Experimental methodology

FePt thin films were deposited in a high-vacuum. The corning glass and single crystal (100) MgO substrates were attached to a rotating substrate holder and were heated to 400 °C prior to deposition. The nominal total thickness of the FePt film was fixed as 15 nm. Figure 8-1 shows the illustration structures of the samples with and without Ag intermediate layers. In Structure I, 15 nm FePt was deposited on the (100)

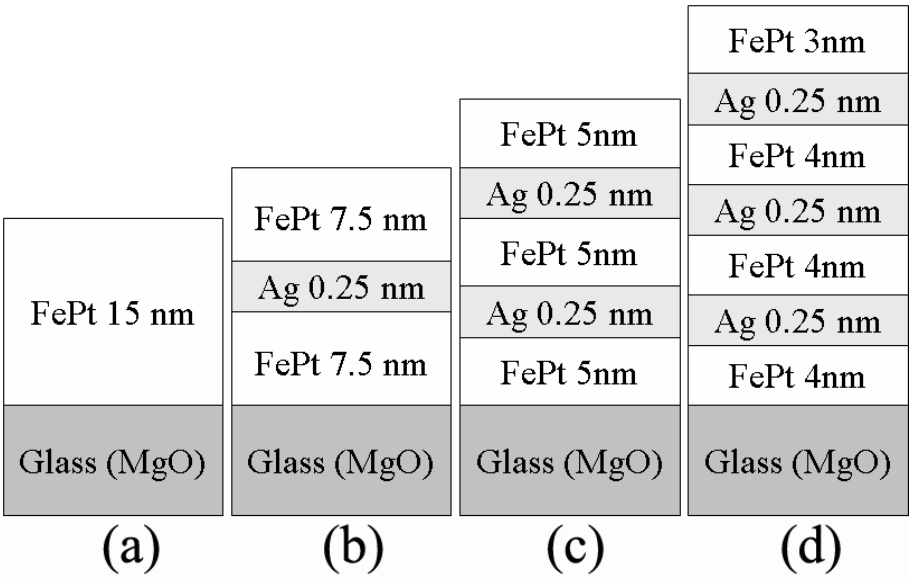

Figure 8-1. Schematic representation of FePt films with Structures I, II, III, and IV, in fig. (a), (b), (c) and (d), respectively. The total nominal thickness of the FePt layers for each sample was 15 nm. While only one FePt layer was deposited in Structure I (fig. (a)), the 15 nm FePt film was divided into two (Structure II), three (Structure III), or four layers (Structure IV) by ultrathin Ag layers with thicknesses of 0.25 nm in fig. (a), (b), and (c). Actually, the 0.25 nm Ag may not form a continuous layer as shown in the figure, but would be called a layer for convenience.

MgO single crystal (or corning glass) substrates (Fig. 8-1a). In Structure II, two FePt layers with a thickness of 7.5 nm were separated by one Ag layer with a nominal thickness of 0.25 nm (Fig. 8-1b). In Structure III, three FePt layers with a thickness of 5 nm were separated by two Ag layers with a nominal thickness of 0.25 nm (Fig. 8-1c). In Structure IV, four FePt layers with a total thickness of 15 nm were separated by three Ag layers with a nominal thickness of 0.25 nm (Fig. 8-1d). The crystallographic texture of the films was studied at room temperature using Cu K_α X-ray diffractometer (XRD). Magnetic properties of the films were measured with a Superconducting quantum interference device (SQUID) with a maximum applied field of 70 kOe. The surface morphology was examined by an atom force microscopy

(AFM). Magnetic domains observation was performed by a magnetic force microscopy (MFM). The film microstructure was studied by a JOEL 3010 transmission electron microscopy (TEM) at 300 kV.

8.3 Results

8.3.1 XRD analysis

Figure 8-2 shows the θ–2θ XRD patterns of the FePt films with glass and MgO single crystal substrates. Fig. 8-2a shows the XRD scans for the FePt films deposited on glass substrate. Except for the amorphous hump of the glass substrate, only a fundamental FePt (111) peak showed up in the film without intermediate layers inserted (Structure I). No superlattice peaks present in the XRD pattern indicates that the disordered *fcc* phase dominates in this film and the current deposition temperature of 400 °C is not high enough to achieve a highly ordered FePt alloy on glass substrate. With Ag ultrathin layers inserted between FePt layers (Structure III), the superlattice (001) peak showed up against the amorphous hump of the glass substrate and additional peak such as (002) peak appears. It indicates that the intermediate Ag layers are effective to promote the ordering of the $L1_0$ FePt structure. Calculated from the (111) peak using Scherrer's formula, the crystalline size is about 6 nm in the film with Structure I, and it almost keeps the same size in the film with Structure II. The calculated crystalline size is comparable to the grain size of FePt film grown on glass that observed by TEM, seen in Fig. 5-6.

Figure 8-2b shows the θ–2θ XRD patterns of the FePt films on the substrates

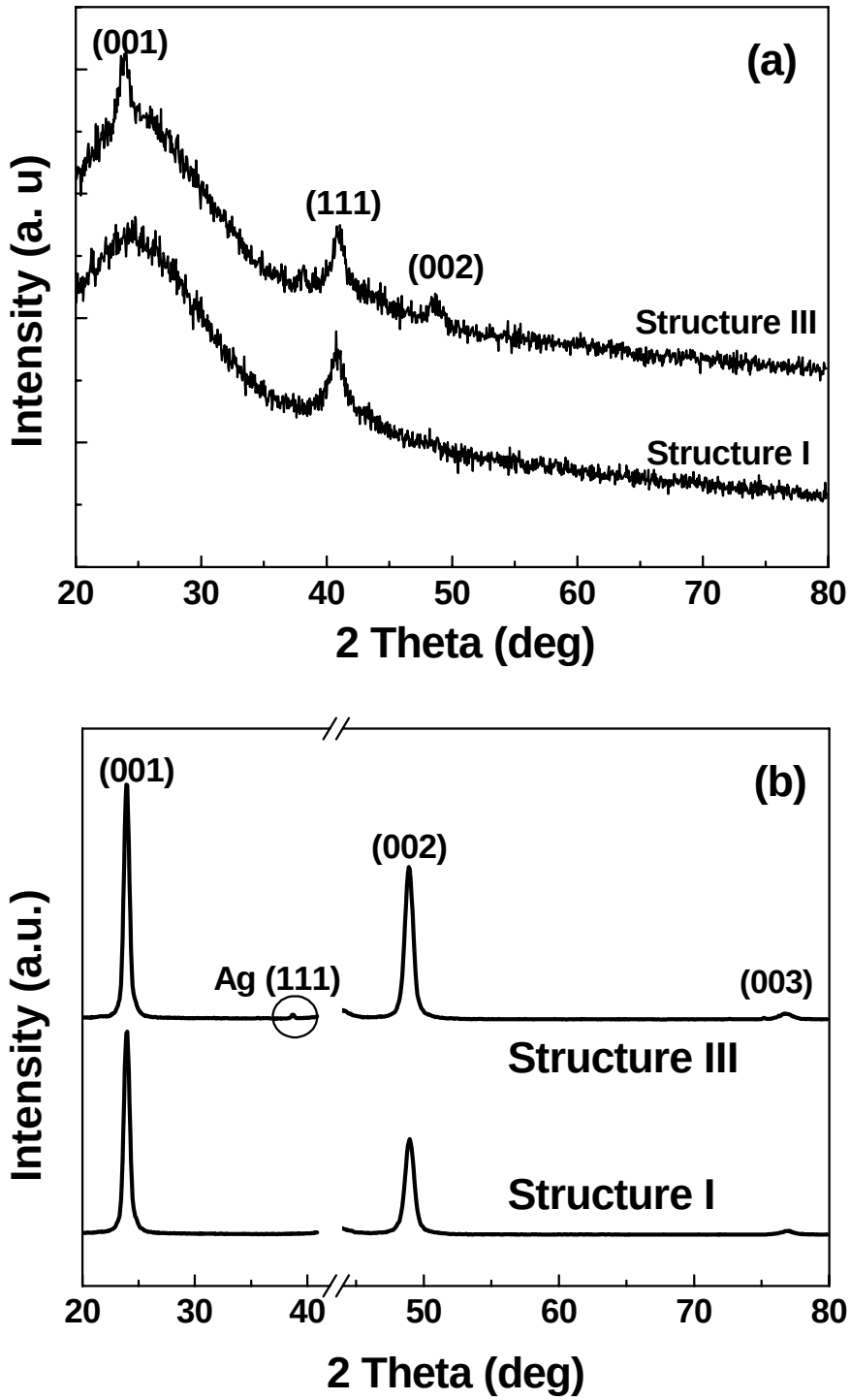

Figure 8-2. θ-2θ XRD patterns of the FePt films with and without Ag intermediate layers on (a) Corning glass and (b) MgO (100) single crystal substrates. Deposited on glass substrate, a strong (111) texture is presented in the FePt film; deposited on MgO substrate, a dominated (001) texture is presented in the FePt film, while the Ag (111) peak appears in the XRD profile of Structure III.

of MgO (100) single crystal. The 2θ range from 42-44 degrees is cut from the curve because the intensity of the single crystal MgO (100) peak was so much greater than that of the FePt peaks. No other peaks, except the *fct* superlattice (001), (002), and (003) peaks, were observed in the XRD pattern, indicating that the film was oriented in the (001) direction (out-of-plane). Thus, single crystal (001) MgO is a suitable candidate to introduce the (001) orientation of the FePt film. Evidence of $L1_0$ ordering appeared as a superlattice (001) ordered FePt peak and (002) peak in the film with Structure I. Calculated from the (002) peak using Scherer's equation, the crystalline size was about 11 nm in the film with Structure I. Crystallization improved for films grown on MgO substrates. Even so, the crystalline size was much smaller than the 50 nm obtained at 700 ^{o}C by Shima.[127] With the Ag layers deposited between FePt layers; the crystalline size calculated from XRD increased only to12 nm for the film with Structure III. No significant change for the diffraction peaks was observed except that the intensity of all the peaks of film with Structure III was larger than those of the film with Structure I. The increased intensity indicates that crystallization in the film was improved by the addition of Ag layers. These results also suggest that the (001) orientation of the FePt film was not affected by the insertion of the two ultrathin Ag intermediate layers. Additionally, the slight (111) Ag peak was observed in the pattern of the film with Structure II, suggesting that the Ag did not form solid solutions with FePt. However, the ordering parameter for the Structure I and III is 0.86 and 0.88, respectively. It indicates that the addition of an Ag layer would only slightly help the ordering of FePt films.

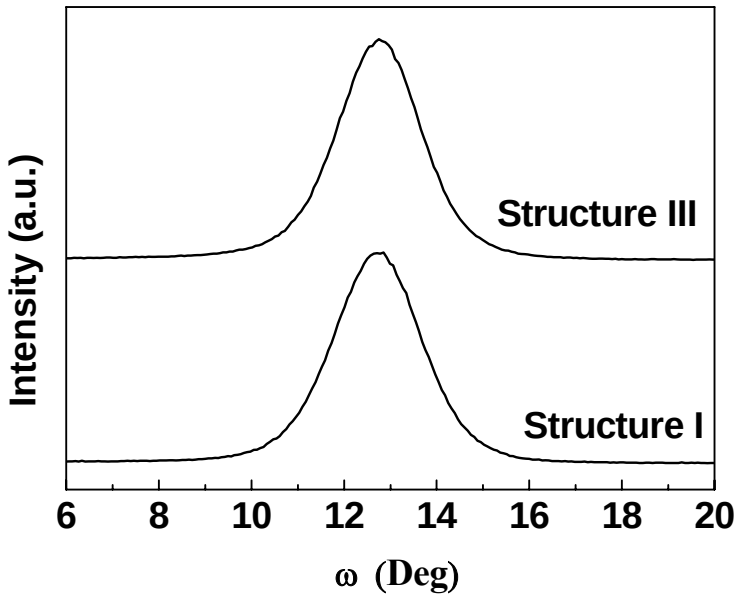

Figure 8-3. Rocking curve of the FePt *fct* (001) peak of FePt thin films with and without Ag intermediate layers. The degree for the rocking curve is nearly the same for both the structure I and III.

Figure 8-3 shows the rocking curves of the FePt $L1_0$ (001) peaks. The full width at half-maximum (FWHM) of the rocking curve was about 2.6 ° for the film with Structure I. Although the growth of FePt was interrupted by the deposition of the two Ag intermediate layers, the FWHM for the Structure II was nearly identical to that of Structure I. This again confirms that the crystallographic texture of the film was not influenced by the insertion of the Ag intermediate layers.

8.3.2 Plane view TEM microstructure

Figures 8-4a and 8-4b shows the TEM plane view of bright field images of the FePt films (Structure I and Structure III, respectively). Large amount of Moiré fringes are observed in the both images as a result of the double diffraction from FePt grains and MgO substrate. Without Ag intermediate layers inserted, the morphology shows a continuous structure in Fig 8-4a. On the other hand, the morphology becomes an

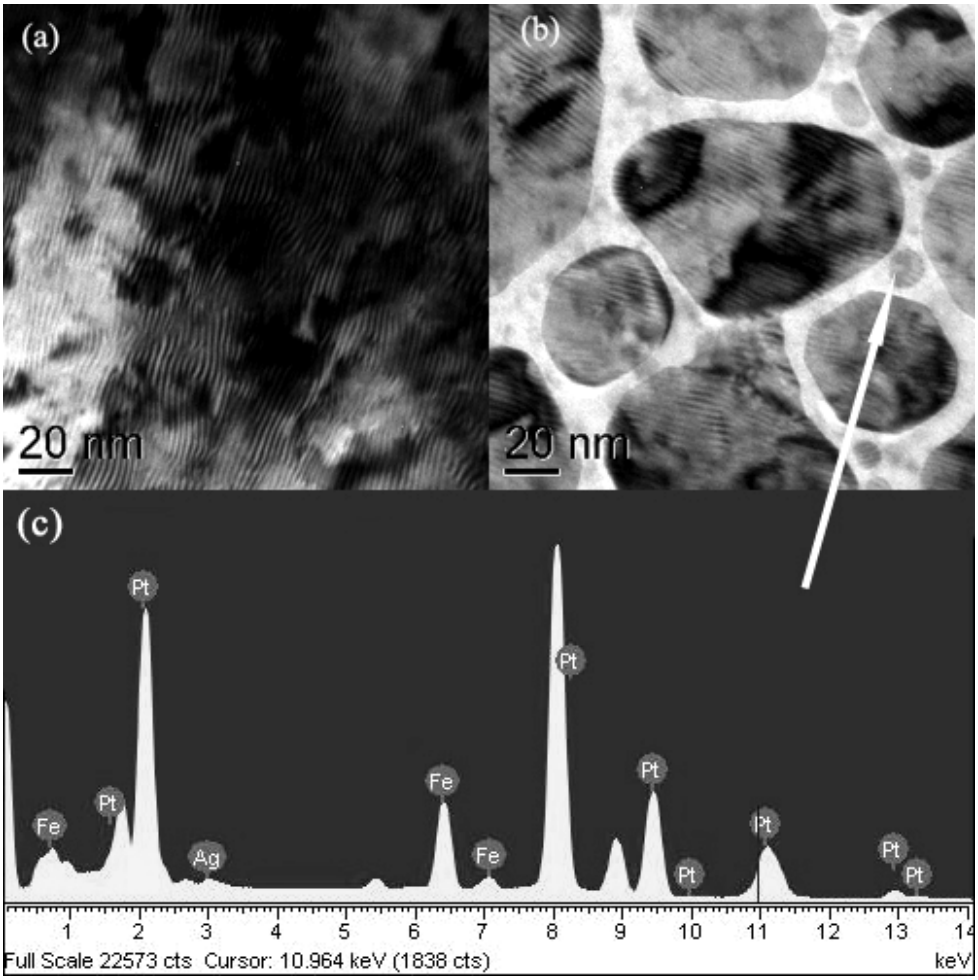

Figure 8-4. Plane view TEM images of FePt thin films with (a) Structure I and (b) Structure III and (c) EDX profile of the arrow pointed small particle in Fig. 8-4b; the data bar is 20 nm for both images; in Fig. (a), the morphology is a continuous structure; in Fig. (b), the morphology becomes an isolated island structure with Ag intermediate layers.

isolated island structure with Ag intermediate layers inserted, seen in Fig 8-4b. It indicates that the continuous lateral growth of the FePt film was interrupted by the insertion of Ag intermediate layers and resulting in the formation of the island structure. The particles are not uniform and the particle size varies from several tens of nanometers to about 100 nm and the separate gap is about 10-20 nm. There are also some small particles with particle size of several nanometers to about ten nanometers in the separate gap of the large particles. Fig. 8-4c shows the EDX profile of one

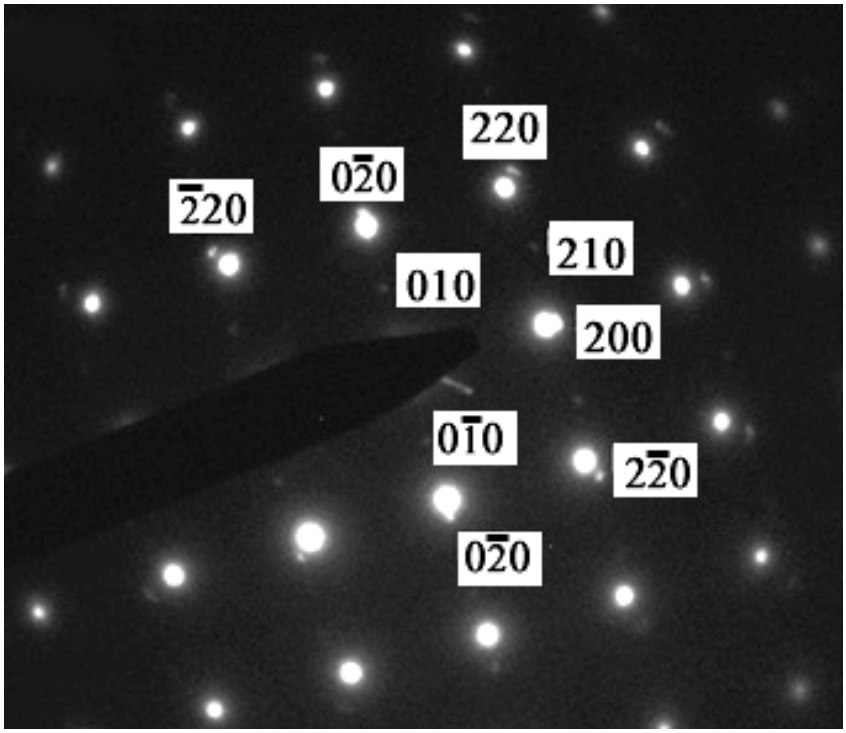

Figure 8-5. SAED pattern of Structure III film with Ag intermediate layers; the strong spots are diffracted from MgO single crystal substrate; the weak satellite diffraction spots diffracted from FePt illustrate the expitaxial growth of FePt on MgO substrate.

small particle (pointed with white arrow) in Fig. 8-4b. Although the dimension of the particle is as small as 10 nm, Ag is detected at the particle. It indicates that the particle may be Ag and the diffused Ag may stay in the gap of FePt particles.

Figure 8-5 shows the corresponding SAED pattern of the FePt film with [001] zone axis. The single crystal lattice of MgO was obvious indicated in the pattern; the diffraction spots from FePt were comparatively weak and satellite to MgO diffraction spots. The SAED pattern shows that the orientation relationship between the FePt film and MgO substrate was cubic-cubic; that is, $(020)_{FePt}$// $(020)_{MgO}$ and $<100>_{FePt}$//$<100>_{MgO}$. FePt (002), (200), and (202) fundamental diffraction spots with small discrepancy values accompanied with the MgO diffraction spots. Additionally,

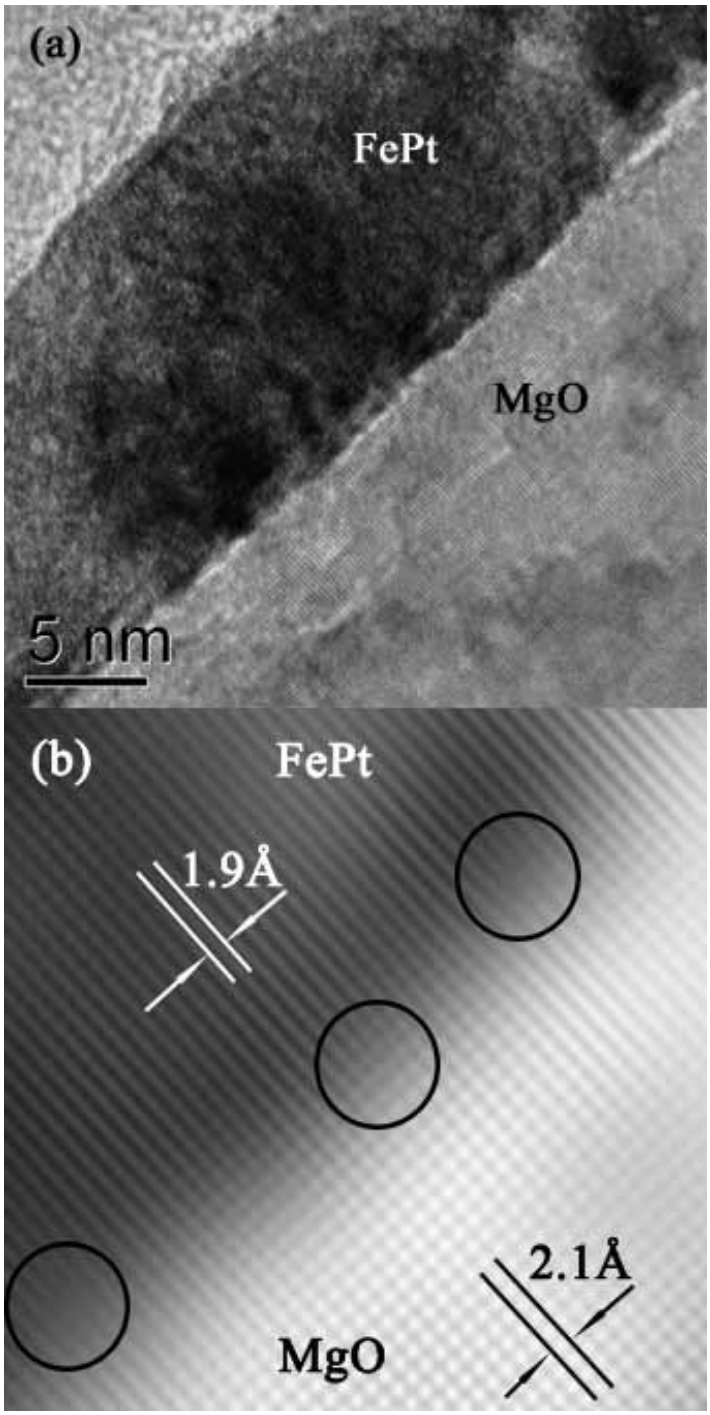

Figure 8-6. (a) HRTEM image of the FePt film with Structure III. (b) the reconstruction image using the FFT filtering technique of the corresponding image. The dislocations are marked with circles.

the FePt (001) and (210) superlattice spots with relatively weak intensity appeared.

Figure 8-6a presents a HRTEM image of the FePt film with Structure III and Figure 8-6b shows the enlarged view of fast Fourier transform (FFT) filtered image in Fig. 8-6a. The HRTEM image shows clear interface between the FePt film and the MgO substrate. The reconstruction image in Figure 8-6b clearly shows the epitaxial growth of the FePt (200) planes with *d* spacing of 1.9 Å on MgO substrate. The dislocations are marked with circles in the image. Dislocations with additional pile of atoms are observed to locate at the interface of the FePt film and MgO substrate. The dislocations at the interface may also contribute to the enhancement of the coercivity due to the pinning effect of the dislocation defects.

8.3.3 Magnetic properties

The coercivity values of the FePt films with different structures on glass and MgO substrates are listed in Table 8-I. With consistence to the result in Chapter 7, the coercivity for the film without Ag intermediate layer on glass substrate is about 1.0 kOe in both in-plane and out-of-plane directions. The low coercivity is well expected from the XRD pattern of the film that the disordered *fcc* FePt phase was the dominating phase when FePt was deposited on the glass substrate at the temperature of 400°C. While Ag intermediate layers inserted, both the in-plane and out-of-plane coercivities increased. It indicates that the Ag intermediate layers are effective to improve the coercivity of the FePt film.

The coercivities for the films grown on glass substrate are measured from VSM. According to the XRD analysis, seen in Fig 8-2b, when deposited on the MgO

Table 8-I. Layer structures and magnetic properties of FePt films with different thickness of Ag intermediate layers deposited on MgO single crystal and glass substrate; $Hc_{//}$ – in-plane coercivity; $Hc_{\perp}$ – out-of-plane coercivity.

	Film structures	MgO $Hc_{//}$ (kOe)	MgO $Hc_{\perp}$ (kOe)	Glass $Hc_{//}$ (kOe)	Glass $Hc_{\perp}$ (kOe)
I	Sub/FePt 15 nm	1.2	6.5	1.5	1.6
II	Sub/FePt 7.5 /Ag 0.25/FePt 7.5 nm	3.2	11.0	6.2	5.8
III	Sub/FePt 5/Ag0.25/FePt 5/Ag0.25/FePt 5 nm	6.5	32.5	5.0	4.3
IV	Sub/FePt4/Ag0.25/FePt4/Ag0.25/FePt4/Ag0.25/ FePt 3 nm	7.6	24.0	6.6	6.3

substrate, the (001) orientation of the FePt film was induced by the epitaxial growth on the single crystal MgO (100) substrate. The out-of-plane coercivity for the film with Structure I is 6.5 kOe and about 1 kOe for the in-plane direction. It indicates that not only the orientation of the easy axis is in the *c*-axis direction but also the coercivity of the films on the MgO substrate increased significantly. A 6.8% of the lattice mismatch between MgO and FePt may result in the rapid growth of the ordered FePt phase because of the strains.

Figure 8-7 shows the hysteresis curves for the FePt films grown on MgO substrate measured by SQUID with maximum applied field of 70 kOe. As illustrated in the XRD patterns (Figure 8-2b), the magnetic easy axis of the tetragonal FePt is normal to the film plane. The out-of-plane coercivity for the film with Structure I is 6.5 kOe, while in-plane coercivity is about 1 kOe (seen in Figure 8-7a). With an Ag layer inserted between FePt magnetic layers (Structure II), the out-of-plane coercivity doubled with respect to that of the FePt thin film without intermediate layer (Structure I). With two ultrathin Ag layers inserted between FePt layers, the out-of-plane

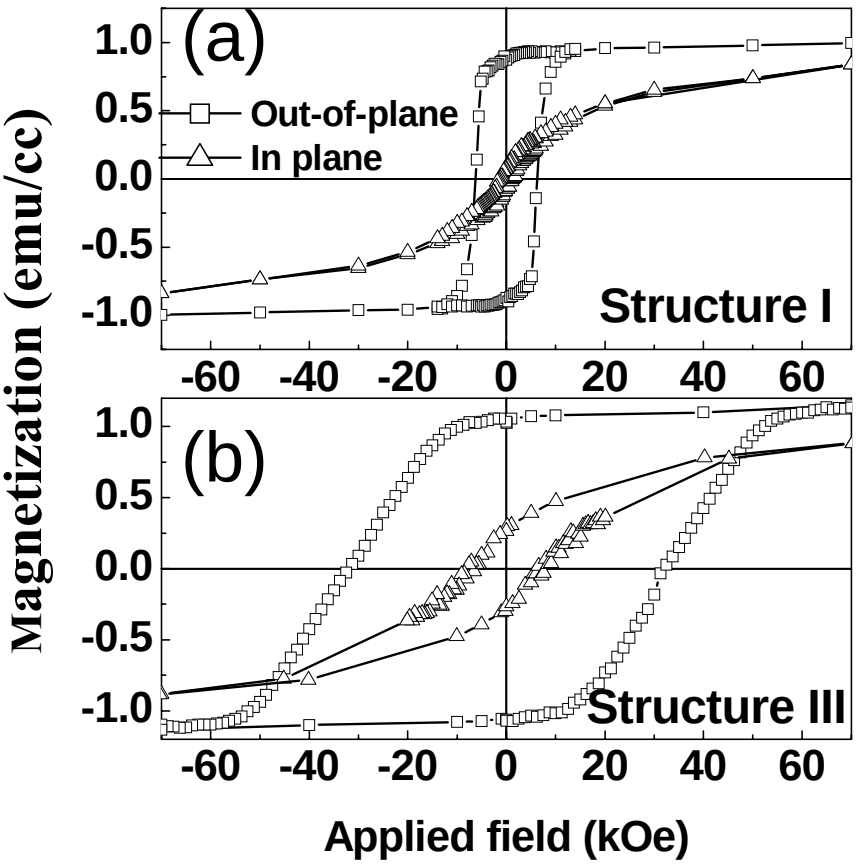

Figure 8-7. Magnetization curves for FePt films measured by SQUID with maximum applied field of 70 kOe. (a) for Structure I without Ag intermediate layer; (b) for Structure III with Ag intermediate layers; Squre – out-of-plane magnetization curves; triangle – in-plane magnetization curves.

coercivity of the film with Structure III dramatically increases to 32.5 kOe (Seen in Figure 8-7(b)). The extrapolated anisotropy fields from hysteresis curves are estimated to be about 70 kOe and 85 kOe for films with structure I and III, respectively.

Using $H_k=2K_u/M_s$, K_u is calculated to be $3.7\text{x}10^7$ and $4.3\ \text{x}10^7$ erg/cc for Structure I and III, respectively. However, with further increase of the number of Ag intermediate layers, the coercivity of FePt film with structure IV slightly decreased to about 24 kOe. Meanwhile, the in-plane coercivity keeps increasing to about 8 kOe.

These results indicate that the perpendicular texture of the film may be slightly destroyed by too many layers inserted into the FePt magnetic films.

8.4 Magnetization reversal mechanism

The drastic increase of the coercivity and anisotropy field should be attributed to the insertion of the ultrathin Ag layers because no other fabrication conditions have been changed except the film structure. From the in-plane TEM microstructure, as seen in Fig. 8-4b, the morphology becomes an island structure with Ag intermediate layers inserted.

In the hysteresis curves of the two films shown in Figure 8-7, the squareness S (the ratio of magnetic remanence M_r to the saturation magnetization M_s; large S is an important factor to keep the stored data) of the hysteresis curves of the two structures was nearly identical for the film with Structures I and III. The coercivity squareness S* ($\Delta H/Hc$) decreased from 0.66 in the film with Structure I to 0.38 in the film with Structure III. The decrease of the S* suggests that the exchange coupling decreased when Ag intermediate layers were inserted. As discussed in Chapter 5, the Ag was immiscible with FePt and would coalescent into Ag clusters and stay in the gap between FePt particles, as seen in Fig. 8-4b. These Ag may decouple the exchange coupling between the FePt particles and change the magnetization reversal mechanism of the FePt films. Additionally, because domain wall propagation is inhibited in islands, the large increase in the coercivity could be either due to decoupling of FePt particles, which promote the rotation-type of the magnetization reversal.[129]

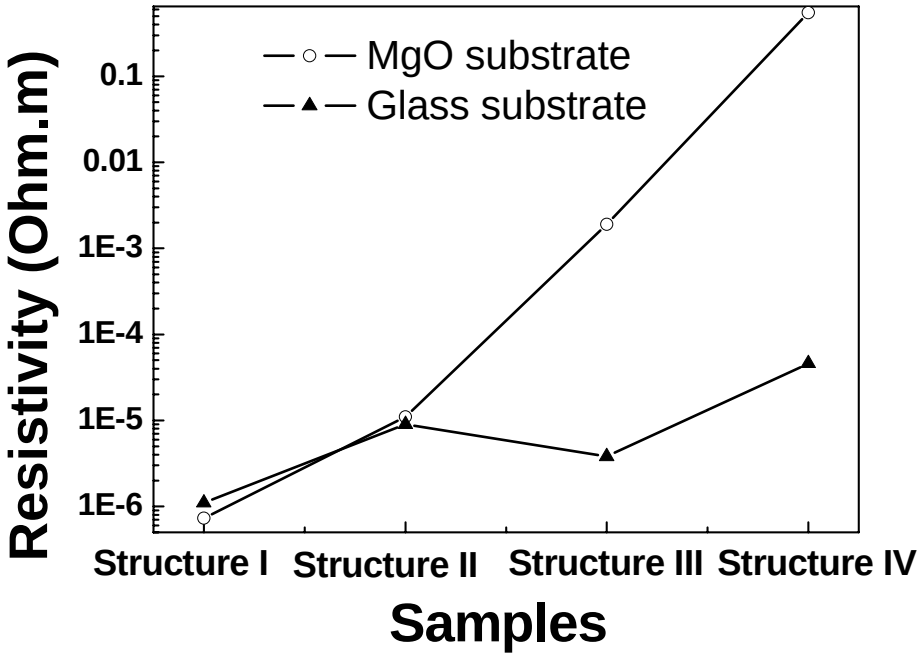

Figure 8-8 Variation of surface resistivity of FePt thin films on MgO single crystal and glass substrate with different intermediate layers. Blank circle – FePt film deposited on MgO single crystal substrate; solide triangle – FePt film deposited on glass substrate.

Figure 8-8 shows the variation of surface resistivity of FePt thin films with different intermediate layers deposited on glass and MgO substrate. The resistivity for the samples deposited on glass substrate varies slightly from the range of 1×10^{-6} (without Ag intermediate layers) to 1×10^{-5} Ohm·m (with Ag intermediate layers). It suggests that top morphology of these samples do not change too much with insertion of Ag intermediate layers. On the contrary, the resistivity of the samples deposited on MgO single crystal substrates dramatically increased from the 1.34×10^{-6} (without Ag intermediate layers) to 1×10^{-1} Ohm·m (with Ag intermediate layers). This phenomenon should be resulted from the significant modification of the surface morphology of the FePt films. The huge increase of the resistivity suggests that the continuous lateral growth of the FePt film is interrupted by the insertion of the Ag

intermediate layers and island structure is formed.

There are three modes of film growth in the thin film deposition. Frank-Van der Merwe mode is called two dimension (2D) layer-by-layer growth which consists of deposition of one monolayer at a time and results in a very smooth epitaxial film. [130] It occurs when the cohesive energy between the film and substrate atoms is greater than the cohesive energy of the film, but monotonically decreases as new layer is added. For a system that nucleates two-dimensional clusters on the substrate, the degree to which true full-monolayer growth will be achieved depends on the density of nucleated clusters. Obviously, the film with Structure I in this study is a kind of 2D layer by layer growth mode, which results in a continuous layer structure as observed in Fig. 8-4a. Three-dimensional (3D) island (Volmer-Weber) growth results in the formation and growth of isolated islands. This occurs when the cohesive energy of the film atoms is greater than the cohesive binding between the film and substrate atoms. This mode can result in an epitaxial film that has a rough surface, or a polycrystalline film containing voids. Mixed (Stranski-Kranstanov) growth consists of island growth after the formation of the first monolayer. It occurs when the monotonic decrease in binding energy with each successive layer is energetically overridden by some factor such as strain energy due to lattice mismatch and island formation becoming more favorable. The island structure observed in the film with Structure III should begin with an initial 2D mode and followed by the 3D growth mode. The mixed 2D-3D growth occurs at high temperatures when the surface diffusion length of the adatoms exceeds the average terrace width. The adatoms in this case migrate to the step edges,

where they find the most stable crystallization sites. The islands therefore start to form as the crystal grows. The formation of FePt island structure at high temperature in Ref. 127-128 is an example of this mixture mode. In our study, although the deposition temperature for the films with the two structures is as the same as 400 ^{o}C, the surface morphology of film with Structure III has changed from a continuous layer to an isolated island structure with Ag intermediate layers inserted between FePt magnetic layers. With Ag elements deposited in the process of growth of FePt epitaxial layer, large amount of strain is introduced into the FePt layer. The formation of island structure is favorable to release of the strain on the interface of the FePt film and the MgO substrate.[131]

The change of the surface morphology was also observed while growth of Fe on single crystal MgO by Boubeta et. al.[132] In Ref. 132, with the increase of temperature from 400 to 700 ^{o}C, the morphology of the Fe film changed from dendrites to islands due to the large surface-diffusion at high temperature. In our work, the deposition of the Ag should have impeded the formation of FePt interconnection network and promoted the formation of island morphology at relatively low temperatures. The large increase of coercivity should be attributed to the realization of the non-interaction mechanism of isolated-island structure in film with Structure III.[126] The non-interaction between particles also explains the small coercivity squareness S* of the hysteresis curve in film with Structure III (Fig 8-11b).

Figure 8-9 shows the surface morphology and magnetic domain structures of the films with Structures I and III measured with the AFM and MFM. The particle size

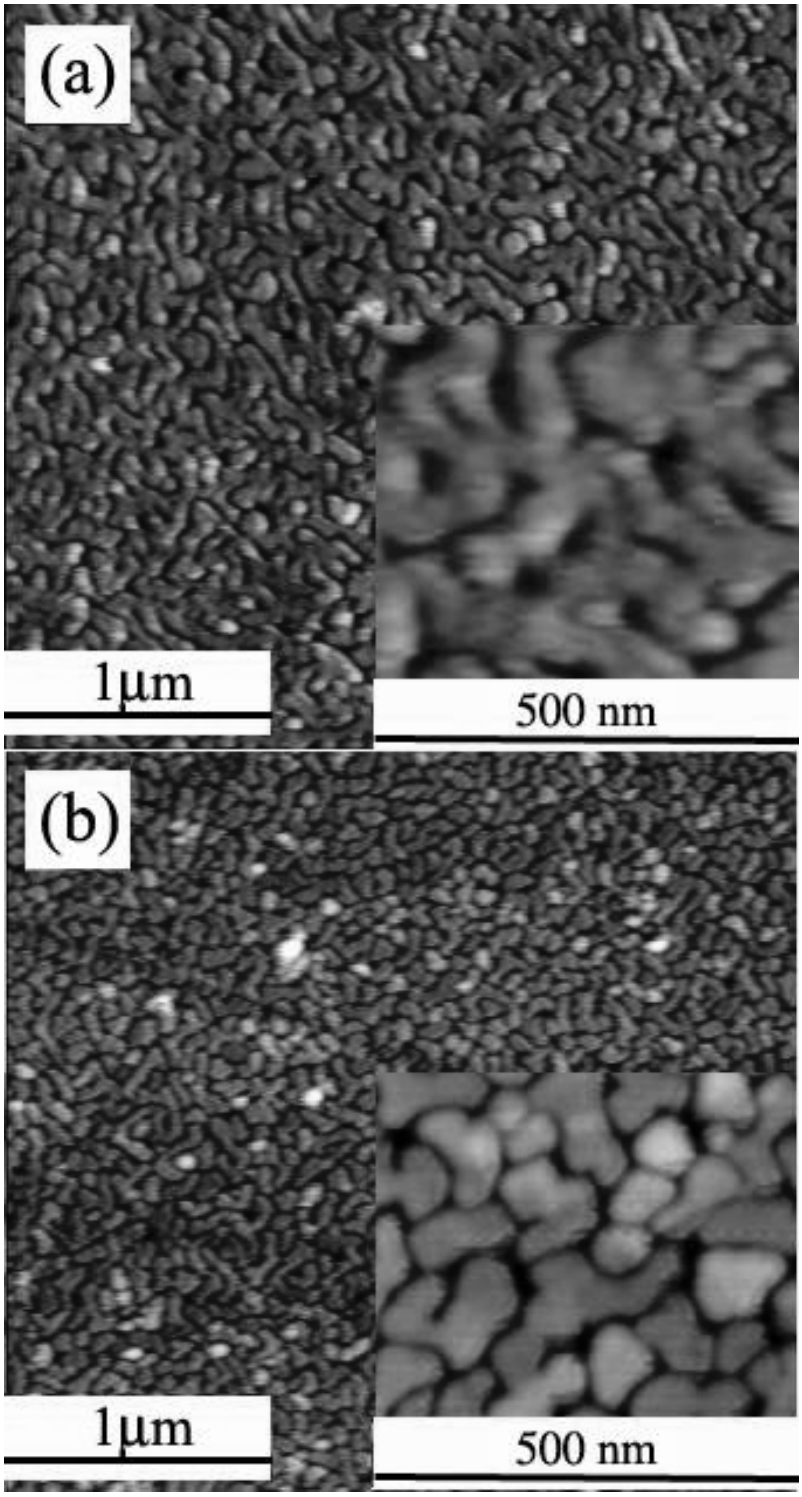

Figure 8-9. AFM images of FePt thin films; (a) FePt film of Structure I without Ag intermediate layers; (b) FePt film of Structure III with Ag intermediate layers; the scale bar is the 1 μm; the insets in the pictures are the enlarged view of the AFM images. The scale bar is 500 nm.

observed by the AFM was obviously larger than the crystalline size obtained from TEM (Seen in Fig. 8-4). The difference was due to the coalescence of the grains on the film surface. The morphology of the film with Structure I showed an interconnected maze-like pattern. The width of the maze was about 100 nm; the length was several times of the width. The MFM observation was performed from the same area measured by the AFM. The magnetic domain size seen by MFM was much larger than the particles observed in the AFM image. This indicates that the interconnected maze-like particles would couple together to form magnetic domains in the film with Structure I.

When two Ag intermediate layers were inserted between FePt layers (Structure III), the AFM morphology changed from a maze-like interconnection to an isolated island structure. The typical particle size was about 50 nm, much smaller than that observed in the film with Structure I. The deposition of Ag should have impeded formation of the interconnection FePt network. The existence of Ag particles between the FePt particles may relax the strain growth in the film and result in small particle size.[132] Impressively, the MFM image also showed a particle structure similar to the island structure observed in the AFM image; however, the particle structure was not a simple following image when the probe lifting height was set as 80 nm. As illustrated in the areas of the white squares in the AFM and MFM images, some of the bright particles in the AFM image became dark color in the MFM image due to oppositely oriented domains as contrast to the bright domains. Meanwhile, most of the boundary between the particles in AFM could still be clearly observed in the MFM image. This suggests that most of the particles in the film with Structure III were non-interaction

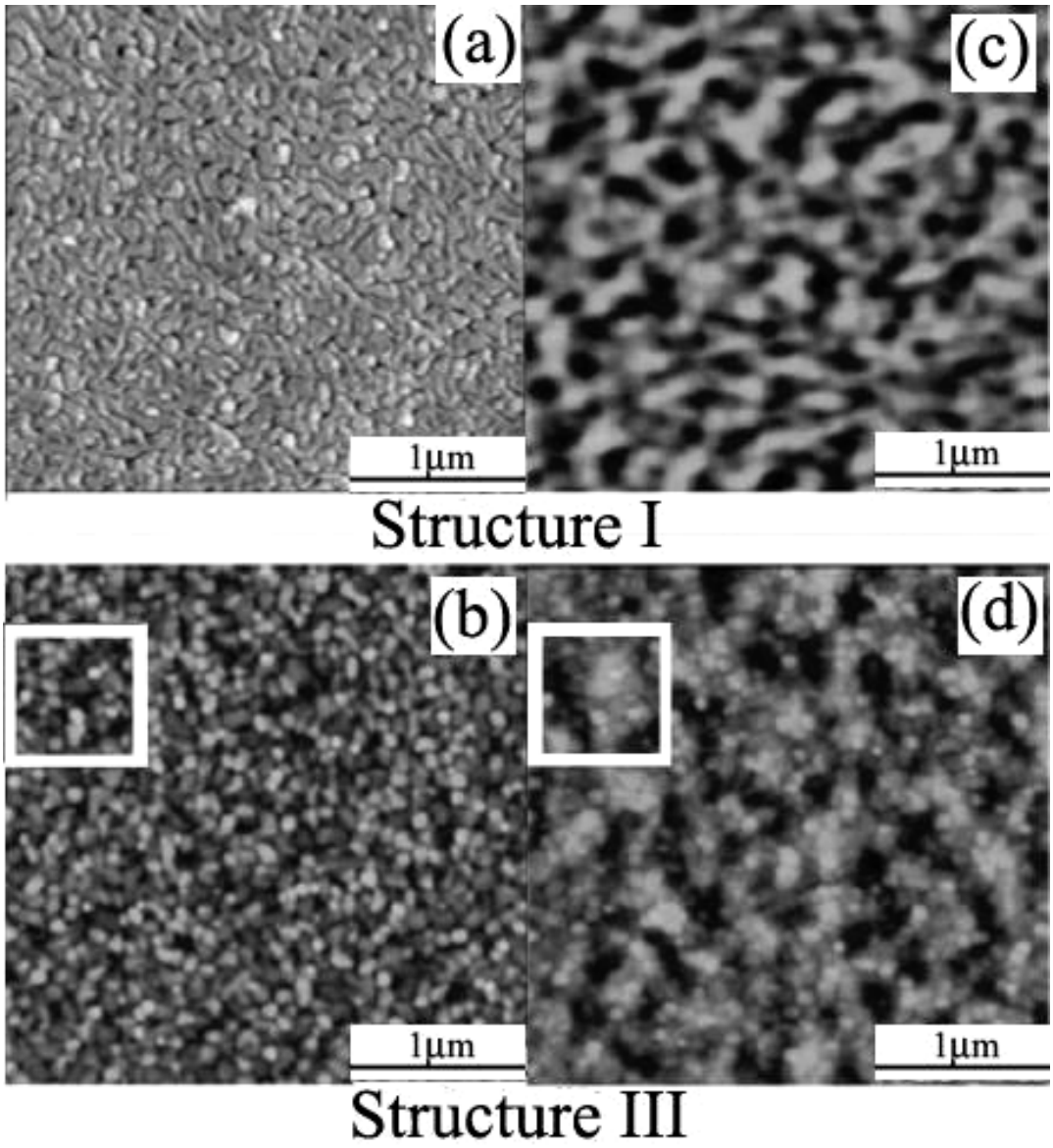

Figure 8-10. AFM and MFM images of FePt thin films; (a) AFM image of FePt film of Structure I without Ag intermediate layers; (b) AFM image of FePt film of Structure III with Ag intermediate layers; (c) MFM image of FePt film of Structure I without Ag intermediate layers; (d) MFM image of FePt film of Structure III with Ag intermediate layers; the data bar for all the images are 1 μm; the identically regions in the white boxes of (b) and (d) illustrate that MFM image is not simply following the structure if AFM.

single domains. The magnetization reversal mechanism should have changed from the domain wall pinning in the film with Structure I to a non-interaction single domain rotation mechanism. The large coercivity of the film with Structure III could have been

caused by the non-interaction mechanism of the single domains, although the coercivity value was still smaller than the theoretical calculation from the Stoner-Wohlfarth model. The non-interaction between particles also explains the small coercivity squareness S* of the hysteresis curve in the film with Structure III (Fig 8-7b).

The difference between the magnetization processes in single-domain particles and multi-domain particles is demonstrated clearly by the initial magnetization curves shown in Fig. 8-11. The magnetization curves were measured in the perpendicular direction to the film plane. The vertical axis indicates the magnetization normalized by the magnetization value at the magnetic field of 50 kOe. For the film without intermediate layers (Structure I), a steep increase of the magnetization at low magnetic field is observed. The fractional magnetization at low magnetic field corresponds to the

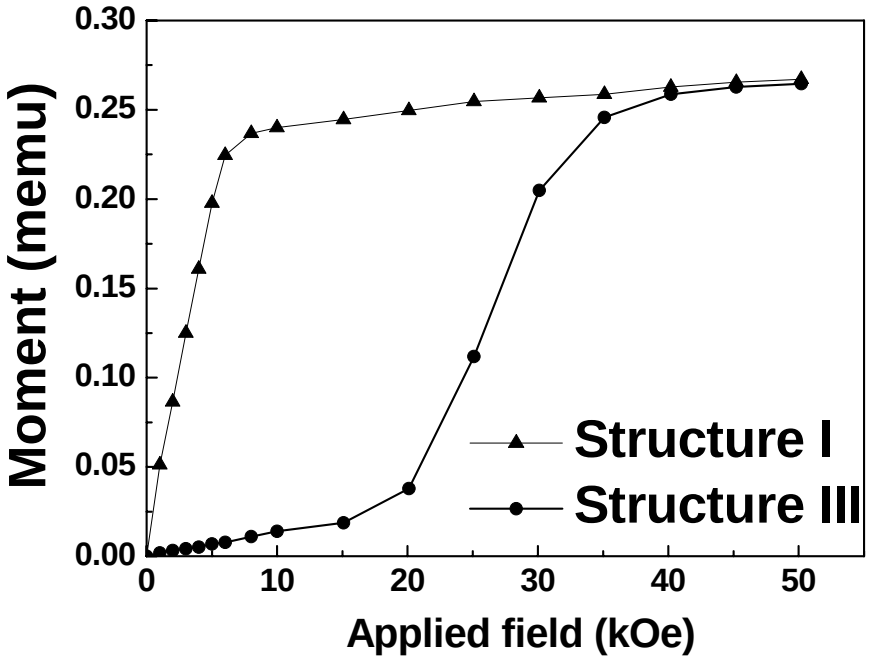

Figure 8-11 Initial magnetization curves for the FePt films with and without Ag intermediate layers; solide triangle – FePt film of Structure I without Ag intermediate layer; solide circle – FePt film of Structure III with Ag intermediate layer.

magnetic domain wall pinning. In this case, the magnetization can be easily saturated at about several kOe with the displacement of domain walls. These initial magnetization curves are usually classified as a nucleation-type. On the other hand, the film with structure III is very difficult to be magnetized. With applied magnetic field lower than 20 kOe the magnetization progress is controlled by the rotation of small domains with dimension of several tens of nanometers while domain wall propagation dominates at magnetic field larger than 20 kOe. That is, the observation of the initial magnetization process gives significant information about the co-existence of both single-domain and multi-domain structures, which explains the current coercivity for the FePt film is still much lower than that predicted by the theory.

8.5 Summary

The magnetic and microstructure properties of FePt thin films prepared by magnetron sputtering were studied. MgO single crystal substrate promoted the crystallization of FePt and introduced the (001) easy axis orientation.

The deposition of Ag intermediate layers between FePt magnetic layers results in surface morphology of film with structure III changing from a continuous 2D layer by layer growth mode to an 3D island growth mode at a relatively low temperature of 400 ^{o}C. With the island structure, the magnetization reversal mechanism was changed from domain wall pinning to a non-interaction single domain rotation mechanism. As a result, the perpendicular coercivity of the FePt film increased to over 30 kOe.

Conclusions

The crystallographic ordering and magnetic properties of FePt thin films with different thicknesses and deposition temperature are discussed in the thesis. For films deposited at the same temperature, the coercivity of FePt films increased with increase of the film thickness. For films of the same thickness, the coercivity increased with increase of deposition temperature.

With deposition of an Ag top layer on FePt films, the phase transformation of the $L1_0$ ordered FePt was promoted and the coercivity of FePt films both in the in-plane and out-of-plane directions were enhanced. Ag is immiscible with FePt and the diffused Ag may stay in the grain boundaries to reduce the exchange coupling between FePt grains. The volume expansion caused by the diffused Ag could supply large elastic energy to the FePt grains, resulting in the promotion of the phase ordering in the FePt film. Correlating with the promotion of ordering transformation of FePt by Ag diffusion, the reduction of the exchange coupling further enhances the coercivity of the FePt films.

Ag, Ru and Pt were deposited as the intermediate layer between FePt magnetic layers to enhance the coercivity in FePt perpendicular media. Comparing with Ru and Pt layers, Ag is the best candidate as the intermediate layer possibly because Ag has a similar structure of FePt and Ag can not form alloy with FePt. With the diffusion of the atoms from the intermediate layers into the magnetic layers, the intergranular exchange coupling in the FePt film reduced. Additionally, the smaller defects introduced by the thin intermediate layer with a nominal thickness of 0.25 nm may

form pinning sites to enhance the coercivity of the FePt film. On the other hand, larger defects introduced by a thicker intermediate may serve as nucleation sites to decrease the coercivity of the films.

MgO single crystal substrate promoted the crystallization of FePt and introduced the (001) easy axis orientation. The deposition of Ag intermediate layers between FePt magnetic layers results in surface morphology changing from a continuous 2D layer by layer growth mode to an 3D island growth mode at a relatively low temperature of 400 ^{o}C. With the island structure, the magnetization reversal mechanism was changed from domain wall motion to a non-interaction single domain rotation mechanism. As a result, the perpendicular coercivity of the FePt film increased to over 30 kOe.

Future work

1. Problem statements and objectives

To realize FePt thin films as commercial recording media, some technical problems need to be solved. Due to surface energy minimization, FePt tends to have a (111) texture when it is directly deposited on a substrate. To realize a perpendicular recording, it is necessary to make the easy axis perpendicular to the film plane. By *in situ* heating the substrate and utilizing CrRu underlayer, perpendicular orientated FePt film at relatively low temperature (<400 ^{o}C) was successfully achieved. However, the coercivity of the FePt media obtained from the relative low deposition temperature is not as large as desired for high-density magnetic recording.

$L1_0$ FePt also can epitaxially grow on MgO single crystal substrates with the easy axis perpendicular to film plane. But expensive MgO single crystal is required as the substrate. On the other hand, the practical implementation of perpendicular recording is using a single pole head flying on a double-layered medium composed of a data storage layer and a soft magnetic underlayer (SUL). It is believed that the addition of a SUL generates the largest benefits for perpendicular recording. The SUL is used to enhance the writing field and increases the readback signal amplitude. However, the noise due to the current SUL driven by stray magnetic fields is a serious problem that would harm the signal quality. Therefore, the objective of this proposal is to achieve suitable underlayers that have the combined function of soft underlayer and orientation layer (to induce the perpendicular orientation).

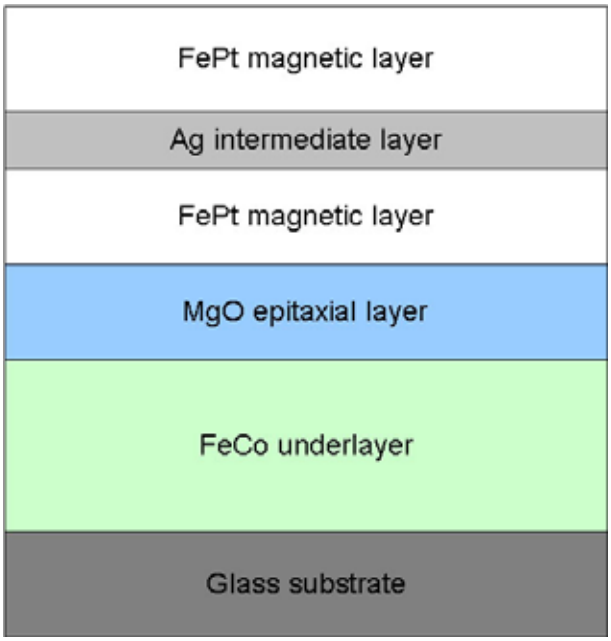

Figure A. Representive schematic of of the layer structure of FePt PMR media. FeCo is the soft underlayer; MgO is the orientation layer to introduce the perpendicular easy axis.

2. Proposed experiments and anticipated results

Figure A shows the representive schematic of the layer structure of PMR media. To develop the FePt film with a soft underlayer (SUL) keeping the magnetic easy axis (*c* axis) of FePt orientated normal to the film plane places a significant challenge in the film fabrication. A full-epitaxial-growth method to get (001) texture of FePt is of difficulty to control, because crystallographic textures of the different layers have to be matched to each other. That may limit the choices of SUL materials and yielding much less tolerance in tailoring properties of the SUL and recording layer separately.

Based on our preliminary results, FeCo layer with different doping elements and high saturation magnetization is proposed as a low noise SUL for perpendicular

recording. In order to develop the FePt (001) texture on SUL, in this proposal, one underlayer deposited on substrate to introduce the perpendicular orientation of SUL and an intermediate layer between the SUL and recording layer are proposed to magnetically decouple these two layers and to control the crystallographic texture in the recording layer as well. There are two major reasons that the commonly used underlayers such as Cr, CrRu as the intermediate layer. One is the thickness of the intermediate layer should be thin enough to keep high writing field. The other is that the intermediate layer should not be miscible with two layers. With a lattice mismatch of about 6%, MgO is proposed both as the orientation layer and intermediate layer to make FePt perpendicular recording medium, where epitaxial growth starting from the MgO underlayer through FeCo soft underlayer and MgO intermediate layer to FePt recording layer will be employed.

Different deposition methods, such as magnetron sputtering, pulsed laser deposition (PLD) and nanocluster fabrication system will be used to deposit the nanostructured FePt films. Different elements, such as Ag and Au, different thicknesses of the intermediate layers, and different deposition (or annealing) temperature will be investigated. Different SUL layers will also be investigated. To eliminate the FePt (001) texture degradation with the FePt film thickness, FePt/MgO laminated layer structure will also be investigated in the proposal.

References

1. B. Hayes, Am. Sci. 90, 212 (2002).

2. R. Wood, IEEE Trans. Magn. 36, 36 (2000).

3. S. Mao, E. Linville, J. Nowak, Z. Zhang, S. Chen. IEEE Trans. Magn. 40, 307 (2004).

4. G. Choe, J. N. Zhou, B. Demczyk, M. Yu, M. Zheng, R. Weng. IEEE Trans. Magn. 39, 633 (2003).

5. Z. Zhang, Y. C. Feng, T. Clinton, G. Badran, N. H. Yeh. IEEE Trans. Magn. 38, 1861 (2003).

6. D. Weller and A. Moser, IEEE Trans. Magn. 35, 4423 (2000).

7. J. Eisenmenger and I. K. Schuller, Nat. Mater. 2, 437 (2004).

8. W. Grogger, K. M. Krishnan, R. A. Ristau, T. Thomson, S. D. Harkness, and R. Ranjan, Appl. Phys. Lett. 80, 1165 (2002).

9. J. G. Zhu, PhD thesis. University of California San Diego, p. 172 (1989).

10. E. E. Fullerton, D. T. Margulies, M. E. Schabes, M. Carey, B. Gurney, A. Moser, M. Best, G. Zeltzer, K. Rubin, H. Rosen, and M. Doerner, Appl. Phys. Lett. 77, 3806 (2000).

11. S. X. Wang and A. M. Taratorin, Magnetic information storage technology, Cambridge University Press, p. 44 (1998).

12. K. E. Johnson, J. Appl. Phys. 87, 5365 (2000).

13. S. H. Charap, P. L. Lu, and Y. He, IEEE Trans. Magn. 33, 978 (1997).

14. A. Moser, K. Takano, D. T. Margulies, M. Albrecht, Y. Sonobe, Y. Ikeda, S. H. Sun, and E. E. Fullerton, J. Phys. D: Appl. Phys. 35, R157 (2002).

15. R. Street and J. C. Woolley, Proc. Phys. Soc. A 62, 562 (1949).

16. D. Weller, A. Moser, L. Folks, M. E. Best, W. Lee, M. F. Toney, M. Schwickert, J. U. Thiele, and M. F. Doerner, IEEE Trans. Magn. 36, 10 (2000).

17. S. Iwasaki, IEEE Trans. Magn. 235, 227 (2001).

18. S. Iwasaki, K. Takemura, IEEE Trans. Magn. 11 1173 (1975).

19. R. Wood, Y. Sonobe, Z. Jin, and B. Wilson, J. Magn. Magn. Mater. 235, 1 (2001).

20. T. Shimatsu, H. Uwazumi, H. Muraoka, and Y. Nakamura, J. Magn. Magn. Mater. 235, 273 (2001).

21. S. N. Piramanayagam, J. Appl. Phys. 102, 011301 (2007).

22. T. Shimatsu, T. Oikawa, Y. Inaba, H. Sato, I. Watanabe, H. Aoi, H. Muraoka, and Y. Nakamura, IEEE Trans. Magn. 40, 2461 (2004).

23. Y. Inaba, T. Shimatsu, H. Muraoka, J. D. Dutson, and K. O'Grady, IEEE Trans. Magn. 41, 3130 (2005).

24. B. R. Acharya, M. Zheng, G. Choe, M. Yu, P. Gill, and E. N. Abarra, IEEE Trans. Magn. 41, 3145 (2005).

25. S. N. Piramanayagam, J. Z. Shi, H. B. Zhao, C. S. Mah, and J. Zhang, IEEE Trans. Magn. 41, 3190 (2005).

26. Z. Wu, S. D. Harkness, US Patent 7,192,664, (2007)

27. E. Isaac and G. Tammann, Z. Anorg. Chem. 55, 63 (1907).

28. A. Kussman and G. V. Rittberg, Z. Metallkunde. **42**, 470 (1950).

29. L. Graf and A. Kussman, Physik. Z. **36**, 544 (1935).

30. H. Lipson, D. Schoenburg, and G. V. Stupart, J. Inst. Met. **67**, 333 (1941).

31. A. Kussman, M. Auwarter, and G. V. Rittberg, Ann. Physik. **4**, 147 (1948).

32. V. A. Nemilov, Z. Anorg. Chem. **204**, 49 (1932).

33. K. Watanabe and H. Masumoto, Trans. Jap. Inst. Met **24**, 627 (1983).

34. D. E. Laughlin, Encyclopedia of materials science and engineering. Vol. **1**, p. 263 (1988).

35. M. Fallot, Ann. phys. **10**, 291 (1938).

36. O. A. Ivanov, L. V. Solina, V. A. Demshina, and L. M. Magat, Fiz. Met. Metal. **35**, 92 (1973).

37. V. G. Pynko, A. S. Komalov, and L. V. Ivaeva, Phys. Stat. Sol. A. **63**, 127 (1981).

38. M. Sakurai, Phys. Rev. B. **50**, 3761 (1994).

39. A. Skuma, J. Phys. Soc. Jpn. **63**, 3053 (1994).

40. E. Devlin, A. Kostikas, A. Simopolous, A. Jankowski, M. Croft, and T. Tsakalakos, Nano. Mater. **6**, 699 (1995).

41. M. Podgorny, Phys. Rev. B. **43**, 11300 (1991).

42. S. Stavroyiannis, I. Panagiotopoulos, D. Niarchos, J. A. Christodoulides, Y. Zhang, and G. C. Hadjipanayis, J. Appl. Phys. **85**, 4304 (1999).

43. S. Shimizu and K. Watai, J. Jap. Inst. Met. **29**, 822 (1965).

44. M. H. Hong, K. Hono, and M. Watanabe, J. Appl. Phys. **84**, 4403 (1998).

45. S. H. Sun, C. B. Murray, D. Weller, L. Folks, A. Moser, Science. **287**, 1989 (2000).

46. S. H. Sun, Adv. Mater. **18**, 393 (2006).

47. Y. K. Takahashi, M. Ohnuma, and K. Hono, J. Magn. Magn. Mater. **246**, 259 (2002).

48. X. C. Sun, S. S. Kang, J. W. Harrell, D. E. Nikles, J. Appl. Phys. **93**, 7337 (2003).

49. F. Iskandar, H. M. Lee, T. Toda, T. Iwaki, and K. Okuyama. J. Magn. Magn. Mater. **305**, 514 (2006).

50. I. C. Chiang, and D. H. Chen. Adv. Funct. Mater. **17**, 1311 (2007)

51. Q. Yan, T. Kim, A. Purkayastha, P. G. Ganesan, M. Shima, G. Ramanath, Adv. Mater. **17**, 2233 (2005).

52. S. W. Yung, Y. H. Chang, T. J. Lin, and M. P. Hung, J. Magn. Magn. Mater. **116**, 411 (1992).

53. J. A. Aboaf, T. R. McGuire, S. R. Herd, and E. Klokholm, IEEE Trans. Mag. **20**, 1642 (1984).

54. M. Watanabe, M. Homma, and T. Masumoto, J. Magn. Magn. Mater. **177**, 1231 (1998).

55. C. P. Luo, S. H. Liou, L. Gao, Y. Liu, and D. J. Sellmyer, Appl. Phys. Lett. **77**, 2225 (2000).

56. T. Suzuki, N. Honda, and K. Ouchi, J. Appl. Phys. **85**, 4301 (1999).

57. T. Maeda, T. Kai, A. Kikitsu, T. Nagase, and J. Akiyama, Appl. Phys. Lett. **80**, 2147 (2002).

58. B. H. Li, C. Feng, T. Yang, J. Feng, and Z. H. Zhai, J. Phys. D: Appl. Phys. **39** 1018 (2006).

59. S. R. Lee, S. Yang, Y. K. Kim, and J. G. Na, Appl. Phys. Lett. **78,** 4001 (2001).

60. C. L. Platt, K. W. Wierman, E. B. Svedberg, R. V. D. Veerdonk, J. K. Howard, A. G. Roy, and D. E. Laughlin, J. Appl. Phys. **92**, 6104 (2002).

61. D. H. Ping, M. Ohnuma, K. Hono, M. Watanabe, T. Iwasa, and T. Masumoto, J. Appl. Phys. **90**, 4708 (2001).

62. S. C. Chen, P. C. Kuo, A. C. Sun, C. T. Lie, and W. C. Hsu, Mater. Sci. Eng. B. **88**, 91 (2002).

63. S. S. Kang, D. E. Nikles, and J. W. Harrell, J. Appl. Phys. **93**, 7178 (2003).

64. Y. Z. Zhou, J. S. Chen, G. M. Chow, and J. P. Wang, J. Appl. Phys. **93**, 7577 (2003).

65. C. Y. You, Y. K. Takahashi, K. Hono, J. Appl. Phys. **100**, 056105 (2006).

66. K. Sato, M. Fujiyoshi, M. Ishimaru, and Y. Hirotsu, Scripta Mater. **48**, 921 (2003).

67. S. K. Chen, C. W. Hsu, F. T. Yuan, and S. H. Hsiao **43**, 3001 (2007).

68. K. H. Kang, Z. G. Zhang, and T. Suzuki, IEEE Trans. Magn. **39**, 2317 (2003).

69. C. M. Kuo, P. C. Kuo, W. C. Hsu, C. T. Li, and A. C. Sun, J. Magn. Magn. Mater. **209**, 100 (2000).

70. K. Inomata, T. Sawa, and S. Hashimoto, J. Appl. Phys. **64**, 2537 (1988).

71. H. Y. Sun, J. L. Xu, S. Z. Feng, J. F. Su, J. Hu, and Y. P. Sun, Appl. Phys. Lett. **88**, 192501 (2006).

72. H. W. Yang, C. M. Chung, J.Y. Ding, J. Magn. Magn. Mater. **312**, 239 (2007).

73. P. C. Kuo, Y. D. Yao, C. M. Kuo, and H. C. Wu, J. Appl. Phys. **87**, 6146 (2000).

74. S. C. Chen, P. C. Kuo, C. T. Lie, and J. T. Hua, J. Magn. Magn. Mater. **236**, 151 (2001).

75. C. M. Kuo, P. C. Kuo, J. Appl. Phys. **87**, 419 (2000).

76. M. Watanabe, T. Masumoto, D. H. Ping, and K. Hono, Appl. Phys. Lett. **76**, 3971 (2000).

77. T. Suzuki and K. Ouchi, IEEE Trans. Magn. **37**, 1283 (2001).

78. Z. G. Zhang, K. Kang, and T. Suzuki, IEEE Trans. Magn. **40**, 2455 (2004).

79. T. Saito, O. Kitakami, and Y. Shimada, J. Magn. Magn. Mater. **239**, 310 (2002).

80. C. Y. Tan, Y. Z. Zhou, J. S. Chen, S. Y. Chow, and G. M. Chow, Thin Solid films. **510**, 286 (2006).

81. G. Safran, T. Suzuki, K. Ouchi, P.B. Barna, G. Radnoczi, Thin Solid films. **496**, 580 (2006).

82. B. M. Lairson, M. R. Visokay, R. Sinclair, and B. M. Clemens, Appl. Phys. Lett. **62**, 639 (1993).

83. T. Shima, T. Moriguchi, S. Mitani, and K. Takanashi, Appl. Phys. Lett. **80**, 288 (2002).

84. Y. K. Takahashi, K. Hono, T. Shima, and K. Takanashi, J. Magn. Magn. Mater. **267**, 248 (2003).

85. J. P. Wang, R. C. Chong and Z. S. Shan, Rec. Res. Devel. Magn. **1**, 139 (2000).

86. Y. F. Xu, J. S. Chen, and J. P. Wang, Appl. Phys. Lett. **80**, 3325 (2002).

87. J. S. Chen, B. C. Lim, and J. P. Wang, Appl. Phys. Lett. **81**, 1848 (2002).

88. E. F. Kneller and R. Hawig, IEEE Trans. Magn. **27**, 3588 (1991).

89. H. Zeng, J. Li, J. P. Liu, Z. L. Wang, and S. H. Sun, Nature **420**, 395 (2002).

90. J. Li, Z. L. Wang, H. Zeng, S. H. Sun, and J. P. Liu, Appl. Phys. Lett. **82**, 3743 (2003).

91. Y. K. Takahashi, T. O. Seki, K. Hono, T. Shima, and K. Takanashi, J. Appl. Phys. **96**, 475 (2004).

92. D. Ravelosona, C. Chappert, V. Mathet, and H. Bernas, Appl. Phys. Lett. **76**, 236 (2000).

93. H. Bernas, J. P. Attan, K. H. Heinig, Halley, Ravelosona, A. Marty, P. Auric, C. Chappert, and Y. Samson, Phys. Rev. Lett. **91**, 077203 (2003).

94. C. H. Lai, C. H. Yang, and C. C. Chiang, Appl. Phys. Lett. **83**, 4550 (2003).

95. K. Seshan, Handbook of Thin film deposition processes and techniques principles, methods, equipment and applications (2nd Edition). William Andrew Publishing/Noyes. p. 265 (2001).

96. B. D. Cullity, Elements of X-ray diffraction, (International Edition) Addison-Wesley. p. 143 (1978).

97. S. A. Guinier, X-ray diffraction, Freeman, San Francisco. p. 87 (1963).

98. D. Briggs, Practical surface analysis: by Auger and X-ray photoelectron Spectroscopy. John Wiley & Sons. p. 127 (1983).

99. D. B. Williams, C. B. Carter, Transmission electron microscopy: A textbook for materials science. Plenum US. p. 69 (2004).

100. S. Foner, Rev. Sci. Instr. **30**, 548 (1959).

101. P. J. Flanders, J. Appl. Phys. **63**, 3940 (1988).

102. E. C. Stoner and E. P. Wohlfarth, Philos. Trans. London Ser. A. **240**, 599, (1948). IEEE Trans. Magn. **27**, 3475 (1991).

103. M. S. Cohen, Thin film phenomena, McGraw-Hill, New York, p. 608 (1969).

104. E. P. Wohlfarth, J. Appl. Phys. **29**, 595 (1958).

105. R. A. McCurrie and P. Gaunt, Philos. Mag. **13**, 567 (1966).

106. P. E. Kelly, K. O'Grady, P. I. Mayo, and R. W. Chantrell, IEEE Trans. Magn. **25**, 3881 (1989).

107. G. B. Ferguson, K. O'Grady, J. Popplewell, and R. W. Chantrell, IEEE Trans. Magn. **25**, 3449 (1989).

108. M. Fearon and R. W. Chantrell, J. Magn. Magn. Mater. **86**, 197 (1990).

109. K. O'Grady, M. E. Hilo, and R. W. Chantrell, IEEE Trans. Magn. **29**, 2608 (1993).

110. J. D. Livingston, J. Appl. Phys. **52**, 2544 (1981).

111. T. Thomson and K. O'Grady, J. Phys. D: Appl. Phys. **30**, 1566 (1997).

112. M. G. Kim and S. C. Shin, J. Appl. Phys., **90**, 2211 (2001).

113. M. F. Toney, W. Y. Lee, J. A. Hedstrom, and A. Kellock, J. Appl. Phys. **93**, 9902 (2003).

114. K.Omote and J. Harada. Adv. X-ray Analy. **43**, 192 (2000).

115. C. H. Park, J. G. Na, P. W. Jang, S. R. Lee, IEEE Magn. **38,** 1961 (2002).

116. J. A. Christodoulides, P. Farber, M. Daniil, H. Okumura, G. C. Hadjipanayis, V. Skumryev, A. Simopoulos, and D. Weller, IEEE Trans. Magn. **37**, 1292 (2001).

117. J. P. Attané, Y. Samson, A. Marty, D. Halley, and C. Beigné, Appl. Phys. Lett. **79**, 794 (2001).

118. W. F. Brown, Phys. Rev. **60**, 139 (1941).

119. J. P. Wang, L. P. Tan, and Y. F. Liew, United States Patent, **US6,201,309B1**, (2001).

120. J. Eisenmenger and I. K. Schuller, Nat. Mater. **2**, 437 (2004).

121. C. D. Mee and E. D. Daniel (eds.), Magnetic recording technology. New York, McGraw-Hill (2nd edition). p. 155 (1996).

122. D. A. Thompson and J. S. Best, IBM J. Res. Dev. **44**, 311 (2000).

123. J. J. M. Ruigrok, R. Coehoorn, S. R. Cumpson, and H. W. Kesteren, J. Appl. Phys. **87**, 5398 (2000).

124. M. Alex, A. Tselikov, T. McDaniel, N. Deeman, T. Valet, and D. Chen, IEEE Trans. Magn. **37**, 1244 (2001).

125. H. Katayama, M. Hamamoto, J. Sato, Y. Murakami, and K. Kojima, IEEE Trans. Magn. **36**, 195 (2000).

126. T. Shima, K. Takanashi, Y. K. Takahashi, and K. Hono, Appl. Phys. Lett. **81**, 1050 (2002).

127. T. Shima, K. Takanashi, Y. K. Takahashi, K. Hono, Appl. Phys. Lett. **85**, 2571 (2004).

128. T. Shima, K. Takanashi, Y. K. Takahashi, K. Hono, G. Q. Li, and S. Ishio, J. Magn. Magn. Mater. **266**, 171 (2003).

129. C. A. Ross, Annu. Rev. Mater. Res. **31**, 203 (2001).

130. V. E. Henrich and P. A. Cox. The surface science of metal oxides. Cambridge University Press. p. 247 (1994)

131. A. Bourret, C. Adelmann, B. Daudin, J. L. Rouvière, G. Feuillet, and G. Mula, Phys. Rev. B. **63**, 245307 (2001).

132. C. M. Boubeta, J. L. C. Kramer, and A. Cebollada, J. Phys.: Condens. Matter. **15**, R1123 (2003).